NTNU
Norwegian University of
Science and Technology

Low-Cost Observer and Path-Following Adaptive Autopilot for Ships

Alexander Mykland

Marine Technology	
Submission date:	July 2017
Supervisor:	Roger Skjetne, IMT
Co-supervisor:	Dong Trong Nguyen, IMT Hans-Martin Heyn, IMT Jon Bjørnø, IMT

Norwegian University of Science and Technology
Department of Marine Technology

NTNU Trondheim
Norwegian University of Science and Technology
Department of Marine Technology

MSC THESIS DESCRIPTION SHEET

Name of the candidate: Mykland, Alexander

Field of study: Marine control engineering

Thesis title (Norwegian): Lavkost observer og bane-følgende adaptiv autopilot for skip

Thesis title (English): Low-cost observer and path-following adaptive autopilot for ships

Background

An autopilot is an important automatic control function of all commercial ships, from shipping to offshore vessels. In this project the focus is the maritime segment of shipping, where the tradeoff between price and quality is extremely important. The autopilot is here part of the navigation equipment sold and installed without access to any costly sea trial for tuning purpose. In the offshore segment, on the contrary, the autopilot is typically a function of the dynamic positioning (DP) system for which several weeks of sea trials are performed to tune the different control functions. Since the challenge with a low-cost autopilot is that no costly sea trials can be made to identify model parameters and tune the feedback gains, an adaptive autopilot design is addressed based on model-reference adaptive control (MRAC). Scaling of the model based on an appropriate method should also be performed so that a normalized vessel can be made as reference for a nominal tuning. Additionally, since also an observer is necessary to reconstruct states and filter wave-frequency motions, this will require that the separation principle holds so that the adaptive autopilot can be designed separately from the observer. The observer should also not require any complex tuning or model parameter identification. Hence, a signal-based (or kinematic) observer is focused on instead of a model-based observer.

In this project the target vessel is R/V Gunnerus, for which a maneuvering simulation model and autopilot control design will be developed. The objective is the (output feedback) adaptive autopilot design with path-following, by adding path generation and a LOS-based guidance loop to the system.

Work description

1. Perform a background and literature review to provide information and relevant references on:
    - The R/V Gunnerus and the ADPRC'16 cruise.
    - Appropriate maneuvering models, such as the Nomoto model(s) and 2DOF state-space model. This includes assessment of directional stability of ships and selection of appropriate control design models capturing such behavior.
    - Scaling methods appropriate for scaling the control design models. A normalized design model should be basis for the control design.
    - Path generation and LOS-guidance.
    - MRAC design method, incl. necessary robustification techniques.
    - Relevant signal-based observer designs. Discuss achieved stability properties and necessary parameterization and tuning w.r.t the low-cost perspective.

    Write a list with abbreviations and definitions of terms, explaining relevant concepts related to the literature study and project assignment.

2. Present the control design model for an adaptive autopilot control design, and discuss available control inputs and measured outputs. Perform normalization of the design model and discuss the motivation for this. Design an adaptive autopilot based on MRAC for your chosen normalized maneuvering model, to track a desired heading input signal from a guidance system. Implement the autpilot for the R/V Gunnerus simulation model and the HIL model and physical model of C/S Enterprise in MC-Lab.

3. Present and discuss relevant practical issues with implementation of the MRAC controller in light of experiences from the ADPRC'16 cruise. Discuss, design, and implement necessary robustification

techniques to the MRAC autopilot, and perform tests to check how well the autopilot controller works for different ship lengths based on the normalization rules. Discuss your experiences in terms of simplified tuning and performance.

4. Implement and test a signal-based observer for the autopilot, and discuss its stability properties, parametrization and tuning, and performance.

5. Present and implement a path-generation method for both straight-line and curved paths, and a Line-of-Sight (LOS) guidance algorithm with current compensation, to enable path-following for the adaptive autopilot.

6. Define test scenarios for testing the autopilot. The autopilot and LOS path following algorithm should be tested in simulation with the maneuvering model for R/V Gunnerus and at least by HIL for C/S Enterprise. Discuss the results and conclude your results.

Specifications

The scope of work may prove to be larger than initially anticipated. By the approval from the supervisor, described topics may be deleted or reduced in extent without consequences with regard to grading.

The candidate shall present personal contribution to the resolution of problems within the scope of work. Theories and conclusions should be based on mathematical derivations and logic reasoning identifying the various steps in the deduction.

The report shall be organized in a logical structure to give a clear exposition of background, results, assessments, and conclusions. The text should be brief and to the point, with a clear language. Rigorous mathematical deductions and illustrating figures are preferred over lengthy textual descriptions. The report shall have font size 11 pts. It shall be written in English (preferably US) and contain the following elements: Title page, abstract, acknowledgements, thesis specification, list of symbols and acronyms, table of contents, introduction with objective, background, and scope and delimitations, main body with problem formulations, derivations/developments and results, conclusions with recommendations for further work, references, and optional appendices. All figures, tables, and equations shall be numerated. The original contribution of the candidate and material taken from other sources shall be clearly identified. Work from other sources shall be properly acknowledged using quotations and a Harvard citation style (e.g. *natbib* Latex package). The work is expected to be conducted in an honest and ethical manner, without any sort of plagiarism and misconduct. Such practice is taken very seriously by the university and will have consequences. NTNU can use the results freely in research and teaching by proper referencing, unless otherwise agreed upon.

The thesis shall be submitted with a printed and electronic copy to the main supervisor, with the printed copy signed by the candidate. The final revised version of this thesis description must be included. The report must be submitted according to NTNU procedures. Computer code, pictures, videos, data series, and a PDF version of the report shall be included electronically with all submitted versions.

Start date: 15 January, 2017 **Due date:** As specified by the administration.

Supervisor: Roger Skjetne
Co-advisor(s): Dong Trong Nguyen, Hans-Martin Heyn, Jon Bjørnø

Trondheim

Roger Skjetne

Digitally signed by Roger Skjetne
Date: 2017.06.19 11:43:40 +02'00'

Roger Skjetne, Supervisor

Preface

This report contains the work and results from the Master's thesis in Marine Technology at NTNU. The topic of the thesis is to develop a low- cost observer and an normalized adaptive autopilot. The topic was chosen based on my interest i nonlinear control, the experience from the Amos DP Research Cruise (ADPRC'16) and from several discussions with my supervisor.

The report includes relevant work made in specialization courses and from the thesis project. In addition, experiences from ADPRC'16 will be presented and discussed throughout the thesis. The thesis was done in the spring semester of 2017, between January and July.

For understanding the report there no need of extensive knowledge of Marine Control Systems. However, basic engineering knowledge is an advantage. This is a standalone report and every subject will be properly introduced and described thoroughly throughout the text.

Trondheim, 2017-07-17

Alexander Mykland

....

Alexander Mykland

Acknowledgement

I would especially like to thank my supervisor, professor Roger Skjetne at the Department of Marine Technology, NTNU. He introduced me to nonlinear control systems and also encouraged me to choose a very interesting topic. His help, support and guidance throughout the semester made it possible to overcome several difficulties, and I am grateful.

I also would like to thank the captain Arve Knudsen and the rest of the crew on R/V Gunnerus for two pleasant cruises (sea trials). Further, I am grateful to Kongsberg Maritime with Vicenzo Calabro and Rune Skullestad, for introducing me to their work. To my co-supervisors Dong Trong Nguyen, Hans-Martin Heyn and Jon Bjørnø, I would like to say thank you for great help and discussions throughout the semester. A special thanks to Torgeir Wahl and Guttorm Udjus for providing help in the MC Lab with both HIL and with the C/S Enterprise I model vessel.

Finally, this thesis could not be done without support from my family and very good friends at VAMOS. A big thanks to Adrian, Dag, Håvard, John Elvin, Ole Johan, Martin and Sindre for a great year.

Summary

In this thesis a signal-based observer and a path-following autopilot design will be derived and implemented on the model vessel C/S Enterprise I. Using scaling methods the goal is to transfer the controllers into a full scale model of R/V Gunnerus without extensive tuning or redesign. The control system will be designed to fulfill a low-cost concept using a signal-based observer and adaptive controllers. This is done in order to avoid using model parameters, which often require lengthy and expensive sea trials. This may facilitate testing which now to a greater extend can be done using laboratories and models instead of actual full-scale vessels. Finally, a guidance loop will be integrated in the control system which will make both vessels able to follow predetermined paths using the low-cost control system.

By using maneuvering theory the 3 DOF vessel model of C/S Enterprise was reduced into uncoupled models for surge-speed, sway-yaw- and yaw-motion. Using normalization methods, these models were tested with respect to scaling, simplicity and performance. Comparison were done with the full-scale 6 DOF R/V Gunnerus model. This resulted in that the surge-speed- and the 1st order Nomoto- model for heading control were chosen as basis for the controller.

Next, a signal-based (or kinamtic) observer design was derived, implemented and tested with and without noise on the acceleration measurements. It proved that the integrator filters worked as expected and that the errors converged towards zero. For the control design, MRAC was chosen as the preferred control scheme. Two different normalized heading controllers in addition to a normalized surge-speed controller were derived and simulated based on the maneuvering models chosen earlier. Tests, were done with and without robustification for the C/S Enterprise I and with scaling on R/V Gunnerus. The simualtions produced satisfying results showing that the scaled adaptive controllers could easily be transferred to a full-scale vessel.

Finally, guidance was added to the autopilot design. Path generation for both regular- and parameterized paths were generated and path-following as well as path-tracking algortihms. Extensions were also implemented in order to cope with current effects. Simulations for both C/S Enterprise I and R/V Gunnerus proved that the vessels were able to follow these paths even when current forces acting were on the vessels. These simulations tested the whole control system developed throughout the thesis and the overall results were satisfying. As a conclusion, the scalable low-cost autopilot design and signal-based observer were succesfully implemented and simulated for both vessels, yielding good results.

Sammendrag

I denne masteroppgaven skal det utvikles en signalbasert estimator og en autopilot med integrert kursgenerering og kursfølging. Disse skal først implementeres for modellskipet C/S Enterprise I. Deretter skal kontrollerne skaleres for bruk på en fullskalamodell av R/V Gunnerus ved minimal bruk av tuning og endring av design. Kontrolldesignet følger et såkalt lavkost konsept som gjør at man vil holde kostnadene nede ved å unngå dyre og langvarige sjøprøver for å bestemme modelparameterene. Dette betyr at estimatoren som brukes har et kinamtisk design og at kontrollerene er adaptive som gjør at de kan estimere enkelte modelparametere selv. I tillegg vil normalisering bli brukt slik at man kan overføre kontrolldesignet mellom skip med forskjellig størrelse ved hjelp av skalering. Dette gjør at testing i laboratorier kan erstatte store deler av sjøprøver som bidrar til lavere kopstnader. Til slutt skal skipets integrerte kursfølger utvikles for at skipet skal kunne følge forutbestemte ruter ved hjelp av kontrollsystemet.

Først skal en modell av C/S Enterprise I med 3 frihetsgraders forenkles ved hjelp av manøvreringsteori. Disse forenklede manøvreringsmodellene skal deretter simuleres for å avgjøre hvilke som var lettest å bruke og hadde de beste egenskapene i forhold til skalering og ytelse. Disse simuleringene gav en hastighetsmodell i jag. Videre ble førsteordens Nomotomodell valgt for beskrivelse av bevegelse i giring.

Deretter ble observeren presentert, implementert og testet med og uten støy på akselerasjonsmålinger. Simuleringne viste at integrasjonsfilteret fungerte bra og at feilen i estimatene konvergerte mot null over tid. For de adaptive kontrollerne ble MRAC valgt som adaptivt design og kontrollerne bygget videre på manøvreringsmodellene som ble utviklet tidligere. To kontrollere for giring samt en for hastighetskontroll i jag ble presentert, implementert og testet for C/S Enterprise I med gode resultater både med og uten robustifisering. I tillegg ble disse skalert for bruk på fullskala modellen av R/V Gunnerus. Dette førte også til gode resultater og lite behov for tuning for å tilpasse kontrollerne.

Til slutt ble kursfølging implementert for kontrollsystemet. Generering av både vanlige og parametriserte ruter ble implementert samt kursfølging og kompensasjon av strømkrefter for autopiloten. Simuleringer ble gjort ved bruk av lavkost autopiloten og viste at hele kontrollsystemet fungerte godt sammen. De genererte kursene ble fulgt både med og uten påvirkning av havstrøm på skipene. Dette bekrefter på mange måter at den normaliserte lavkost autopiloten og den signalbaserte estimatoren ble presentert, implementert og testet med gode resultater.

Table of Contents

Preface i

Acknowledgement iii

Summary v

Sammendrag vii

Nomenclature xviii

Terms and Concepts xxvii

1 Introduction 1

- 1.1 Motivation and Background 1
  - 1.1.1 Motivation 1
  - 1.1.2 Underactuated Marine Vessels 2
  - 1.1.3 Modeling of Marine Vessels 2
  - 1.1.4 Adaptive Control 3
  - 1.1.5 Path-Following Control for Marine Surface Vessels 4
  - 1.1.6 State Estimator 4
  - 1.1.7 Target Vessels 5
  - 1.1.8 AMOS DP Research Cruise 2016 6
- 1.2 Objective and Scope 6
- 1.3 Limitations 7
- 1.4 Contributions of this Thesis 8
- 1.5 Outline of the Thesis 8

2 Mathematical Modeling 9

- 2.1 Derivation of Mathematical Vessel Models 10

2.1.1 Kinematics 10
2.1.2 Kinetics 13
2.2 Maneuvering Models 15
2.2.1 Linearized Models for Autopilot Design 16
2.2.2 Nomoto Models 17
2.2.3 Adding Nonlinear Characteristics 18
2.3 Normalization 18
2.3.1 Normalized Maneuvering Models 18
2.3.2 Open-Loop Stability 21
2.4 Numerical Values for CSEI 21
2.4.1 Mass Matrix 21
2.4.2 Damping Matrix 22
2.4.3 Coriolis Matrix 23
2.5 Simulation Study of Maneuvering Models 23
2.5.1 Simulation Results using Decoupled Maneuvering Models 23
2.5.2 Simulation Results from Scaled Maneuvering Models 26
2.5.3 Open-Loop Stability 27
2.6 Conclusions 29

3 Simulations and Experiment Setup **31**
3.1 Simulations using MATLAB/Simulink 31
3.2 Hardware-in-the-Loop Simulations 31
3.3 Physical Experiments 32
3.3.1 The MC Lab 32
3.3.2 Experiments on the CSEI Model Vessel 33
3.3.3 Notes on Physical Experiments with CSEI 34

4 Low-Cost Observer Designs **35**
4.1 Kinematic Observer 36
4.1.1 Attitude Observer 37
4.1.2 Translational Observer 37
4.2 Stability Analysis 38
4.3 Simulations of the Kinematic Observer 38
4.4 MATLAB/Simulink Simulations 39
4.4.1 Estimation using Noiseless Signals 39
4.4.2 Estimation using Noisy Signals 42
4.4.3 HIL Simulation of Observer 45
4.5 Conclusions 46

5 Model Reference Adaptive Control **49**
5.1 Heading Controllers 50
5.1.1 Direct MRAC Design with Integral Action 50
5.1.2 Direct MRAC Design by Augmenting a Baseline Control Law 55
5.2 Surge Controller 57
5.3 Robustification Methods 60
5.3.1 Dead-zone Modificator 60
5.3.2 Projection Operator 61
5.4 Simulation Study of the Controllers 61
5.4.1 MRAC for CSEI 62
5.4.2 Robustification of the Controllers 66
5.4.3 HIL Simulations of the MRAC 68
5.4.4 Simulating Scaled Controllers on the R/V Gunnerus Model 69
5.5 Implementation Issues on a Full Scale Test with R/V Gunnerus 74
5.6 Conclusions 74

6 Guidance **77**
6.1 Steering Laws for Regular Paths 78
6.1.1 Straight-lines Between Waypoints and Circular Paths 78
6.1.2 Line-of-Sight Guidance 79
6.2 Steering Laws for Parameterized Paths 81
6.2.1 Parameterization of Paths 83
6.2.2 Update Laws 84
6.3 Current Compensation 85
6.3.1 Sideslip Angle 85
6.3.2 Integral Line-of-Sight 85
6.4 Simulations of the Path-Following Algorithms 87
6.4.1 Simulations of Path-Following and Path-Tracking for CSEI 87
6.4.2 HIL Simulations for Guidance 96
6.4.3 Simulations of Path-Following and Path-Tracking for R/V Gunnerus . . 97
6.5 Conclusions 101

7 Discussion **103**
7.1 Discussing the Normalized Maneuvering Models 103
7.2 Discussion Concerning the Signal-Based Observer 104
7.3 Discussion of the Adaptive Controllers 104
7.4 Discussion Based on Guidance 104

8 Conclusions and Further Work **107**
8.1 Overall Conclusion 107
8.2 Further Work 108

Bibliography **108**

List of Tables

2.1 Normalization of parameters in surge, sway and yaw 19
2.2 General parameters for CSEI 22
2.3 Added mass parameters for CSEI 22
2.4 Drag coefficients for CSEI 22

List of Figures

1.1 The C/S Enterprise I model vessel 5
1.2 Photo of R/V Gunnerus taken from the ADPRC'16 6

2.1 Thrust input for the CSEI maneuvering models 24
2.2 Surge speed model compared to real 3 DOF model 25
2.3 Sway-yaw subsystem compared to real 3 DOF model 25
2.4 Nomoto models compared to real 3 DOF model 26
2.5 Thrust input for the scaled CSEI maneuvering models 27
2.6 Scaled surge speed model compared to real 6 DOF model of R/V Gunnerus . . 28
2.7 Scaled 1st order Nomoto model compared to real 6 DOF model of R/V Gunnerus 28

3.1 Screenshot of the workbench used for monitoring HIL simulations and lab experiments 32
3.2 The Marine Cybernetics Laboratory 33

4.1 Thrust input for the observer study 39
4.2 Position and velocity estimates without noise 40
4.3 Position and velocity errors without noise 40
4.4 Estimated angular rates without noise 41
4.5 Yaw rate error without noise 42
4.6 Attitude without noise 42
4.7 True and estimated yaw angle with the error for noiseless test 43
4.8 Estimated postion and velocity from simulations with noise 44
4.9 Error in postion and velocity estimates from simulations with noise 44
4.10 Estimated heading and yaw rate from simulations with noise 45
4.11 Errors in heading and yaw rate from simulations with noise 45
4.12 Estimated position and heading from HIL simulation 46
4.13 Errors in position and heading estimates from HIL simulation 47

5.1 Two different designs of MRAC 50
5.2 Desired surge velocity and heading for CSEI 62
5.3 Reference states together with the corresponding measured states 63
5.4 Parameter estimates for MRAC with integral action 63
5.5 Surge reference model compared to actual values 64
5.6 Estimated controller gains $\hat{\rho}$ and $\hat{\theta}_i$ 65
5.7 Reference states together with the corresponding measured states for baseline MRAC 66
5.8 Parameter estimates for the baseline MRAC 66
5.9 Control inputs for the simulation 67
5.10 Chattering on parameter estimates 67
5.11 Chattering removed by dead-zone modification 68
5.12 Desired and actual surge velocity from HIL simulation 69
5.13 Desired and actual heading from HIL simulation 69
5.14 Desired surge velocity and heading for CSEI 70
5.15 Results from scaled vectorial heading controller with integral action 71
5.16 Estimated paremeter values for integral action MRAC for R/V Gunnerus 71
5.17 Results from scaled MRAC with a baseline control law for R/V Gunnerus . . . 72
5.18 Estimated paremeter values for MRAC with a baseline control law for R/V Gunnerus 72
5.19 Results from scaled indirect MRAC for the surge-speed of R/V Gunnerus . . . 73
5.20 Estimated paremeter values for the indirect surge-speed MRAC for R/V Gunnerus 73

6.1 LOS setup. [Courtesy: Fossen (2011)]. 80
6.2 LOS setup for circular path. [Courtesy: Breivik and Fossen (2008)]. 82
6.3 LOS setup for parameterized paths. [Courtesy: Breivik and Fossen (2008)]. . . 82
6.4 Straight-line path in between waypoints 88
6.5 Cross-track error for straight-line path in between waypoints 88
6.6 Circular path generated in clockwise direction 89
6.7 Circular path generated in counter-clockwise direction 89
6.8 Cross-track error for circular path generated in clockwise direction 90
6.9 Cross-track error for circular path generated in counter-clockwise direction . . 90
6.10 Parameterized straight-line paths 91
6.11 Epsilon for parameterized straight-line paths 91
6.12 Parameterized path variable 92
6.13 Parameterized circular path 93
6.14 Epsilon for circular path 93
6.15 Straight-line path with current compensation 94

6.16 Epsilon for straight-line path with current compensation 94
6.17 Circular path with current compensation 95
6.18 Cross-track error for circular path with current compensation 95
6.19 Square path consisting of straight lines from HIL 96
6.20 Circular path generated in counter-clockwise direction for R/V Gunnerus . . . 97
6.21 Cross-track error for circular path generated in counter-clockwise direction for R/V Gunnerus 98
6.22 Parameterized circular path for R/V Gunnerus 99
6.23 Epsilon for circular path for R/V Gunnerus 99
6.24 Path variable for circular path 100
6.25 Straight-line path with current compensation 100
6.26 Epsilon for straight-line path with current compensation 101

Nomenclature

Abbreviations

ASV - Autonomous Surface Vehicle
ADPRC'16 - AMOS DP Research Cruise 2016
AMOS - Centre for Autonomous Marine Operations and Systems
AUV - Autonomous underwater Vehicle
BL - Baseline
BODY - Body Reference Frame
CG - Center of Gravity
cRIO - NI compact RIO
CSEI - CyberShip Enterprise I
DOF - Degrees of Freedom
DP - Dynamic Positioning System
ECEF - Earth- Centered Earth-Fixed
ECI - Earth-Centered Inertial
EKF - Extended Kalman Filter
GNSS - Global Navigation Satellite System
GPS - Global Positioning System
HIL - Hardware-in-the-Loop
IA - Integral action
ILOS -Integral Line-of-Sight
IMU - Inertial Measurement Unit
IND - Indirect MRAC
KM - Kongsberg Maritime
LFC - Lyapunov Function Candidate
LOS - Line-of-Sight
m - Meters (SI)
MC Lab - Marine Cybernetics Laboratory
MRAC - Model Reference Adaptive Control
NED - North-East-Down
N - Newtons (SI)
NI - National Instruments

NTNY - Norwegian University of Science and Technology
PhD - Doctor of Philosofy
PID - Proportional, Integral, Derivative
REF - Reference (signals)
RIO - Reconfigurable Input/Output modules
UGES - Uniformly Globally Stable
UGS - Uniformly Globally Stable
ULES - Uniformly Locally Stable
USGES - Uniformly Semi-Globally Exponetnially Stable
UB - Uniformly Bounded
UUB - Ultimately Uniformly Bounded
VRU - Virtual Reference Unit

Greek Letters

α - Control input for indirect MRAC
β - *Rotation
β - *Sideslip angle
Γ - Unknown gain in MRAC design
$\mathbf{\Gamma}$-Adaptation gain matrix
$\mathbf{\Gamma}_x$-Adaptation gain matrix
$\mathbf{\Gamma}_\theta$-Adaptation gain matrix
$\mathbf{\Gamma}_\Omega$-Adaptation gain matrix
γ_b - Adaptation gain
Δ - Lookahead distance
δ - Control input
δ_{bl} - Control input MRAC with baseline control law
δ_{ia} - Control input MRAC with integral action
$\boldsymbol{\epsilon}$ - *Vector of quaternion components
$\boldsymbol{\epsilon}(\cdot)$ - Vector of along-track- and cross-track- errors
$\boldsymbol{\eta}$ - Position and attitude in NED frame
$\boldsymbol{\eta}_d^s$ - Path derivatives
$\boldsymbol{\eta}_d^{s^2}$ - Path double derivatives
η - Skalar term in the quaternion vector
Θ - Vector of unknown parameters
Θ_{nb} - Attitude in Euler angle
θ - *Observer gain
θ - *Pitch angle

θ_{max} - Upper bound on estimates

λ - Unit vector

μ - Dead-zone modification term

$\dot{\boldsymbol{\nu}}$ - Linear and angular acceleration vector in BODY frame

$\boldsymbol{\nu}$ - Linear and angular velocity vector in BODY frame

$\boldsymbol{\nu}_c$ - Current velocity vector

$\boldsymbol{\nu}_r$ - Relative velocity vector

ξ - Integral state

ρ - Estimated bias for indirect MRAC

$\boldsymbol{\xi}$ - Integral state vector

$\boldsymbol{\sigma}$ - Correction vector in observer

σ - *Switching parameter for turning on/off feedback in reference filters

σ - *Gain for ILOS

$\boldsymbol{\tau}$ - Total force vector

τ_m - Moment

$\boldsymbol{\tau}_N$ - Control input moment in yaw

$\boldsymbol{\tau}_{RB}$ - Rigid-body force vector

$\boldsymbol{\tau}_{wave}$ - Wave force vector

$\boldsymbol{\tau}_{wind}$ - Wind force vector

$\boldsymbol{\tau}_X$ - Control input force in surge

$\boldsymbol{\tau}_Y$ - Control input force in sway

Υ - Vector of unknown parameters for MRAC with baseline control law

ϕ - Roll angle

$\boldsymbol{\Phi}(\cdot)$ - Known regressor vector

χ - Course angle

ψ - Yaw angle

ψ_c - Measured compass angle

ψ_d - Desired heading angle

ψ_{cmd} - Commanded heading angle

ψ_{int} - Integral of the yaw angle

ψ_p - Desired heading angle

ψ_r - Convergence term for guidance

ψ_{ref} - Heading reference angle

Ω - Controller gain vector for MRAc with baseline control law

Ω_0 - Bounded set

Ω_1 - Bounded set

$\boldsymbol{\omega}$ - Angular rate vector

$\boldsymbol{\omega}_{IMU}$ - Measured angular rate

Roman Letters

$\boldsymbol{A}$ - State matrix for baseline control law

$\boldsymbol{A}_{bl}$ - Plant system matrix, MRAC with baseline

$\boldsymbol{A}_{ia}$ - Plant system matrix, MRAC with integral action

$\boldsymbol{A}_{ref}$ - Reference plant system matrix

$\boldsymbol{A}_{v}$ - State matrix for observer like MRAC control

a_{ind} - Plant system scalar, indirect MRAC

a_i - Parameters for maneuvering characteristic estimates

a_{ref} - Reference plant scalar

$\boldsymbol{B}$ - Input matrix for baseline control law

$\boldsymbol{B}_{bl}$ - Input system matrix, MRAC with baseline

$\boldsymbol{B}_{ia}$ - Input system matrix, MRAC with integral action

^{b}, $\{b\}$ - *NED frame decomposition

B -Width

b - Bias

$\boldsymbol{b}$ - Bias vector

$\boldsymbol{b}_g$ - Bias vector

$\boldsymbol{b}_{bl}$ - Input system vector, MRAC with baseline

$\boldsymbol{b}_{ia}$ - Input system vector, MRAC with integral action

$\boldsymbol{b}_{ref}$ - Reference plant input vector

b_i - Bech's coefficients for maneuvering $i - 0, 1, 2, 3$

b_{ind} - Input system scalar, indirect MRAC

$\boldsymbol{C}$ - *Combined coriolis matrix

$\boldsymbol{C}$ - *Output matrix for baseline control law

$\boldsymbol{C}_A$ - Centripetal-coriolis matrix

$\boldsymbol{C}_{bl}$ - Output matrix, MRAC with baseline

$\boldsymbol{C}_{ia}$ - Output matrix, MRAC with integral action

$\boldsymbol{C}_{RB}$ - Rigid-body centripetal matrix

$\boldsymbol{c}^b$ - Reference vector for observer

$\boldsymbol{c}^n$ - Reference vector for observer

$\boldsymbol{c}_{bl}$ - Input system vector, MRAC with baseline

$\boldsymbol{c}_{ia}$ - Input system vector, MRAC with integral action

c_{ind} - Output system scalar, indirect MRAC

$\boldsymbol{D}$ - Combined damping matrix

$\boldsymbol{D}_{lin}$ - Linear damping matrix

$\boldsymbol{D}_{nl}$ - Nonlinear damping matrix

D - Down. Vertical position below surface in NED frame, depth

d_u- combined damping in surge

E - True East. Horizontal position component

e - Error

e_{int} - Integral cross-track error term

$e(\cdot)$ - Cross-track error

e_{ind} - Error in indirect MRAC

e_0 - Parameter for dead-zone modificator

$\boldsymbol{e}$ - Error vector

$\boldsymbol{e}_{bl}$ - Error vector MRAC with baseline

$\boldsymbol{e}_{ia}$ - Error vector MRAC integral action

$\boldsymbol{f}_{IMU}$ - Specific force, acceleration measurements

g - Gravitational constant $\boldsymbol{g}(\cdot)$ - Restoring force matrix

$\boldsymbol{g}_0$, $\boldsymbol{g}$ - Gravity vector

$\boldsymbol{H}$ - Normalization matrix

$H_B(r)$ - Bech's nonlinear extension of Nomoto

$H_N(r)$ - Norrbin's nonlinear extension of Nomoto

I - Mass moment of Inertia

$\boldsymbol{I_{3\times3}}$ - Unit matrix

$\boldsymbol{I}_b$ - Mass moment of inertia matrix

I_z - Mass moment of inertia in yaw

$\boldsymbol{J}$ - LQR cost function

$\boldsymbol{J}(\cdot)$ - 6 DOF velocity transformation matrix

$\boldsymbol{J}(\cdot)_{\boldsymbol{q}}$ - 6 DOF velocity transformation matrix for quaternions

$\boldsymbol{K}_{LQR}$-LQR gain vector

$\boldsymbol{K}_{PID}$-PID gain vector

$\boldsymbol{K}_{pp}$ - Observer gain matrix

$\boldsymbol{K}_{vp}$ - Observer gain matrix

$\boldsymbol{K}_x$ - Controller gain vector

$\boldsymbol{K}_\delta$ - Controller gain for MRAC with baseline control law

$\boldsymbol{K}_{\xi p}$ - Observer gain matrix

K - Nomoto gain

K_0-Nominal gain

k_1 - Observer gain

k_2 - Observer gain

k_i - Observer gain

k_p - *Observer gain

k_p - *Controller gain

k_{ppi} - Observer gain

k_{vpi} - Observer gain
$k_{\xi pi}$ - Observer gain
$\boldsymbol{L}_v$ - Matrix for observer like system
L - Length
L$_{pp}$-Ship length between fore- and aft- perpendiculars
$\boldsymbol{M}$ - Combined mass matrix
m - Mass
$\boldsymbol{M}_A$ - Added mass matrix
$\boldsymbol{M}_{RB}$ - Rigid-body mass matrix
N - True North. Horizontal position component
N_v - Linear damping coefficient in yaw
$N_{|v|v}$ - Nonlinear damping coefficient in yaw
$N_{|v|r}$ - Nonlinear coupled damping coefficient in yaw
$N_{\dot{r}}$ - Added mass coefficient in yaw
N_r - Linear damping coefficient in yaw
N_{rr} - Nonlinear damping coefficient in yaw
N_{rrr} - Nonlinear damping coefficient in yaw
$\boldsymbol{N}(\cdot)$ - Combined coriolis and damping matrix
$\boldsymbol{N}(u_0)$ - Linearized combined coriolis and damping matrix
^{n}, $\{n\}$ - NED frame decomposition
n_i - Norrbins coefficients for maneuvering $i - 0, 1, 2, 3$
$\boldsymbol{P}$ - Solution of the ARE for actual plant
$\boldsymbol{P}_v$ - Solution of the ARE for observer like plant
$\boldsymbol{P}$ - *Gain matrix for LQR
$\boldsymbol{P}_{ref}$ - Solution of the ARE for reference plant
p - Angular velocity in roll
$\boldsymbol{p}$ - Horizontal position vector
$\boldsymbol{p}_0$ - Initial position vector
$\boldsymbol{p}_c$ - Coordinates of origin of circle
$\boldsymbol{p}_d$ - Desired position vector
$\boldsymbol{p}_d^s$ - Derivative of the desired position vector
$\boldsymbol{p}_p$ - Path position
p_i- Integrator position
p^z- Virtual reference
$\boldsymbol{Q}$ - *Solution of the Lyapunov equation for the actual plant
$\boldsymbol{Q}$ - *Gain matrix for LQR
$\boldsymbol{Q}_{ref}$ - Solution of the Lyapunov equation for reference plant
$\boldsymbol{Q}_v$ -Solution of the Lyapunov equation for observer like plant

$\boldsymbol{q}$ - Quaternion vector

q - Angular velocity in pitch

$\boldsymbol{R}(\Theta)$ - 3 DOF Velocity transformation matrix

$\boldsymbol{R}(\psi)$ - Horizontal Velocity transformation matrix

R - Radius in LOS algorithm

r - Yaw rate

r_g^b - Distance from CG to origin of b-frame

r_c - radius of circular path

$\boldsymbol{S}(\cdot)$ - Skew-symmetric matrix

s (Laplace integration) - Mathematical operator in Laplace transform*

s - *Parameterized path variable

$s(\cdot)$ - Along-track error

$\boldsymbol{T}$-Transformation matrix

$\boldsymbol{T}_\Theta$ - Quaternion velocity transformation matrix

T-Time constant for first order Nomoto model

T_0-Nominal time constant

T_1-Time constant for second order Nomoto model

T_2-Time constant for second order Nomoto model

T_3-Time constant for second order Nomoto model

t - Time, duration

U - Vessel speed

u - Surge velocity

u_{bl} - LQR control input

u_d - Desired speed

u_{ind}- State in indirect MRAC

u_0 - Linearized surge velocity

u_c - Current velocity in surge

u_r - Relative velocity in surge

u_{ref} - Reference surge speed

$\boldsymbol{v}$ - Horizontal velocity vector

v - Sway velocity

v_c - Current velocity in sway

v_r - Relative velocity in sway

v - Parameter in observer-like matrix

w - Heave velocity

w_c - Current velocity in heave

$X_{\dot{u}}$ - Added mass coefficient in surge

X_u - Linear damping coefficient in surge

X_{uu} - Nonlinear damping coefficient in surge
$X_{|u|u}$ - Nonlinear damping coefficient in surge
X_{uuu} - Nonlinear damping coefficient in surge
$\boldsymbol{x_{bl}}$ - State vector MRAC with baseline
$\boldsymbol{x_{ia}}$ - State vector MRAC with integral action
$\boldsymbol{x_{ref}}$ - Reference state vector
x - Surge position
x_{ind} - State scalar for indirect MRAC
x$_{int}$ - Integral parameter surge
x$_{g}$ - Distance from CG
$Y_{\dot{v}}$ - Added mass coefficient in sway
Y_{v} - Linear damping coefficient in sway
Y_{vv} - Nonlinear damping coefficient in sway
$Y_{|v|v}$ - Nonlinear damping coefficient in sway
Y_{vvv} - Nonlinear damping coefficient in sway
$Y_{|v|r}$ - Nonlinear coupled damping coefficient in sway
$Y_{\dot{r}}$ - Coupled added mass coefficient in sway
$\boldsymbol{y}$ - Output vector
y - Output
$\boldsymbol{y}_{cmd}$ - Commanded output vector
y - Sway positon
y_{cmd} - Commanded output
$\boldsymbol{y}_{bl}$ - Regulated output MRAC with baseline control law
$\boldsymbol{y}_{ia}$ - Regulated output MRAC with integral action
y$_{int}$ - Integral parameter sway
z - Heave position
$\boldsymbol{z}$ - State in the baseline control law

Symbols

’ - Prime-scaled parameter, nondimensional
” - Bis-scaled parameter, nondimensional
ˆ - Estimates
˜ - Difference between true values and estimates
˙ - First derivative
¨ - Second derivative

Terms and Concepts

- **Adaptive Control** is a control design in which design parameters can be estimated online while controlling a craft or a process.
- **Autopilot** is an automatic control function for steering a moving craft.
- **Controllers** are what makes the vessel move. It relates the actual- and the commanded-states to thrust and steer the vessel towards the desired values.
- **Dynamic Positioning System** is a control system that is used for maintaining postion and heading for marine crafts. It can also be used for navigating at very slow velocities to desired setpoints. The Dynamic Positioning System is controlled by computers.
- **Equilibrium** is the point in which the observers or controllers stabilizes to with or without disturbances acting on them.
- **Heading Control** refers the controllers ability to steer the craft to the desired yaw angle.
- **Maneuvering Model** is a mathematical description for a relatively fast moving vessel (faster than for seekeeping or DP models).
- **Path-Following** for a marine vessel is the ability to follow paths without any constraints on time.
- **Path-Tracking** for a marine craft allows the vessel to track a desired path with constraints on duration.
- **Surge-speed Control** is ability to make the vessel follow a certain speed in surge using a controller.
- **Stability** in control design is that the errors converges towards zero both with and without disturbances. If the errors in the control signals fail to converge the system is said to be unstable.
- **State Estimator** or observer is a vital part of a control system which is used to reconstruct unmeasurable states and also to act as backup in case of signal failure.
- **Underactuated Vessels** have control inputs in less DOFs than its workspace. For a surface vessel moving in 3 DOF an underactuated vessel have control inputs in for instance surge and yaw while sway input is not available.

Chapter 1

Introduction

This thesis presents the analysis of non-dimensional adaptive autopilot designs, a signal-based observer and guidance for a under-actuated path following marine vessel. The first chapter is meant for introducing the topics, ongoing research, the scope of this report and contributions resulting from this study.

1.1 Motivation and Background

1.1.1 Motivation

The first control systems for marine crafts date back to the 19th century for steam powered engines, but it was not until the early nineteen-hundreds when the first gyrocompass was implemented on a US war ship that the first autopilot was designed. In 1922 the engineer Nicolas Minorsky published the first theoretical analysis for a Proportional-integral-derivative (PID) controller and implemented an automatic steering device on USS New Mexico. This paved way for modern ship autopilots and control theory. Nowadays the autopilot is widely used in a wide range of vehicles, from space crafts and planes to cars and marine vessels. It contributes to easier and safer maneuvering operations and requires less onboard crew to operate. For marine applications the dynamic positioning (DP) systems and ship autopilots are the most known applications.

Recently, as the marine control systems are becoming more accurate, reliable and safe, the idea of a completely unmanned vehicle has emerged and become a reality. Autonomous underwater vehicles (AUV) were used for mapping the seabed and for monitoring underwater structures to prevent diving accidents in offshore operations. For surface vessels the autonomy is also growing and fully autonomous surface vehicles (ASV) have been developed. This tendency for autonomy makes the development of improved controllers important leading to the introduction of automatic path generation and guidance control. Together they can make ship navigation safer, more environmentally friendly and efficient.

A new aspect of autonomous vessels is the cost versus performance since control systems have become part of most commercial ships. This has huge influence on the control designs as most of them uses physical vessel parameters and gains determined by expensive and lengthy sea trials.

In order to fulfill the constraints on the cost and performance one must find other ways to determine these parameters. This can be done using controllers that are able to estimate and adapt to the required parameters. Including a state estimator, or observer, the cost of additional sensors on board is reduced and it can provide a certain level of redundancy should any of the remaining sensors fail. Following the model-free control design a kinematic observer suits the purpose and assists the control systems in estimating unmeasurable states.

1.1.2 Underactuated Marine Vessels

Most vessels are underactuated. This is because it simplifies the control system design, reduces cost and consumes less energy. As described in Fossen (2011), underactuated control refers to when a craft is operating in more degrees of freedom (DOF) than it has control inputs.

For a conventional autopilot model for a 3 DOF surface vessel model, only one control input (in yaw) is needed to control the heading. In order to solve the path-following control objective for the same vessel model an additional control input in surge is needed. The main challenge for underactuated vessel is that the sway dynamics are not controlled and are very responsive to disturbances. The sway equation must be stabilized in order to make the whole system stable. For this thesis underactuated vessel models will be used for as a basis for developing the control system.

1.1.3 Modeling of Marine Vessels

In order to develop control systems for marine crafts mathematical models are essential. Using accurate mathematical models together with better computers and simulation tools like the hardware-in-the-loop (HIL) simulators can reduce the risk of accidents as well as time. These mathematical descriptions are often formulated in two different complexity levels (Sørensen (2013)). A process plant model (PPM) or a simulation model (Fossen, 2011) is a detailed description of the vessel. It is used to simulate real plant dynamics and requires a lot of computer power and time in order to obtain results with a certain level of accuracy. For a control system, however, it is normal to utilize a simplified model which includes only the most important physical properties of the vessel in study. This is called the control plant model. It can be applied to the controllers itself or be used in analytic stability analysis. A third model approach exists for observer design. Although similar to the simulation model its main purpose is to reconstruct unmeasured states, noise and waves in addition as being a fail-safe option in case of sensor failures.

All mathematical models for marine crafts are designed with respect to the operational conditions. Low-velocity (seekeeping) models are often used for applications of Dynamic positioning (DP) while the high-velocity maneuvering models (Fossen, 2011) are applied for operational conditions which require faster moving vessels. For an autopilot model the latter one is applied for simulations. This is because the vessel is assumed to be moving at a cruising speed far greater than the desired speed for seekeeping purposes.

A useful extension of the maneuvering models is to normalize them as described in Fossen (2011). It is a useful tool in order to simplify the transition from a small model to the full scale vessel or using the same controller on similar vessels. By normalizing the maneuvering models, the controllers can also be made non-dimensional. More time can therefore be used in laboratories with a model vessel because the maneuvering models and the controllers are scalable. This reduce the duration of implementation, cost of sea trials and tuning.

1.1.4 Adaptive Control

For the control purpose an adaptive design is chosen. According to Ioannou and Sun (2012) adaptive control is described by the controllers ability to adapt to changing conditions. While doing this the controller input is modified to change the vessel dynamics and estimates unknown disturbances in order to remove them from the true dynamics. This does not necessarily mean that the estimates represent true parameter values nor the actual disturbances. There exists two main branches in adaptive control design. The first one, called indirect adaptive control, estimates system parameters for which it calculates the controller parameters at each time step. The second method is called direct adaptive control. In contrast to the indirect method, the plant is parameterized in terms of the unknown model parameters calculating the control parameters in one step.

Adaptive control emerged with the advances in control theory in the 1950s. One of the first methods to be developed was called Model Reference Adaptive Control (MRAC). MRAC can be applied with both direct and indirect adaptation and is still one of the preferred techniques for adaptive control and will be the method of choice for this thesis. In short, this method forces the system output to track a bounded reference signal estimating model parameters giving the desired response (Lavretsky and Wise, 2012). Robust control can be achieved for MRAC similarly to other adaptive techniques. Robust control guarantee boundedness of the output signal even with plant uncertainties and bounded disturbances. Two common methods for robustification are the Dead zone modification which stops adaptation when the reference is tracked properly and the Projection operator which prevents drifting of the estimates. Both are described in Ioannou and Sun (2012) and Lavretsky and Wise (2012).

1.1.5 Path-Following Control for Marine Surface Vessels

Path-following is a widely used control function for maneuvering. The goal is to make the vessel follow predefined paths without any time constraints. For underactuated vessels this can be done by controlling the heading and adjusting it in order to minimize the cross track error. Line-of-sight guidance is the most common way to handle the path-following control problem. It uses the controlled heading to compensate for the lack of control input in sway in order to follow the desired path even with environmental disturbances such as current and wind. In (Fossen, 2011) these forces are handled by calculating the sideslip angle and making the course angle compensate in order to reduce it.

This thesis, however, focuses on the ILOS guidance presented in Børhaug (2008). Here a new approach to handle constant ocean currents without the need of the sideslip angle is discussed. In short, an integral state multiplied with a tunable gain is added into the heading equation in original line-of-sight guidance. If this integral term is used it can be tuned to compensate for constant disturbances.

1.1.6 State Estimator

Reconstructing unmeasured states is very important on board a marine vessel. As mentioned in Section 1.1.1, it can reduce costs of additional sensors and provide redundancy if any problems occur.

The chosen design is a signal-based or kinematic observer and uses gyro measurements of velocity and acceleration to estimate the velocities and attitude of the vessel (Brodtkorb et al., 2016). The attitude and translation part of the observer are separated as two fundamentally different components only connected by the estimated accelerations in North-East-Down (NED) frame and the wave frequency state.

1.1.7 Target Vessels

For this thesis the path-following autopilot and the signal-based observer will be implemented on a medium-high maneuvering model of R/V Gunnerus, NTNUs research vessel. For HIL simulations, scaling controllers and for practical experiments in the Marine Cybernetics Laboratory (MC Lab) the C/S Enterprise I (CSEI) will be used.

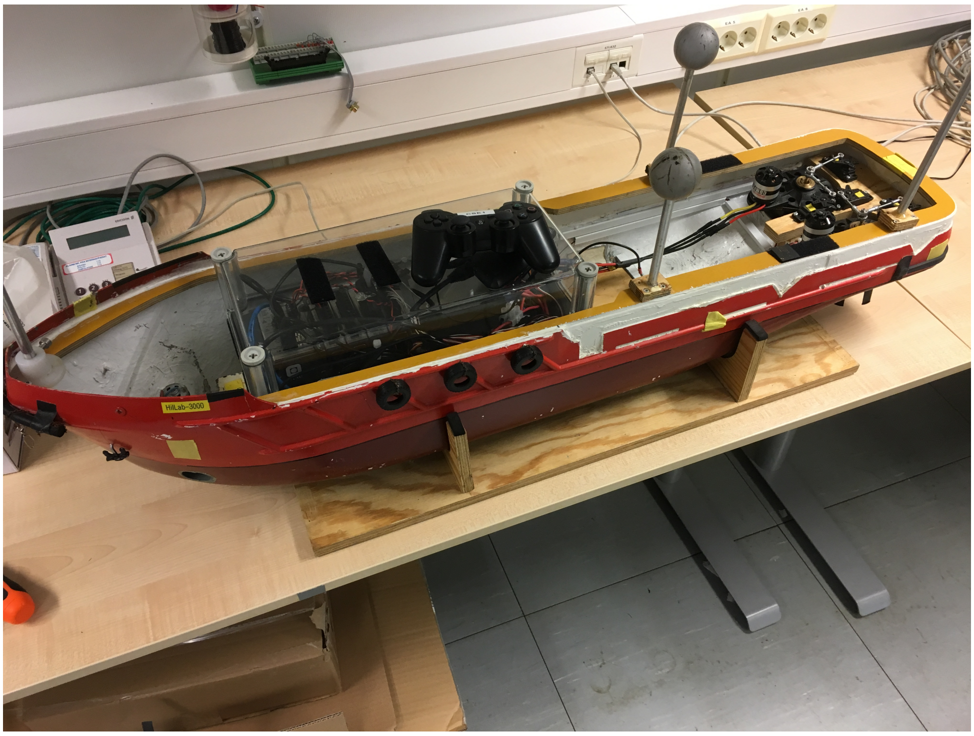

Figure 1.1: The C/S Enterprise I model vessel

The CSEI vessel is shown in Figure 1.1. It is 1m long (L_{pp}) and weighs 14.79 kg. It has 3 actuators, one bow thruster and two Voight Schneider propellers at the aft. It was originally built in 2009, but later modified in 2011 (NTNU (2016)). The vessel is used for experiments in the MC Lab for both Master's and PhDs students.

For testing of the controllers in full-scale a vessel model of R/V Gunnerus is used in this thesis. The modelled vessel measures 29.8 m (L_{pp}) and weighs 743888.94 kg. R/V Gunnerus is the NTNU reasearch vessel and is used for many different applications including control system design and biological research. The real vessel also has a bow thruster, but its main actuators are two azimuth thrusters. A picture of the vessel is shown in Figure 1.2.

Using the simulation models for each vessel, the input to the models will be thrust forces and moment. Thrust allocation will only be applied for physical experiments in the MC Lab. Both models are taken directly using NTNU (2016) and Perez and Fossen (2004) for CSEI and R/V Gunnerus respectively.

Figure 1.2: Photo of R/V Gunnerus taken from the ADPRC'16

1.1.8 AMOS DP Research Cruise 2016

During two weeks of October and November 2016 a sea trial in cooperation between NTNU and Kongsberg Maritime (KM) called the AMOS DP Research Cruice 2016 (ADPRC'16) was held. This was a first-of-its-kind sea trial were NTNU granted KM access to R/V Gunnerus for testing their DP and autopilot systems. In return PhD candidates in addition to myself were able to test different controllers, observers and autopilot models for the full scale vessel using the KM control system on board. The experiences from these cruises will be used in this thesis to improve the autopilot focusing on how to prevent the implementation issues that occurred and how to improve the controllers. Figure 1.2, is taken during the last cruise and shows the research vessel in Brekstad port.

1.2 Objective and Scope

The topics presented above are well known and widely used in marine control applications. However, there is a slight gap in the study of normalized adaptive autopilot designs. By applying the experience gained during APDRC'16 and using existing literature this topic will be investigated in order to prove if normalized adaptive autopilots may reduce the cost on a surface vessel while still being able to perform at a high level. The scopes are throughout the thesis divided into:

1. Perform a literature survey on the relevant subjects
2. Establish an appropriate underactuated simulation model for R/V Gunnerus for medium-high speeds.
3. Assess, simulate and compare different adaptive control design models for autopilot design.
4. Discuss normalization and scaling methods and how it affects the control behaviour.
5. Study the MRAC design, normalize the controllers and discuss their applicability to scaling.
6. Assess and simulate a signal-based/kinematic observer design with respect to the autopilot design.
7. Implement path generation and add guidance as an outer loop in the autopilot using the ILOS method for path-following purposes.
8. Define test scenarios and perform simulations in MATLAB/Simulink, HIL and if possible of practical experiments in the MC Lab.

1.3 Limitations

The thesis is limited to underactuated surface vessels moving in 3 DOFs, adaptive controllers and signal-based observers. Two vessel models will be used for simulations and for comparison of the results. These vessels are CSEI and R/V Gunnerus. Both models will be tested in MATLAB/Simulink but, only the CSEI will be used in HIL and in laboratory exercises as no model vessel exists for R/V Gunnerus.

The CSEI was broken for almost the entire semester as well as being used in lab exercises for an advanced marine control course. This meant that there were not enough time for physical experiments. In addition, the model parameters in the given model were inaccurate and some even completely wrong, resulting in that some modifications needed to be done in order to get stable maneuvering models. The absence of physical tests opportunities made the need of extensive HIL simulation less necessary. Since the same inaccurate vessel models were used in the HIL software as in MATLAB simulations yielding the same results, HIL was used only as proof of that the control system worked with the software that is used in the MC Lab.

1.4 Contributions of this Thesis

Apart from studying and presenting a less known topic within autopilot design this thesis includes practical contributions such as:

- Implementation of a working low-cost normalized adaptive autopilot model for CSEI, including path generation, tracking and a signal-based observer. The autopilot can be scaled for application on a full scale simulation model of R/V Gunnerus.

1.5 Outline of the Thesis

The rest of this thesis will be organized as follows:

Chapter 2: describes how the modeling of kinetics and kinematics are done. Further, the maneuvering models will be derived and simulations of these designs will be tested in order to find the most suited models for this thesis. Finally, the normalization will be applied for the maneuvering models.

Chapter 3: Presents the procedure of simulations, HIL testing and full scale test. In addition, the methods for monitoring and gathering of results are discussed.

Chapter 4: will look closer into the kinematic observer complete with robustification. Stability properties will be discussed and results from simulations will also be presented.

Chapter 5: presents various MRAC designs for the autopilot model with stability proofs, robustification techniques and results from simulations using MATLAB/Simulink and HIL tests.

Chapter 6: extends the autopilots control system into including path generation, path-following and path-tracking of underactuated marine vessels. Relevant simulations and proof of HIL testing will also be presented.

Chapter 7: analyses the overall results of the thesis in a discussion.

Chapter 8: concludes the thesis based on the discussion and also provides topics for further work.

Chapter 2

Mathematical Modeling

In order to develop mathematical models for the two target vessels their operational purposes must be determined. In Section 1.1.3 the different classification of these models were presented according to Fossen (2011) and Sørensen (2013). For an autopilot a CPM is preferred as it is less computationally expensive and sufficient for controlling purposes. As both target vessels are operating at the surface only, a natural simplification is to reduce the 6 DOF simulation model to a 3 DOF model which the maneuvering models will be derived from. Fossen (2011) and Fossen (1994) will be used as a base for model derivation.

Mathematical models for marine vessels must include both dynamic theory and hydrostatics. Dynamics is usually divided into kinematics and kinetics. Kinematics describes motion from a geometrical point of view; defining coordinate frames, how they relate and how they move with respect to one another. Kinetics however, focuses on how forces affects the motions of a vessel. It is common to model moving vessels as mass-spring-damper-systems. Hydrostatics focuses on the restoring (or spring) forces caused by gravity and buoyancy, based on *Archimedes Principle*. As the vessels are assumed to be moving at a constant speed, the mass and damper terms are found through maneuvering theory. It is worth noticing that added mass, Coriolis forces, linear and non-linear damping are all included in the mathematical models.

For a underactuated surface vessel, the main issue is how to handle the sway dynamics. As presented in Section 1.1.2 a constant thrust in surge in adition to control input in yaw is sufficient to steer the ship along a desired path. The 1 DOF Nomoto model (Nomoto K. and Hirano, 1957) is one of the most widely used autopilot design models and builds on this principle. The second order Nomoto model was first derived from a 2 DOF linearized sway-yaw subsystem developed by Clarke and Horn (1997) and Fossen (1994). Further simplifications resulted into a first order model, depending on only a time constant and a controller gain. Extensions to the Nomoto models have been made to include non-linear effects as presented in Norrbin (1963) and Bech (1969).

Determining which of the maneuvering models to chose and which extensions are to be included, is done by assessment of directional stability. The models that can keep the same heading after disturbances are said to be directionally stable and is explained in Fossen (2011, Chapter 12). In Nomoto (1972) the Nomoto model is discussed in light of directional stability. In Saout and Ananthakrishnan (2011) a similar study for the coupled sway-yaw motion is done for underwater vehicle close to the free surface.

For some path-following and path-tracking purposes and for maneuvering, an additional input in surge is required in order to control the velocity. Due to starboard-port symmetry no coupling effects exists between surge and the two other DOF (sway and yaw). Hence, the surge equation can be treated separately to the 2 DOF sway-yaw subsystem and the Nomoto models.

Finally, the maneuvering models will be normalized in order to facilitate scaling between similar vessels with different sizes. Two such techniques are known as Prime-scaling (SNAME, 1950) and Bis-scaling (Norrbin, 1971) and can be applied for derivation of scalable controller design. In this thesis the focus will be on the Bis-scaled normalization method.

2.1 Derivation of Mathematical Vessel Models

In this section the vessel kinematics and kinetics will be described according to Fossen (1994) and Fossen (2011), starting with a 6 DOF model before simplifying it to fit the purpose of this thesis. The notation throughout will follow Fossen's Robot-like Vectorial Model for Marine Crafts first introduced in Fossen (1991).

2.1.1 Kinematics

There are several ways to look at the motion of a surface vessel. One way to look at it is by studying the vessel from a Earth-centered coordinate frame. The Earth-centered Earth-fixed (ECEF) frame has its origin at the center of the Earth. Its x-axis is pointing through the intersection of 0° longitude and latitude, the z-axis points straight upwards and the y-axis lies in the direction which fulfills the right-hand-rule. This frame rotates along with the Earth, which for marine purposes can be ignored. Instead, an Earth-centered Inertial (ECI) frame is used. It is a non-accelerating coordinate system in which Newton's laws of motion does apply. The ECI frame has its origin and z-axis as for the ECEF frame, but its x-axis points through the vernal equinox. The y-axis points as in the ECEF frame and is placed such that the right-hand-rule is satisfied.

A more common way for looking at motion is using a geographical frame with origin on the surface of the Earth. The North-East-Down (NED) frame defines the x-axis as true North, y-axis as East and z-axis pointing downwards towards the center of Earths reference ellipsoid (World Geodetic System, 1984). The body-fixed (BODY) frame has its origin midships on the mean waterline, x-axis pointing straight forward, y-axis pointing starboard and z-axis is defined positive downwards.

Having defined the coordinate systems, the 6 DOF kinematic differential equation relating position in NED coordinates to velocities in body frame can be written as

$$\dot{\boldsymbol{\eta}} = \mathbf{J}(\eta)\boldsymbol{\nu} \tag{2.1}$$

where,

$$\boldsymbol{J}(\boldsymbol{\eta}) = \begin{bmatrix} \boldsymbol{R}_b^n(\boldsymbol{\theta}_{nb}) & 0_{3\times3} \\ 0_{3\times3} & \boldsymbol{T}_\Theta(\boldsymbol{\theta}_{nb}) \end{bmatrix} \tag{2.2}$$

is the 6 DOF velocity transformation matrix. $\boldsymbol{\eta}$ and $\boldsymbol{\nu}$ represents the the position in NED frame and the body-fixed velocities, respectively and they are written out as shown in (2.3) and (2.4) below.

$$\boldsymbol{\eta} = [\boldsymbol{p}_{b/n}^n \boldsymbol{\Theta}_{nb}]^\top = [N, E, D, \phi, \theta, \psi]^T \tag{2.3}$$

$$\boldsymbol{\nu} = [\boldsymbol{v}_{b/n}^b \boldsymbol{\omega}_{b/n}^b]^\top = [u, v, w, p, q, r]^T \tag{2.4}$$

$\boldsymbol{p}_{b/n}^n$ represents the NED coordinates, $\boldsymbol{\Theta}_{nb}$ the attitude in Euler angles while $\boldsymbol{v}_{b/n}^b$ and $\boldsymbol{\omega}_{b/n}^b$ represent the linear and angular velocity decomposed in BODY coordinates.

The two velocity transformation matrices in (2.2) build on Euler's Theorem of Rotation (explained in Fossen (2011)) which states the relative orientation between two different frames can be made by rotating one of them with respect to the other. A rotation matrix $\boldsymbol{R}_{\lambda,\beta}$ will rotate the frames according to a rotation (β) about the λ axis as shown in (2.5), where

$$\boldsymbol{R}_{\lambda,\beta} = \boldsymbol{I}_{3\times3} + sin(\beta)\boldsymbol{S}(\boldsymbol{\lambda}) + [1 - cos(\beta)]\boldsymbol{S}^2(\boldsymbol{\lambda}). \tag{2.5}$$

Here, $\boldsymbol{\lambda}$ is the unit vector parallel to the axis of rotation and $\boldsymbol{S}(\boldsymbol{\lambda})$ is a skew-symmetric matrix defined as (2.6)

$$\boldsymbol{S}(\boldsymbol{\lambda})_{3\times3} = -\boldsymbol{S}^\top(\boldsymbol{\lambda}) = \begin{bmatrix} 0 & -\lambda_3 & \lambda_2 \\ \lambda_3 & 0 & -\lambda_1 \\ -\lambda_2 & \lambda_1 & 0 \end{bmatrix}. \tag{2.6}$$

For the principal rotations $\boldsymbol{\lambda}$ is set to $[1,0,0]^\top$, $[0,1,0]^\top$ and $[0,0,1]^\top$ representing the x-, y- and z-axis respectively. These are paired with the rotations (β) with respect to the axis (Φ, Θ, Ψ). The linear velocity transformation is obtained by multiplying all principal rotation matrices resulting in (2.7)

$$\boldsymbol{R}_b^n(\boldsymbol{\Theta})_{3\times3} = \begin{bmatrix} \mathrm{c}\psi\mathrm{c}\theta & -\mathrm{s}\psi\mathrm{c}\phi + \mathrm{c}\psi\mathrm{s}\theta\mathrm{s}\phi & \mathrm{s}\psi\mathrm{s}\phi + \mathrm{c}\psi\mathrm{c}\phi\mathrm{s}\theta \\ \mathrm{s}\psi\mathrm{c}\theta & \mathrm{c}\psi\mathrm{c}\phi + \mathrm{s}\phi\mathrm{s}\theta\mathrm{s}\psi & -\mathrm{c}\psi\mathrm{s}\phi + \mathrm{s}\theta\mathrm{s}\psi\mathrm{c}\phi \\ -\mathrm{s}\theta & \mathrm{c}\theta\mathrm{s}\phi & \mathrm{c}\theta\mathrm{c}\phi \end{bmatrix}, \tag{2.7}$$

where $\mathrm{s}(\cdot)$ and $\mathrm{c}(\cdot)$ are short for the sine and cosine functions, respectively. The inverse matrix can be obtained multiplying the transposed matrices (of the principal roptations) together according to zyx convention (Fossen, 2011)

$$\boldsymbol{R}_b^n(\boldsymbol{\Theta_{nb}})^{-1} = \boldsymbol{R}_b^n(\boldsymbol{\Theta_{nb}})^T. \tag{2.8}$$

The angular velocity transformation matrix $T_{\Theta_{nb}}$ can be defined from $\boldsymbol{\omega}_{\boldsymbol{b/n}}^{\boldsymbol{b}}$ and the principle rotation matrices discussed above, resulting in

$$\boldsymbol{\omega}_{\boldsymbol{b/n}}^{\boldsymbol{b}} = \begin{bmatrix} \dot{\phi} \\ 0 \\ 0 \end{bmatrix} + \boldsymbol{R}_{x,\phi}^\top \begin{bmatrix} 0 \\ \dot{\theta} \\ 0 \end{bmatrix} + \boldsymbol{R}_{x,\phi}^\top \boldsymbol{R}_{y,\theta}^\top \begin{bmatrix} 0 \\ 0 \\ \dot{\psi} \end{bmatrix} := \boldsymbol{T}^{-1}(\boldsymbol{\Theta}_{nb})\dot{\boldsymbol{\Theta}}_{nb}. \tag{2.9}$$

By inverting the matrix $(\boldsymbol{\Theta}_{nb}^{-1})$ in the last expression of 2.9, $T_{\Theta_{nb}}$ is obtained and expressed as

$$\boldsymbol{T}(\boldsymbol{\Theta_{nb}})_{3\times3} = \begin{bmatrix} 1 & \mathrm{s}\phi\mathrm{t}\theta & \mathrm{c}\phi\mathrm{t}\theta \\ 0 & c\phi & -\mathrm{s}\phi \\ 0 & \mathrm{s}\phi/\mathrm{c}\theta & \mathrm{c}\theta/\mathrm{c}\phi \end{bmatrix}, \tag{2.10}$$

where $\mathrm{t}(\cdot)$ is short for the tangent function.

Having defined the angular rotation matrix, the derivative of the linear velocity transformation matrix can be obtained using

$$\dot{\boldsymbol{R}}_b^n(\boldsymbol{\Theta_{nb}}) = \boldsymbol{R}_b^n \boldsymbol{S}(\boldsymbol{\omega}_{\boldsymbol{b/n}}^{\boldsymbol{b}}). \tag{2.11}$$

In (2.11) $\boldsymbol{S}(\boldsymbol{\omega}_{\boldsymbol{b/n}}^{\boldsymbol{b}})$ is like (2.6) but where $[\lambda_1, \lambda_2, \lambda_3]$ is replaced by the body-fixed angular velocities $[p, q, r]$.

The problem with defining rotations using Euler angles as above is that there exist singularities. To avoid this problem Chou (1992) introduced quaternions which are complex number consisting of a real part η and a vector of imaginary numbers $\boldsymbol{\epsilon}$. In vector form the unit quaternions are defined using (2.5) defining $\boldsymbol{q}$ as

$$\boldsymbol{q}_b^n = \begin{bmatrix} \eta \\ \epsilon_1 \\ \epsilon_2 \\ \epsilon_3 \end{bmatrix} = \begin{bmatrix} \eta \\ \boldsymbol{\epsilon} \end{bmatrix} = \begin{bmatrix} \cos(\frac{\beta}{2}) \\ \boldsymbol{\lambda}\sin(\frac{\beta}{2}) \end{bmatrix}, \tag{2.12}$$

where $|\boldsymbol{q}|_2 = 1$. Using quaternions the transformation matrices (2.7) and (2.10) transform into

$$\boldsymbol{R}_b^n(\boldsymbol{q})_{3\times3} = \begin{bmatrix} 1-2(\epsilon_2^2+\epsilon_3^2) & 2(\epsilon_1\epsilon_2-\epsilon_3\eta) & 2(\epsilon_1\epsilon_3+\epsilon_2\eta) \\ 2(\epsilon_1\epsilon_2+\epsilon_3\eta) & 1-2(\epsilon_1^2+\epsilon_3^2) & 2(\epsilon_2\epsilon_3-\epsilon_1\eta) \\ 2(\epsilon_1\epsilon_3-\epsilon_2\eta) & 2(\epsilon_2\epsilon_3+\epsilon_1\eta) & 1-2(\epsilon_1^2+\epsilon_2^2) \end{bmatrix} \tag{2.13}$$

and

$$\boldsymbol{T}(\boldsymbol{q})_{4\times3} = \begin{bmatrix} -\epsilon_1 & -\epsilon_2 & -\epsilon_3 \\ \eta & -\epsilon_3 & \epsilon_2 \\ \epsilon_3 & \eta & -\epsilon_1 \\ -\epsilon_2 & \epsilon_1 & \eta \end{bmatrix}, \tag{2.14}$$

which in turn modifies (2.11) transform into

$$\dot{\boldsymbol{q}}_b^n = \boldsymbol{T}(\boldsymbol{q}_b^n)\boldsymbol{\omega}_{\boldsymbol{b/n}}^{\boldsymbol{b}}. \tag{2.15}$$

and the kinematic equation(2.1) into

$$\dot{\boldsymbol{\eta}} = \mathrm{J}_q(\mathrm{q})\boldsymbol{\nu}. \tag{2.16}$$

2.1.2 Kinetics

The study of kinetics introduces the marine craft equations. In order to complete these equations rigid-body forces, hydrostatics and hydrodynamics must be studied. Starting with rigid-body kinetics (Fossen, 2011, Chapter 2) a 6 DOF vessel can be described as

$$\boldsymbol{M}_{RB}\dot{\boldsymbol{\nu}} + \boldsymbol{C}_{RB}(\boldsymbol{\nu})\boldsymbol{\nu} = \boldsymbol{\tau}_{RB}, \tag{2.17}$$

where

$$\boldsymbol{M}_{RB} = \begin{bmatrix} m\boldsymbol{I}_{3\times3} & -m\boldsymbol{S}(\boldsymbol{r}_g^b) \\ -m\boldsymbol{S}(\boldsymbol{r}_g^b) & \boldsymbol{I}_b \end{bmatrix} \tag{2.18}$$

is the rigid-body mass matrix (m is for mass, I_b denotes mass moments of Inertia),

$$\boldsymbol{C}_{RB} = \begin{bmatrix} m\boldsymbol{S}(\boldsymbol{\nu}_2) & -m\boldsymbol{S}(\boldsymbol{\nu}_2)\boldsymbol{S}(\boldsymbol{r}_g^b) \\ -m\boldsymbol{S}(\boldsymbol{r}_g^b)\boldsymbol{S}(\boldsymbol{\nu}_2) & \boldsymbol{S}(\boldsymbol{I}_b\boldsymbol{\nu}_2), \end{bmatrix} \tag{2.19}$$

is the rigid-body centripetal matrix (Fossen and Fjellstad, 1995). $\boldsymbol{\nu}$, is as in (2.4), while $\boldsymbol{\nu}_2 = [p, q, r]^\top$ and $\boldsymbol{r}_g^b$ are the angular velocities and the distance from the origin of the BODY frame to the center of gravity (CG) of the craft, respectively. $\boldsymbol{I_{3\times3}}$, is the unit matrix while $\boldsymbol{S}(\cdot)$ is a skew-symmetric matrix presented as (2.6). $\boldsymbol{\tau}$, is the rigid-body force vector.

The restoring terms are added to (2.17) by studying the hydrostatic forces (Fossen, 2011, Chapter 4). These includes effects of gravity and buoyancy (*Archimedes Principle*) written in vector notation (Fossen, 1991) as $\boldsymbol{g}(\boldsymbol{\eta}) + \boldsymbol{g}_0$, where the first term includes the restoring forces and the second includes the gravitational ones.

Assessing the hydrodynamics of the vessel using maneuvering theory (Fossen, 2011, Chapter 6) the last terms includes added mass forces $\boldsymbol{M}_A$, linear ($\boldsymbol{D}_{lin}(\boldsymbol{\nu})\boldsymbol{\nu}$) and nonlinear ($\boldsymbol{D}_{nl}(\boldsymbol{\nu})\boldsymbol{\nu}$) damping forces as well as Coriolis-Centripetal forces $\boldsymbol{C}_A(\boldsymbol{\nu})$.

Introducing other external forces acting on the vessel such as current-, wind- ($\boldsymbol{\tau}_{wind}$), waves- ($\boldsymbol{\tau}_{wave}$) and control input-forces ($\boldsymbol{\tau}$), the complete maneuvering equation can be written as

$$\begin{aligned} &\boldsymbol{M}_{RB}\dot{\boldsymbol{\nu}} + \boldsymbol{C}_{RB}(\boldsymbol{\nu})\boldsymbol{\nu} + \boldsymbol{M}_A\dot{\boldsymbol{\nu}}_r + \boldsymbol{C}_A(\boldsymbol{\nu}_r)\boldsymbol{\nu}_r + \boldsymbol{D}(\boldsymbol{\nu}_r)\boldsymbol{\nu}_r \\ &\qquad ... + \boldsymbol{g}(\boldsymbol{\eta}) + \boldsymbol{g}_0 = \boldsymbol{\tau} + \boldsymbol{\tau}_{wind} + \boldsymbol{\tau}_{wave}. \end{aligned} \tag{2.20}$$

Note that the current forces in (2.20) are included in the relative velocity components $\boldsymbol{\nu}_r = \boldsymbol{\nu} - \boldsymbol{\nu}_c$, where $\boldsymbol{\nu}_c$ represents the constant irrotational current vector

$$\boldsymbol{\nu}_c = \begin{bmatrix} u_c & v_c & w_c & 0 & 0 & 0 \end{bmatrix}^\top. \tag{2.21}$$

As the current is assumed to be constant $\dot{\boldsymbol{\nu}}_c = \boldsymbol{0_{6\times1}}$ and $\dot{\boldsymbol{\nu}}_r = \dot{\boldsymbol{\nu}}$.

2.2 Maneuvering Models

For autopilot applications there is no need to include 6 DOFs in calculations. For surface vessels it is normal to reduce the model to motion in surge, sway and yaw. This is done under the assumption that motions in heave, roll and pitch are small. In this way the kinematic velocity transformation matrix (2.1) reduces to (Fossen, 2011)

$$\dot{\boldsymbol{\eta}} = \boldsymbol{R}_b^n(\psi)\boldsymbol{\nu}, \tag{2.22}$$

where $\boldsymbol{\eta} = [N, E, \psi]^T$, $\boldsymbol{\nu} = [u, v, r]^T$ and $\boldsymbol{R}_b^n(\psi)$ is called the 3 DOF rotation matrix and is expressed as follows:

$$\boldsymbol{R}_b^n(\psi) = \begin{bmatrix} \cos(\psi) & -\sin(\psi) & 0 \\ \sin(\psi) & \cos(\psi) & 0 \\ 0 & 0 & 1 \end{bmatrix}. \tag{2.23}$$

This reduction of DOFs applies also for the kinetics. Further simplifications are made by summing the mass components, the linear and nonlinear damping and the Coriolis-Centripetal terms as well as neglecting the hydrostatic forces as they are zero in the horizontal plane. This implies that (2.20) can be written as

$$\boldsymbol{M}\dot{\boldsymbol{\nu}} + \boldsymbol{C}(\boldsymbol{\nu}_r)\boldsymbol{\nu}_r + \boldsymbol{D}(\boldsymbol{\nu}_r)\boldsymbol{\nu}_r = \boldsymbol{\tau} + \boldsymbol{\tau}_{wind} + \boldsymbol{\tau}_{wave}, \in \mathbb{R}^3, \tag{2.24}$$

where

$$\boldsymbol{M} = \begin{bmatrix} m - X_{\dot{u}} & 0 & 0 \\ 0 & m - Y_{\dot{v}} & mx_g - Y_{\dot{r}} \\ 0 & mx_g - Y_{\dot{r}} & I_z - N_{\dot{r}} \end{bmatrix} \tag{2.25}$$

is the combined rigid-body mass and added mass terms. $X_{\dot{u}}$, $Y_{\dot{u}}$, $Y_{\dot{r}}$ and $N_{\dot{r}}$ are added mass components and mx_g is cross terms of the mass moment. The damping matrix including both linear and nonlinear damping becomes (Faltinsen and Sortland, 1987)

$$\boldsymbol{D}(\boldsymbol{\nu}_r) = \begin{bmatrix} -X_u - X_{|u|u}|u_r| & 0 & 0 \\ 0 & -Y_v - Y_{|v|v}|v_r| & -Y_r - Y_{|v|r}|v_r| \\ 0 & -N_v - X_{|v|v}|v_r| & -N_r - N_{|v|r}|v_r| \end{bmatrix}, \tag{2.26}$$

and at last the 3 DOF simplified Coriolis matrix becomes

$$\boldsymbol{C}(\boldsymbol{\nu}_r) = \begin{bmatrix} 0 & 0 & -(m - Y_{\dot{v}})v - (mx_g - Y_{\dot{r}})r \\ 0 & 0 & (m - X_{\dot{u}})u_r \\ (m - Y_{\dot{v}})v + (mx_g - Y_{\dot{r}})r & (X_{\dot{u}} - Y_{\dot{v}})u_r & (mx_g - Y_{\dot{v}})u_r \end{bmatrix}. \tag{2.27}$$

It is common to add the damping and coriolis matrices together as they their effects on the craft are often hard to separate. This is usually done by (Fossen, 2011)

$$\boldsymbol{N}(\boldsymbol{\nu}_r) = \boldsymbol{D}(\boldsymbol{\nu}_r) + \boldsymbol{C}(\boldsymbol{\nu}_r), \tag{2.28}$$

resulting in

$$\boldsymbol{M}\dot{\boldsymbol{\nu}} + \boldsymbol{N}(\boldsymbol{\nu}_r)\boldsymbol{\nu}_r = \boldsymbol{\tau}, \in \mathbb{R}^3. \tag{2.29}$$

Due to starboard and port symmetry Fossen (2011) suggests that the surge motion is assumed decoupled from sway-yaw and that they may be treated as separate subsystems. The surge speed model can then be written as

$$(m - X_{\dot{u}})\dot{u}_r - X_u u_r - X_{|u|u} u_r = \tau_x. \tag{2.30}$$

The sway and yaw terms can be written as (2.29), but where the equations now describe a 2 DOF system where $\boldsymbol{\eta_r} = [y_r, \psi]^\top$ and $\boldsymbol{\nu}_r = [u_r, r]^\top$. The first columns and rows of (2.25), (2.26) and (2.27) are hence removed resulting in the sway-yaw subsystem (Clarke and Horn, 1997) below

$$\boldsymbol{M}\dot{\boldsymbol{\nu}} + \boldsymbol{N}(\boldsymbol{\nu}_r)\boldsymbol{\nu}_r = \boldsymbol{\tau}, \in \mathbb{R}^2. \tag{2.31}$$

2.2.1 Linearized Models for Autopilot Design

The 2 DOF model from (2.31) can be further simplified to obtain a simpler maneuvering model. One way to do that is by linearizing it about the cruise speed (u_0) as the vessel motion is an important assumption in deriving the maneuvering model. With linearization the model become

$$\boldsymbol{M}\dot{\boldsymbol{\nu}} + \boldsymbol{N}(u_0)\boldsymbol{\nu}_r = \boldsymbol{\tau}. \tag{2.32}$$

In (2.32), only linear damping and linearized coriolis terms are present in the $\boldsymbol{N}(u_0)$ term by application of (2.28). The 2 DOF linear damping and coriolis matrices are shown in (2.33) and (2.34):

$$\boldsymbol{D}(\boldsymbol{\nu}_r) = \begin{bmatrix} -Y_v & -Y_r \\ -N_v & -N_r \end{bmatrix}, \tag{2.33}$$

$$\boldsymbol{C}(\boldsymbol{\nu}_r) = \begin{bmatrix} 0 & (m - X_{\dot{u}})u_0 \\ (X_{\dot{u}} - Y_{\dot{v}})u_0 & (mx_g - Y_{\dot{v}})u_0 \end{bmatrix}. \tag{2.34}$$

Note that the term in the lower left corner of (2.34) is a destabilizing moment called the Munk moment. In many cases $\boldsymbol{\tau}$ is written as a function of rudder angle

$$\boldsymbol{\tau} = \boldsymbol{b}\delta, \tag{2.35}$$

where $\boldsymbol{b}$ is a gain and δ the rudder angle.

2.2.2 Nomoto Models

If only yaw rate (r) is chosen as output of the 2 DOF state-space representation of (2.32) a 1 DOF model is obtained. By applying the *Laplace transformation* of this system the following equation is obtained

$$\frac{r}{\delta}(s) = \frac{K(1 + T_3 s)}{(1 + T_1 s)(1 + T_2 s)}. \tag{2.36}$$

$T_i (i = 1, 2, 3)$ are time constants and K is the yaw gain from the $\boldsymbol{b}$ vector in (2.35). A similar model can be obtained for sway motion, but the gain and T_3 will be different from the yaw model. Integrating the model (dividing with s in the *Laplace* domain) the second order transfer function representing the Nomoto model is obtained in the same way as done by Nomoto K. and Hirano (1957):

$$\frac{\psi}{\delta}(s) = \frac{K(1 + T_3 s)}{s(1 + T_1 s)(1 + T_2 s)}, \tag{2.37}$$

where ψ is the desired heading. Introducing an equivalent time constant $T = T_1 + T_2 - T_3$, (2.37) is reduced to a first order model

$$\frac{\psi}{\delta}(s) = \frac{K}{s(1 + Ts)}. \tag{2.38}$$

Transferred back into time-domain (2.37) and (2.38) can be written as

$$T_1 T_2 \psi^{(3)} + (T_1 + T_2)\ddot{\psi} + \dot{\psi} = K(\delta + T_3\dot{\delta}) \tag{2.39}$$

and

$$T\ddot{\psi} + \dot{\psi} = K\delta \tag{2.40}$$

2.2.3 Adding Nonlinear Characteristics

Sometimes it is preferred to include nonlinear terms in the Nomoto models. The $\dot{\psi}$ terms in (2.39) and (2.40) are replaced by a nonlinear function of r (as $\dot{\psi} = r$)

$$H_N(r) = n_3 r^3 + n_2 r^2 + n_1 r + n_0 \tag{2.41}$$

$$H_B(r) = b_3 r^3 + b_2 r^2 + b_1 r + b_0 \tag{2.42}$$

The first one (2.41), developed by Norrbin (1963) added nonlinearities to the first order expression. The second equation (2.42), developed by Bech (1969) did the same for the second order model. Note that the linear models are obtained by setting $H_N(r) = H_B(r) = r$. Concerning the constant values b_i and n_i, they depend on the maneuver characteristics of the target vessels used in this thesis. Due to ship symmetry the terms b_0 and b_2 are assumed to be zero, while b_1 changes sign if it's course-stable (positive) or unstable (negative). Their values can be determined through Bech's spiral maneuver (Fossen, 2011, Chapter 12.1.1). Normalizing Bech's parameter values, results in the equivalent parameters according to Norrbin's theory. This means that for course-stable vessels n_1 is 1 and for course-unstable vessels n_1 is -1.

2.3 Normalization

Two scaling laws are described in Fossen (2011, Chapter 7.2.5). The first one is called the Prime system (SNAME, 1950). The second is called the Bis system (Norrbin, 1971). To show the differences in scaling the non-dimensional time is used as an example

$$t' = \frac{L_{pp}}{U}, \tag{2.43a}$$

$$t" = \sqrt{\frac{L_{pp}}{g}}. \tag{2.43b}$$

The Bis scaling (2.43b) is the method chosen because of its overall validity, even at slow speed, where the Prime system (2.43a) has a singularity. A non-dimensional model is introduced in order to easier transfer it to other vessel models. It can be a great advantage to perform tests of controllers on a model vessel before trying them out in full scale. The scaling should facilitate the implementation and tuning of the control systems made using the small model vessel in the laboratory.

2.3.1 Normalized Maneuvering Models

In order to normalize equations (2.30), (2.32), (2.39) or (2.40) all the components from the equations must be scaled according to (2.43), Table 2.1 and Fossen (2011, Chapter 7.2.5). For a floating ship all normalized values are scaled with a parameter $\mu = 1$, hence it is not included in the equations. In addition mass, inertia, forces and moments must be normalized using

Table 2.1: Normalization of parameters in surge, sway and yaw

	Surge (x)	Sway (y)	Yaw (ψ)	
$\boldsymbol{\xi}$	$x_{int} = \sqrt{\frac{L^3}{g}} x_{int}^{"}$	$y_{int} = \sqrt{\frac{L^3}{g}} y_{int}^{"}$	$\psi_{int} = \sqrt{\frac{L}{g}} \psi_{int}^{"}$	
$\boldsymbol{\eta}$	$x = Lx^{"}$	$y = Ly^{"}$	$\psi = \psi^{"}$	.
$\boldsymbol{\nu}$	$u = \sqrt{Lg} u^{"}$	$v = \sqrt{Lg} v^{"}$	$r = \sqrt{\frac{g}{L}} \psi^{"}$	
$\dot{\boldsymbol{\nu}}$	$\dot{u} = g\dot{u}^{"}$	$\dot{v} = g\dot{v}^{"}$	$\dot{r} = \frac{g}{L} \dot{r}^{"}$	

$$m = \rho \nabla m^{"} \tag{2.44a}$$

$$I = \rho \nabla L^2 I^{"} \tag{2.44b}$$

$$\tau_f = \rho g \nabla \tau_f^{"} \tag{2.44c}$$

$$\tau_m = \rho g \nabla L \tau_m^{"}. \tag{2.44d}$$

According to Fossen (2011) it is preferred to use dimensional time when simulating controllers. Hence, the states and inputs are kept dimensional, while the hydrodynamical coefficients stays nondimensional. For the 3 DOF model in (2.29), this results in:

$$(\boldsymbol{T}\boldsymbol{M}^{"}\boldsymbol{T}^{-1})\dot{\boldsymbol{\nu}} + \sqrt{\frac{g}{L}}(\boldsymbol{T}\boldsymbol{N}^{"}\boldsymbol{T}^{-1})\boldsymbol{\nu}_r = \frac{1}{m}\boldsymbol{T}^2\boldsymbol{\tau}, \tag{2.45}$$

where the mass, forces and moments are normalized according to (2.44). In vector form the components of (2.45) can be expressed by

$$\boldsymbol{M} = m\boldsymbol{T}^{-2}(\boldsymbol{T}\boldsymbol{M}^{"}\boldsymbol{T}^{-1}), \tag{2.46a}$$

$$\boldsymbol{N} = m\sqrt{\frac{g}{L}}\boldsymbol{T}^{-2}(\boldsymbol{T}\boldsymbol{N}^{"}\boldsymbol{T}^{-1}), \tag{2.46b}$$

where $T = \text{diag}([1, 1, \frac{1}{L}])$ is a transformation matrix for the relation between angular and translational motion. As described in Section 2.2 the velocity- and input- vectors in (2.45) are expressed as $\boldsymbol{\nu}_r = [u_r, v_r, r]^\top$, $\boldsymbol{\tau} = [\tau_X, \tau_Y, \tau_N]^\top$ and $\dot{\boldsymbol{\nu}}_r = \dot{\boldsymbol{\nu}}$.

Surge Speed Model

Using Table 2.1 and $m = \rho\nabla$ the surge subsystem from (2.30) can be normalized into

$$(m^{"} - X_{\dot{u}}^{"})\dot{u} - \sqrt{\frac{g}{L}}(X_u + X_{|u|u}|u_r|)^{"} u_r = \frac{1}{m}\tau_X, \tag{2.47}$$

where the damping term $d_u'' = (X_u + X_{|u|u}|u_r|)''$ is obtained by rearranging

$$d_u = m\sqrt{\frac{g}{L}}d_u''. \tag{2.48}$$

Note that the nonlinear term in d_u'' in (2.47) varies with the relative velocity. For maneuvering this velocity is assumed to be constant, resulting in constant damping parameters. The added mass term $X_{\dot{u}}$ is normalized as the mass in (2.44a).

Linearized Sway-Yaw Model

In terms of normalized coefficients (2.32) results in (2.45) with $T = \text{diag}([1, \frac{1}{L}])$, $\boldsymbol{\nu}_r = [v_r, r]^\top$, $\boldsymbol{\tau} = [\tau_Y, \tau_N]^\top$ and $\dot{\boldsymbol{\nu}}_r = \dot{\boldsymbol{\nu}}$. The mass, and the linearized terms for coriolis and damping are normalized as

$$\boldsymbol{M} = m\boldsymbol{T}^{-2}(\boldsymbol{T}\boldsymbol{M}''\boldsymbol{T}^{-1}), \tag{2.49a}$$

$$\boldsymbol{N} = m\sqrt{\frac{g}{L}}\boldsymbol{T}^{-2}(\boldsymbol{T}\boldsymbol{N}''(u_0'')\boldsymbol{T}^{-1}). \tag{2.49b}$$

Normalized Nomoto Models

The two Nomoto models (2.39) and (2.40) are relatively easy to normalize compared to the others as they only include time constants and a gain. The time constants are normalized as shown in (2.43b) and the Nomoto gain is scaled as described in Skjetne (2016)

$$K = \sqrt{\frac{g}{L}}K''. \tag{2.50}$$

(2.39) can now be written as

$$\frac{L}{g}T_1''T_2''\psi^{(3)} + \sqrt{\frac{L}{g}}(T_1'' + T_2'')\ddot{\psi} + \dot{\psi} = \sqrt{\frac{g}{L}}K''(\delta + T_3''\dot{\delta}), \tag{2.51}$$

and (2.40) as

$$\sqrt{\frac{L}{g}}T''\ddot{\psi} + \dot{\psi} = \sqrt{\frac{g}{L}}K''\delta. \tag{2.52}$$

If nonlinear modifications such as (2.41) or (2.42) were to replace $\dot{\psi}$ in (2.51) or (2.52), they do not have to be scaled.

2.3.2 Open-Loop Stability

Determining the open-loop stability for both the model vessel and the full scale target vessel is important when scaling the autopilot models. It can explain how the scaled vessel model behave compared to the actual vessel and will help in order to determine certain maneuvering characteristics.

If the state matrix in a state-space representation of a maneuvering model has positive poles, the vessel is said to be unstable. The vessel will not be able to handle any disturbances and must be avoided.

A moving vessel is said to be straight-line stable if its path after a disturbance in yaw still is straight (Fossen, 2011). This can mathematically be determined by looking at the poles of the state matrix describing the vessel dynamics (in state-space form). If the uncontrolled ($\delta = 0$) craft has at least one negative pole and the others are maximum zero, it is said to be straight-line stable. A more physical way of determining straight line stability is to check whether the yaw rate (r) converges to zero after the disturbance.

Some vessel models satisfy an even stricter condition. Directional stability (course stability) can be proven for a vessel if all the poles in the state matrix of the autopilot model are negative. Physically, this means that the vessel heading converges to the same as before the disturbance in yaw. Determining whether the vessel is course stable will for instance affect the coefficients in the nonlinear extension of the Nomoto models as shown in Section 2.2.3 describing fundamentally different maneuvering characteristics.

2.4 Numerical Values for CSEI

For the simulations to come the following parameters and equations were used for modeling the vessel dynamics of CSEI. Note that all these matrices are simplified versions of the ones discussed in the sections above. Because determining the model-based parameters is not a part of this thesis, the model taken directly from Perez and Fossen (2004), Fossen and Perez (2008) and the MC lab handbook (NTNU, 2016) along with all relevant hydrodynamical parameters.

2.4.1 Mass Matrix

For the assembly of the mass matrix the relevant values are presented in Table 2.2 and Table 2.3 and the 3 DOF mass matrix from (2.25) is calculated to be as in (2.53)

Table 2.2: General parameters for CSEI

Parameter	Value
m(mass)	14.79
x_g	0.0375
I_z	1.76

Table 2.3: Added mass parameters for CSEI

Parameter	Value
$X_{\dot{u}}$	-2.0
$Y_{\dot{v}}$	-1.0
$Y_{\dot{r}}$	0.0
$N_{\dot{v}}$	0.0
$N_{\dot{r}}$	-1.0

$$\boldsymbol{M} = \begin{bmatrix} 16.79 & 0 & 0 \\ 0 & 15.79 & 0.5546 \\ 0 & 0.5546 & 2.76 \end{bmatrix}. \tag{2.53}$$

2.4.2 Damping Matrix

The coefficients used for calculation of damping forces in vessel simulations are presented in Table 2.4 The damping matrix can be written as below

Table 2.4: Drag coefficients for CSEI

Parameter	Value
X_u	-0.6555
$X_{u\|u\|}$	0.3545
X_{uuu}	-3.787
Y_v	-1.33
$Y_{v\|v\|}$	-2.776
Y_{vvv}	-64.91
Y_{rv}	-0.805
N_r	-1.9
$N_{r\|r\|}$	-0.750
N_{rrr}	0
N_{vr}	0.08

$$\boldsymbol{D} = \begin{bmatrix} d_{11} & 0 & 0 \\ 0 & d_{22} & d_{23} \\ 0 & d_{32} & d_{33} \end{bmatrix}, \tag{2.54}$$

where the damping forces are calculated according to (2.55)

$$d_{11} = -X_u - X_{uu}u - X_{uuu}u^2, \tag{2.55a}$$

$$d_{22} = -Y_v - Y_{vv}v - Y_{vvv}v^2 - Y_{rv}|r|, \tag{2.55b}$$

$$d_{33} = -N_r - N_{rr}|r| - N_{rrr}r^2 - N_{vr}|v|. \tag{2.55c}$$

Above in (2.55), $\boldsymbol{\nu} = [u, v, r]^\top$ represents the velocity components. The cross terms d_{23} and d_{32} of (2.54) were not correctly implemented in the given vessel model and are set equal to zero in the simulations because determining the vessel dynamics is not part of this thesis.

2.4.3 Coriolis Matrix

Finally, a simplified version of the coriolis matrix (2.27) were assembled as follows

$$\boldsymbol{C} = \begin{bmatrix} 0 & 0 & c_{13} \\ 0 & 0 & c_{23} \\ -c_{13} & -c_{23} & 0 \end{bmatrix}, \tag{2.56}$$

were the two terms are calculated as

$$c_{13} = -(m - Y_{\dot{v}})v - (mx_g - Y_{\dot{r}})r, \tag{2.57a}$$

$$c_{23} = (m - X_{\dot{u}})u_r. \tag{2.57b}$$

2.5 Simulation Study of Maneuvering Models

For the autopilot design, linearized maneuvering models presented throughout Section 2.2 will be scaled and compared to the higher order maneuvering models through assessment of directional stability. Their sensitivity to scaling (from Section 2.3) will also be simulated. The simulations will be done for CSEI and then scaled in order to check their applicability of scaling parameters to fit the larger R/V Gunnerus vessel. For the derivation of the maneuvering models some modifications have been made to compensate for inaccuracies in the given vessel model for CSEI. This is because the hydrodynamical coefficients from NTNU (2016) are not accurate enough and some seem to be wrong. This will be specified throughout the next sections. After the simulations results are presented, a brief discussion will be done in order to determine the open-loop stability of the vessel.

2.5.1 Simulation Results using Decoupled Maneuvering Models

First, the decoupled maneuvering models from (2.30), (2.32), (2.39) and (2.40) will be compared to the corresponding DOF from the 3 DOF vessel model of CSEI (2.29). All simulations are run for 200 seconds (s) without any waves and current forces.The vessel model of CSEI is excited by steps of 0.5 N constant thrust in surge and 1 N step (20 s) in yaw. These input forces are summarized in Figure 2.1.

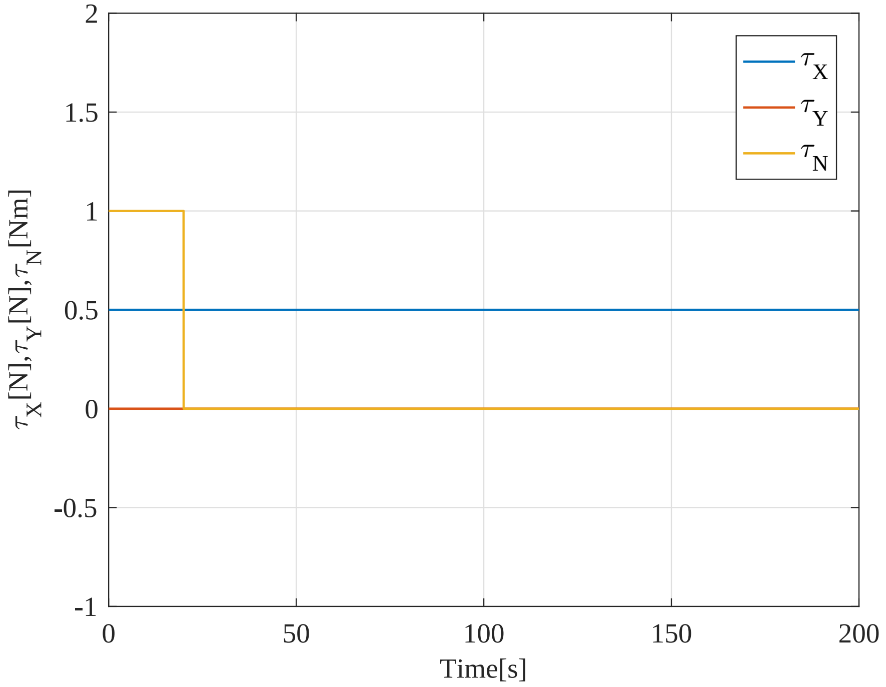

Figure 2.1: Thrust input for the CSEI maneuvering models

Starting with the surge speed model from (2.30), a third term is added to the damping (2.30) in order to make the model stable. This quadratic damping term makes the surge model stable and it is included in the 3 DOF vessel model as in (2.55a), making the two expressions equal. The problem is the second damping term that becomes negative for positive speed due to the sign of $X_{|u|u}$. In the surge speed model no coriolis terms are involved, resulting in when thrust exists in other DOFs in addition to surge the models will differ. The effect the coriolis terms has on the 3 DOF model compared to the surge speed model is shown in Figure 2.2.

The simulation of the linearized sway-yaw subsystem from (2.32) resulted in Figure 2.3, where it is clear that the two models are very different. The coriolis terms becomes more dominant when the nonlinear damping terms are removed. The linear damping terms are too small compared to the nonlinear terms and the model behaves very different. In addition the damping cross terms are set to zero as discussed in Section 2.4.2, making the coriolis matrix the only term acting in the coupled motion. This makes the destabilizing effect of the Munk moment (the term on lower left corner of (2.34) with no counter term and the vessel dynamics becomes more unstable. The 2 DOF model is also linearized about the surge speed of 0.42 $\mathrm{m/s}$ which is the cruise speed in surge, as shown in Figure 2.2 which adds to the differences.

Finally, the Nomoto models described by (2.39) and (2.40) are simulated for the same inputs as the sway-yaw system. The gains used in the 1st order model were $K = 0.45, T = 2$ and

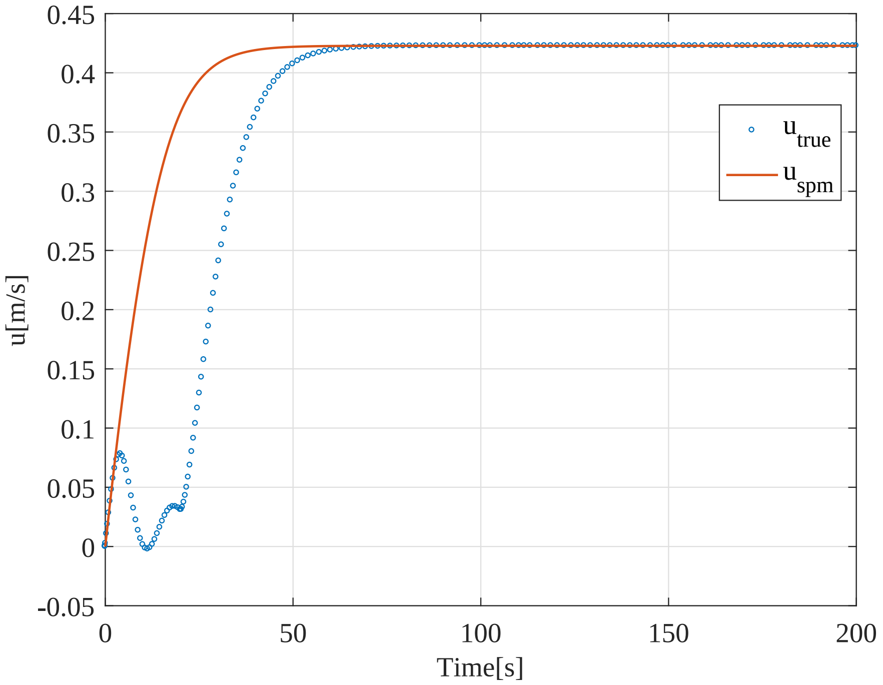

Figure 2.2: Surge speed model compared to real 3 DOF model

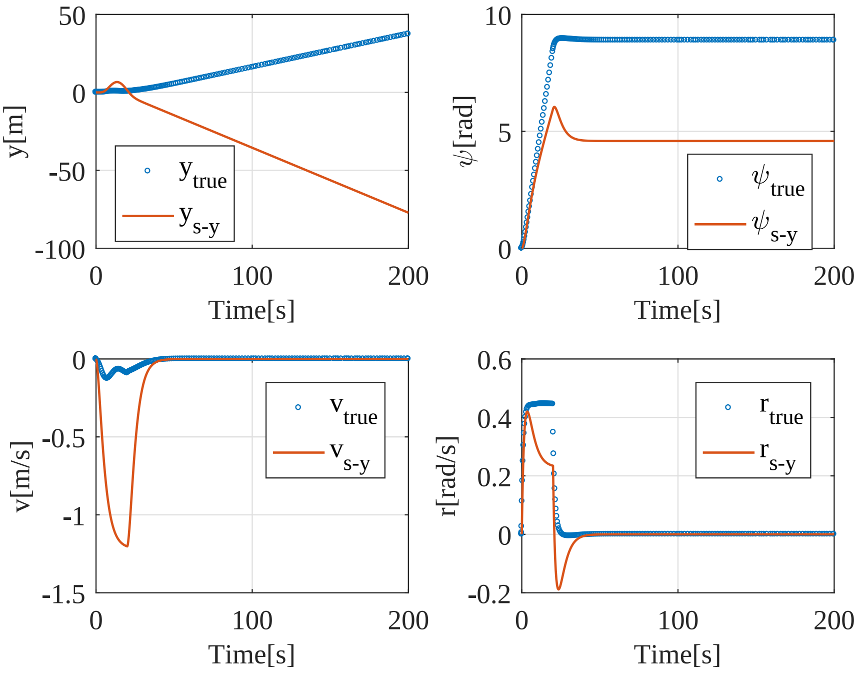

Figure 2.3: Sway-yaw subsystem compared to real 3 DOF model

similarly for the second order model were $K = 2, T_1 = 3, T_2 = 1, T_3 = 2$.

The plot in Figure 2.4 shows that the two models are very much alike and well suited for

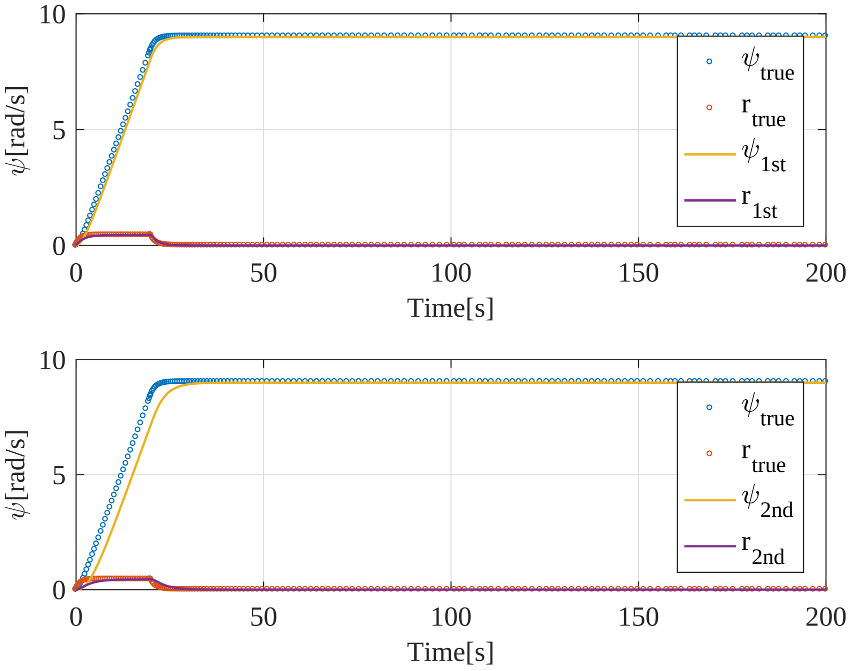

Figure 2.4: Nomoto models compared to real 3 DOF model

modeling the yaw motion of the 3 DOF vessel. This was expected as the second order model was designed such that $T_{1st} = T_1 + T_2 - T_3$ is satisfied for the 1st order model which simplifies tuning. The second order model should be more accurate than the 1st order model, but is harder to tune. Since this is only a test of the models, little effort were made in order to perfectionate the tuning. Figure 2.4 shows that the 1st order Nomoto model is sufficient in order to cope with the yaw dynamics and will therefore be used in scaling as it is simpler to work with. As the Nomoto models both perform better than the sway-yaw subsystem in addition of being much simpler to work and that they do not use any of the uncertain hydrodynamical coefficients from the given vessel model, the sway-yaw subsystem will not be scaled.

2.5.2 Simulation Results from Scaled Maneuvering Models

Now, using the scaling methods discussed in Section 2.3 the models used to obtain the results above are to be normalized. The scaled inputs are fed both to the scaled CSEI model and to the R/V Gunnerus vessel model in order to compare the behavior and rate each of the models. As in the previous section simulations were made to show which models showed the best behavior with respect to scaling and tuning. The scaled versions are therefore produced without excessive tuning to tell each model apart.

Using the bis-scaled model (2.47), with the same inputs as in the previous models (see Figure 2.1) gave the control inputs as shown in Figure 2.5. Note that τ_X is the force input in surge and

$\tau_N = b\delta$ represent the output from the 1st order scaled Nomoto model.

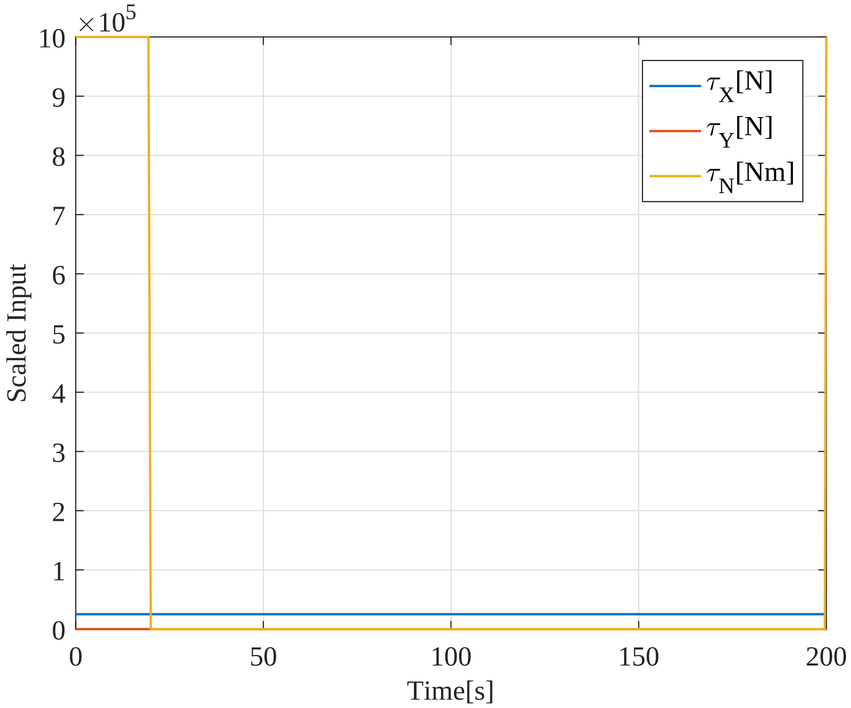

Figure 2.5: Thrust input for the scaled CSEI maneuvering models

The normalized surge speed model produced the response shown in Figure 2.6. As it is possible to see, the scaling do not seem to affect the response at all. The resulting surge speed model behaves in the same way for the CSEI and for the 6 DOF model which represents the full scale vessel of R/V Gunnerus.

For the simulation of the scaled 1st order Nomoto model the yaw moment of Figure 2.5 is used. The model is scaled according to (2.52) by scaling the time constant and gain according to (2.43b) and (2.50). The scaled Nomoto model yields the results presented in Figure 2.7. It shows that the model scaled the yaw response almost perfectly. Both the yaw angle (ψ) and the yaw rate (r) are very similar to the full scale vessel of R/V Gunnerus. Due to its simplicity and great initial results without a lot of tuning, the Nomoto model will be sufficient in order to make autopilot controllers that steer the ship with the correct heading.

2.5.3 Open-Loop Stability

In Section 2.3.2 two cases of open-loop stability for autopilot models were presented. Using the plots from the simulations above (Figures 2.3, 2.5 and 2.7), a similar stability analysis will be done for the two vessels used in this thesis.

In this analysis the step in yaw is treated as the disturbance on the vessel. Both vessels start with an initial heading of zero radians and at rest. During the disturbance the vessel starts turn-

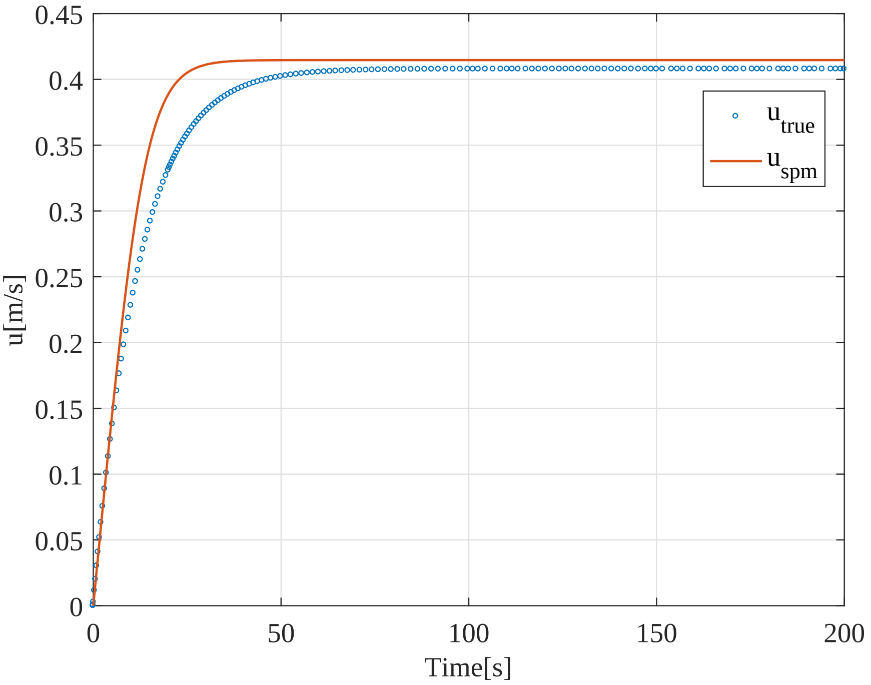

Figure 2.6: Scaled surge speed model compared to real 6 DOF model of R/V Gunnerus

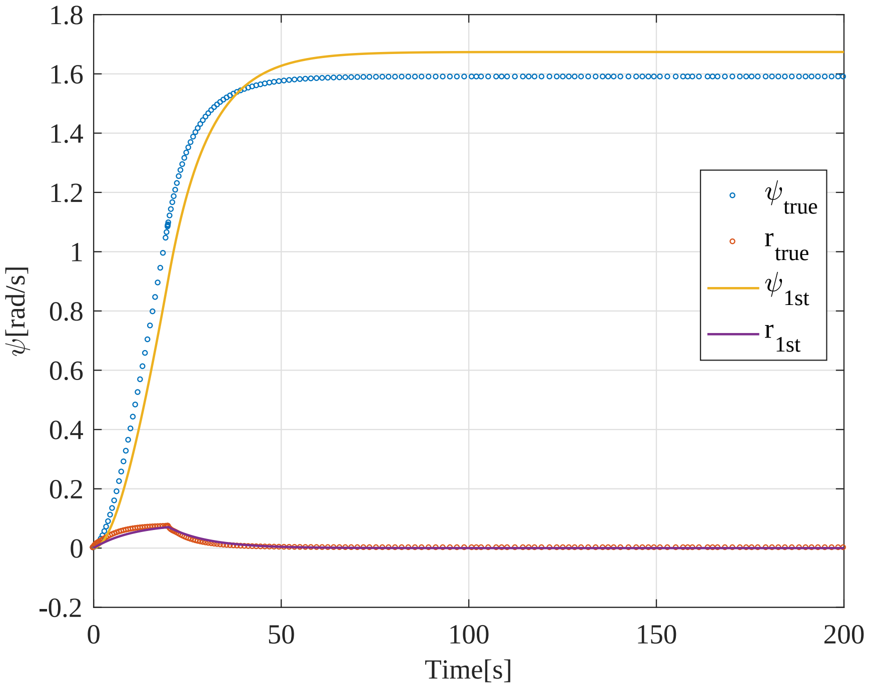

Figure 2.7: Scaled 1st order Nomoto model compared to real 6 DOF model of R/V Gunnerus

ing, increasing the yaw rates and angles. After 20 s. the yaw disturbance is over and the yaw rates converges to zero for both vessels. The heading angles, however, do not regain their initial values. According to Fossen (2011) this means that both vessels are proven straight-line stable, but not course stable.

Even though the vessel models cannot satisfy the strictest form of stability, the two vessels behave similarly. This means that the nonlinear extensions of the Nomoto models discussed in Section 2.2.3 will look similar. As the vessels are symmetric about starboard and port it can be determined from (2.41) and (2.42) that the terms b_2 and n_2 are zero. Being course unstable vessel the models yields $b_1, n_1 < 0$ for both.

2.6 Conclusions

To conclude this section, three maneuvering models were implemented and tested for their applicability to describe the dynamics of the model vessel and the best were compared with respect to scaling. The decoupled models for CSEI needed to be modified in order to be stable as the hydrodynamical coefficients were not optimal. This resulted in a smoother curve for the surge-speed model than for the actual 3 DOF vessel model, since the coriolis terms were not included.It comfirmed that the surge-speed model can be used separately from the sway-yaw subsystem, but due to problems with the hydrodynamical coefficients the linearized sway-yaw subsystem did not satisfy the expectations. The 1st order Nomoto model, however, proved sufficient in order to define the yaw dynamics of the model vessel. This will make the tuning process easier and allow the use of simpler heading control designs.

Scaling the CSEI vessel model to the dimensions of R/V Gunnerus, yielded varying results. The scaled surge speed- and the scaled 1st order Nomoto- model were successful in achieving good results with almost no tuning. For the sway-yaw system, however, scaling was not done because of its inaccurate representation of the vessel dynamics. In addition, most autopilot models require only that the heading is controlled and the sway motion (from current etc.) can be compensated by adjusting the heading angle using guidance algorithms such as LOS with sideslip compensation or ILOS which are briefly introduced in Section 1.1.5.

Chapter 3

Simulations and Experiment Setup

In this chapter the procedure and setup for the simulations and experiments will be described. The procedure is divided into three parts and results from different test scenarios will be repeated for each step. The goal is to simulate all stages of the control system development. First the controllers will be derived and put through initial tests in a safe environment using MATLAB. Then, simulations in real-time using HIL will be done. Finally, the control design will be tested in a physical model. Note that HIL simulations and physical experiments will only be done for CSEI as one of the thesis' main objectives is to prove that scaling of the control system facilitates implementation on the full scale vessel as described in Section 1.2. The controllers for the full scale target vessel model of R/V Gunnerus will be scalable controllers originally developed for CSEI. A complete description of the MC Lab, HIL testing and equipment in the lab can be found in NTNU (2016).

3.1 Simulations using MATLAB/Simulink

The first tool to be used in order to develop the control- and observer-designs is the MATLAB/Simulink (version 2016b, 2015a for HIL) software developed by MathWorks. The maneuvering models presented in Setion 2.2 are implemented for both vessel models described in Section 2.1. Based on the results presented in Section 2.5 the control system will be developed and tested on this software. At this point the complete vessel models and control system exist as single initialization scripts and Simulink diagrams (for each vessel) for which simulations are done by simulating predefined test scenarios.

3.2 Hardware-in-the-Loop Simulations

After making sure that the control system works with the use of mathematical modeling of the vessels, it is time to implement the controllers on the software used to control the vessels in the laboratory. This software is developed by National Instruments (NI) and is called Veristand (version 2014, service pack A). Using a real time embedded controller called a compact RIO (cRIO) the same test scenarios as simulated in MATLAB/Simulink are repeated, for the CSEI model. The vessel model is divided into a series of different Simulink models connected through mapping of input- and output- ports. In theory the single Simulink model could be applied for HIL simulations with an easy mapping. However, by using the same setup as for the actual vessel the step from HIL to physical experiment is simplified. A monitoring station (see Figure 3.1) for starting and stopping simulations, tuning gains, plotting and logging is developed in order to control and record the tests. If the control systems performance during HIL simulation is adequate, the control system can be simulated on the physical model.

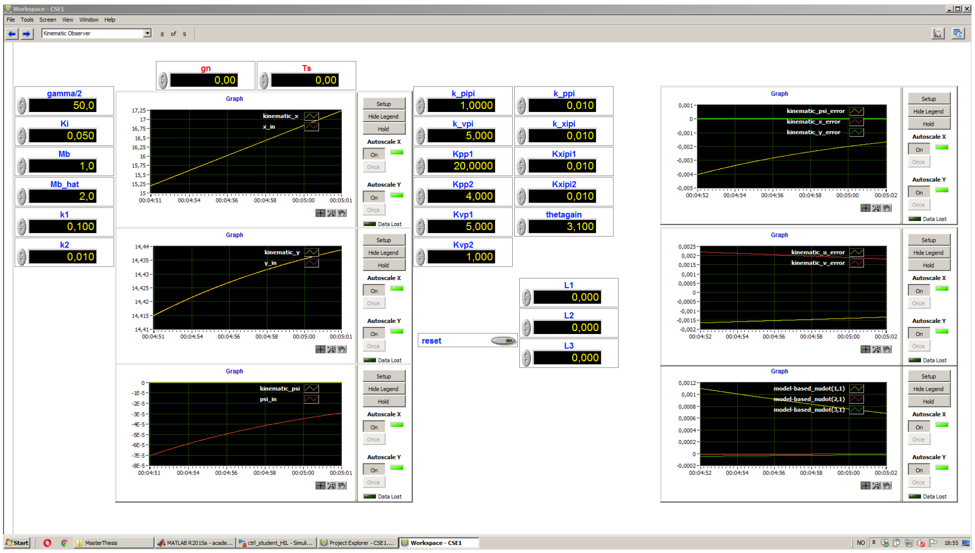
Workspace - CSE1
File
Tools
Screen
View
Window
Help
Kinematic Observer
8 of 9
Graph
kinematic_x
x_in
kinematic_y
y_in
kinematic_psi
psi_in
kinematic_psi_error
kinematic_x_error
kinematic_y_error
kinematic_u_error
kinematic_v_error
model-based_nudot(1,1)
model-based_nudot(2,1)
model-based_nudot(3,1)
17,25
15
14,44
14,41
0
-8E-5
0,001
-0,005
0,0025
-0,002
0,0012
-0,0002
00:04:51
00:04:54
00:04:56
00:04:58
00:05:00
00:05:01
00:04:52
00:05:02
Setup
Hide Legend
Hold
Autoscale X
Autoscale Y
On
Once
Data Lost
reset
Start
MasterThesis
MATLAB R2015a - acade...
ctrl_student_HIL - Simuli...
Project Explorer - CSE1....
Workspace - CSE1
NO
18:55

gn 0,00
Ts 0,00
gamma/2 50,0
Ki 0,050
Mb 1,0
Mb_hat 2,0
k1 0,100
k2 0,010
k_pipi 1,0000
k_vpi 5,000
Kpp1 20,0000
Kpp2 4,000
Kvp1 5,000
Kvp2 1,000
k_ppi 0,010
k_xipi 0,010
Kxipi1 0,010
Kxipi2 0,010
thetagain 3,100
L1 0,000
L2 0,000
L3 0,000

Figure 3.1: Screenshot of the workbench used for monitoring HIL simulations and lab experiments

3.3 Physical Experiments

To ensure that everything works as planned the control system must be tested in a physical experiment. This is the last chance for testing the control system on the software that is assumed to be used on both target vessels. Often, these experiments revile problems that did not occure during computer simulations and can be very useful.

3.3.1 The MC Lab

In order to perform physical tests of the model vessel, the MC Lab was used. It consists of a water filled basin, as shown in Figure 3.2, measuring $L \times B \times D = 40 \text{ m} \times 6.45 \text{ m} \times 1.5 \text{ m}$, advanced instrumentation for simulation above and underneath the surface, a towing carriage with on board computer, wave generator and a control room equipped with computers for controlling tests and with tools to fix the vessels.

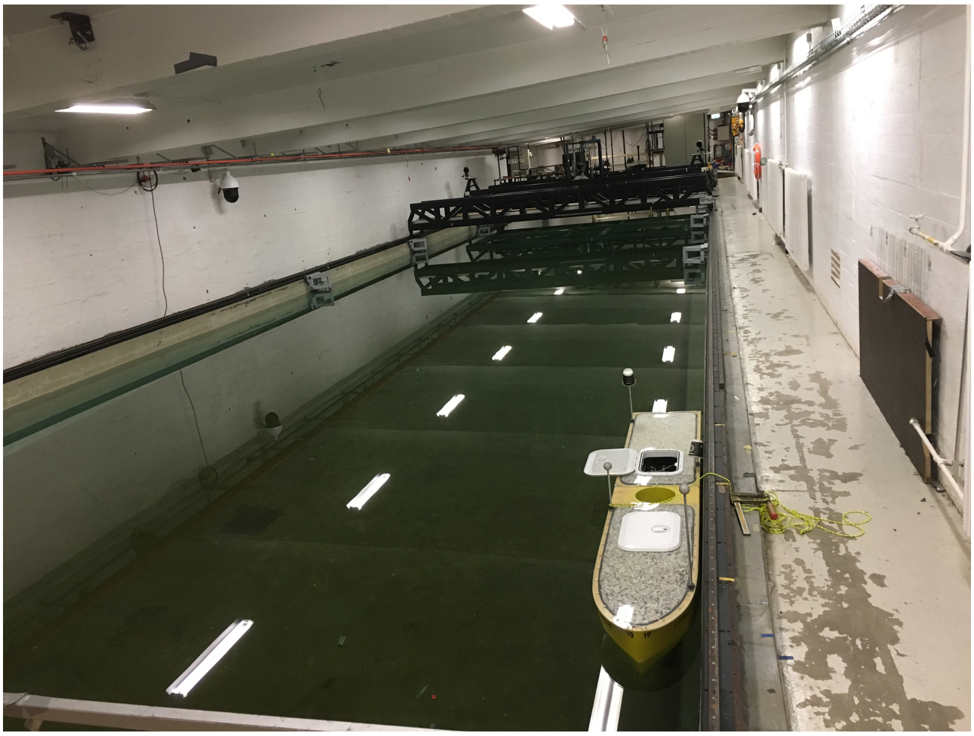

Figure 3.2: The Marine Cybernetics Laboratory

3.3.2 Experiments on the CSEI Model Vessel

Having done HIL simulations one can use the workbench (or monitoring station) developed during HIL simulations. The only difference is that the position inputs are taken from a positioning system and the controller inputs are sent through a thrust allocator to the real vessel actuators. Tuning, monitoring and logging of the results will therefore be done in the same way as for HIL tests.

As the positioning system uses high-speed infrared cameras with a certain range, the vessels cannot move far from them. The most efficient way to test an autopilot design and path following will then be to either move in a circle or similarly between way point in a triangle or square, keeping the vessel within range of the cameras. For drop out of the signals an observer is a must for not risking loosing control of the vessel. In order to simulate current the towing carriage (on which the cameras are mounted) can be driven at a constant speed in one direction, thus compensating for not having a current generator.

3.3.3 Notes on Physical Experiments with CSEI

Since the actual vessel of CSEI does not work because of a faulty bow thruster, HIL simulations are done in order to debug the control system. These simulations will replace the physical experiments of the control system with the actual model. As it uses the same software as the HIL, the verified control system can be assumed to work on the actual vessel by only minor adjustments.

Several HIL simulations were run for testing the control system. Since the same model used in MATLAB and Simulink is included in these simulations, the results will be very similar, if not equal. Therefore, more work have been done to develop and explain complex scenarios in MATLAB and Simulink rather plotting every result from HIL simulations. The results of HIL that are included in this thesis will act as proof that simulations were done using the HIL software and that the control system is ready for use in physical experiments when the model vessel is fixed.

Chapter 4

Low-Cost Observer Designs

In Section 1.1.3, the model-based observer design was presented shortly as one of three mathematical models of the vessel. However, for this thesis the model parameters will be treated as unknown or estimates making the model-based design less accurate. Therefore, the preferred observer will be a signal-based observer. Another aspect discussed in sections 1.1.1 and 1.1.6 is to keep the costs of testing and implementation at a minimum. This makes the latter observer preferable as it can be tuned using sensors in a laboratory and does not necessarily need extensive tuning during sea trials. An observer is important also for testing in the laboratory for the same reasons as on an actual vessel. The positioning system may drop out, destroying simulations completely. With an observer, at least the damage can be reduced.

One of the most well-known estimators are based on Kalman (1960) and Kalman and Bucy (1961) where the linear Kalman filters for continuous- and discrete-time were developed. Later, in Schmidt and McGee (1985) these were applied to nonlinear applications linearizing the systems about the state estimates at each time step. These are the Extended Kalman filters (EKF). These can be applied for both model-based systems as in Fossen (2011, Chapter 11.3) and for signal-based systems (Vik, 2014). These designs are more intuitive and was used to get an overview of the underlying ideas behind state estimators and how to build signal-based observer models. For nonlinear filters Khalil (2015) is recommended for description of similar estimators, mathematical examples and stability analysis.

For this thesis a kinematic approach is chosen. The observer consists of two interconnected parts. The first one, an attitude estimator was first developed by Grip et al. (2013), and is based on Grip et al. (2012) and Mahony et al. (2008). The second part of the observer is for the translational motion similar to Bryne et al. (2014), but is made time-invariant as in Bryne et al. (2015) and Brodtkorb et al. (2016). It is a 6 DOF kinematic observer design, using Inertial Measurement Units (IMU) for angular velocity-, specific force- and a compass for heading-measurements. In addition, Global Navigation Satellite System (GNSS) is used for position updates in the translation part of the observer. Stability for the chosen observer is proved using Grip et al. (2012) and Bryne et al. (2015). It also includes a Virtual reference unit (VRU) which is used to transform the position from a GNSS receiver to the coordinate frame of the IMU. General information in addition example of similar integration filters for IMU and GNSS with and without VRUs can be found in Fossen (2011, Chapter 11.5).

The observer is in this thesis mainly used as a separate part of the control system. It is used for recreating states and works according to the separation principle (Sørensen, 2013). A short simulation study will be done for the observer studying how accurate the states can be recreated and how noise affects the accuracy and stability of the kinematic observer.

4.1 Kinematic Observer

For strap down Inertial Navigation System (INS) the following NED representation can be applied (Bryne et al., 2015)

$$\dot{\boldsymbol{p}}^n = \boldsymbol{v}^n \tag{4.1a}$$

$$\dot{\boldsymbol{v}}^n = \boldsymbol{R}_b^n \boldsymbol{f}^b + \boldsymbol{g}^n \tag{4.1b}$$

For the chosen observer design quaternions are preferred and introduces a third equation similar to (2.15)

$$\dot{\boldsymbol{q}}_b^n = \boldsymbol{T}(\boldsymbol{q}_b^n)\boldsymbol{\omega_{b/n}^b}. \tag{4.2}$$

In (4.1), $\boldsymbol{p}^n = [N, E]^\top$, $\boldsymbol{v}^n = [u^n, v^n]$ is the velocities decomposed in NED frame, $\boldsymbol{q}_b^n$ is the quaternion vector, $\boldsymbol{f}^b$ is the specific force vector decomposed in BODY coordinates and $\boldsymbol{g}^n$ is the gravity vector. If Euler angles is preferred (2.11) can be applied instead of (4.2).

The instrumentation follows Brodtkorb et al. (2016). The position measurements is obtained from GNSS, heading measurements from a compass, angular velocity and specific force from an IMU. This is represented in the following equations

$$\boldsymbol{p}^n = [N, E]^\top \tag{4.3a}$$

$$\psi_c = \psi \tag{4.3b}$$

$$\boldsymbol{\omega}_{imu}^b = \boldsymbol{\omega}^b + \boldsymbol{b}_g \tag{4.3c}$$

$$\boldsymbol{f}_{imu}^b = \boldsymbol{R}(\boldsymbol{\Theta})(\dot{\boldsymbol{v}}^n - \boldsymbol{g}^n). \tag{4.3d}$$

In (4.3a), ψ_c is the compass heading, b_g is the gyroscope bias term and $\boldsymbol{R}(\boldsymbol{\Theta})$ is the linear velocity transformation matrix as represented in (2.7).

4.1.1 Attitude Observer

Estimating the attitude is done by implementing model from Grip et al. (2013), Bryne et al. (2015) and Brodtkorb et al. (2016):

$$\dot{\hat{\boldsymbol{q}}}_b^n = \boldsymbol{T}(\boldsymbol{q})(\boldsymbol{\omega}_{imu}^b - \hat{\boldsymbol{b}}_g + \hat{\boldsymbol{\sigma}}) \tag{4.4a}$$

$$\dot{\hat{\boldsymbol{b}}}_g = \text{Proj}(\hat{\boldsymbol{b}}_g, k_I \hat{\boldsymbol{\sigma}}), \tag{4.4b}$$

where

$$\hat{\boldsymbol{\sigma}} = k_1 c^b \times \boldsymbol{R}^\top(\hat{\boldsymbol{q}}_b^n) c^n + k_2 \boldsymbol{f}_{imu}^b \times \boldsymbol{R}^\top(\hat{\boldsymbol{q}}_b^n) \hat{\boldsymbol{f}}^n \in \mathbb{R}^3 \tag{4.5}$$

is a correction term, $\{\hat{\boldsymbol{q}}_b^n \in \mathbb{R}^4\}$, is the quaternion estimate, $\{\hat{\boldsymbol{b}}_g \in \mathbb{R}^3\}$ estimated gyro bias and $\{\hat{\boldsymbol{f}}^n \in \mathbb{R}^3\}$ is the specific force estimate vector decomposed in NED. $\{\boldsymbol{R(q_b^n)} \in \mathbb{R}^{3\times3}\}$ is the linear velocity transformation matrix (2.7) in terms of quaternions. $\boldsymbol{c}^n = [1, 0, 0]^\top$ and $\boldsymbol{c}^b = [\cos(\psi), -\sin(\psi), 0]$ are reference vectors. $k_1 > k_p$, $k_2 > k_p$, $k_p > 0$ and $k_I > 0$ are scalar gains.

4.1.2 Translational Observer

In Bryne et al. (2015) the translational observer equations are presented as:

$$\dot{\hat{p}}_I^n = \hat{p}_z^n + k_{pipi} \tilde{p}_I \tag{4.6a}$$

$$\dot{\hat{\boldsymbol{p}}}^n = \hat{\boldsymbol{v}}^n + \theta \begin{bmatrix} \boldsymbol{0_{2\times1}} & \boldsymbol{K_{pp}} \\ k_{ppi} & \boldsymbol{0_{1\times2}} \end{bmatrix} \begin{bmatrix} \tilde{p}_I \\ \tilde{\boldsymbol{p}} \end{bmatrix} \tag{4.6b}$$

$$\dot{\hat{\boldsymbol{v}}}^n = \hat{\boldsymbol{f}}^n + \boldsymbol{g}^n + \theta^3 \begin{bmatrix} \boldsymbol{0_{2\times1}} & \boldsymbol{K_{vp}} \\ k_{vpi} & \boldsymbol{0_{1\times2}} \end{bmatrix} \begin{bmatrix} \tilde{p}_I \\ \tilde{\boldsymbol{p}} \end{bmatrix} \tag{4.6c}$$

$$\dot{\boldsymbol{\xi}}_f = -\boldsymbol{R}(\boldsymbol{q}_b^n) \boldsymbol{S}(\hat{\boldsymbol{\sigma}}) \boldsymbol{f}_{imu}^b + \theta^4 \begin{bmatrix} \boldsymbol{0_{2\times1}} & \boldsymbol{K_{\xi p}} \\ k_{\xi pi} & \boldsymbol{0_{1\times2}} \end{bmatrix} \begin{bmatrix} \tilde{p}_I \\ \tilde{\boldsymbol{p}} \end{bmatrix} \tag{4.6d}$$

$$\hat{\boldsymbol{f}}^n = \boldsymbol{R}(\hat{\boldsymbol{q}}_b^n) \boldsymbol{f}_{imu}^b + \boldsymbol{\xi}_f. \tag{4.6e}$$

$\{\hat{p}_I^n \in \mathbb{R}\}$ is the scalar integral value estimate of the position, $\{\hat{p}_z \in \mathbb{R}\}$ is the estimated virtual reference (Bryne et al., 2014), $\{\hat{\boldsymbol{p}}^n, \hat{\boldsymbol{v}}^n \in \mathbb{R}^2\}$ are the position and velocity estimates and $\{\hat{\boldsymbol{\xi}}_{\boldsymbol{f}} \in \mathbb{R}^2\}$ is a correction vector for acceleration. k_{pipi}, k_{ppi}, k_{vpi} and $k_{\xi pi}$ are scalar gains all greater than zero, $\theta \geq 1$ is a high-gain. $\boldsymbol{K_{pp}}, \boldsymbol{K_{vp}}, \boldsymbol{K_{\xi p}} \in \mathbb{R}^{2\times2}$ are gain matrices. $\tilde{p}_I = p_I - \hat{p}_I = 0 - \hat{p}_I \in \mathbb{R}$ an $\tilde{\boldsymbol{p}} = \boldsymbol{p}^n - \hat{\boldsymbol{p}}^n \in \mathbb{R}^2$ are called the driving errors. $\{\hat{\boldsymbol{f}}^n \in \mathbb{R}^3\}$ and

$\{\boldsymbol{R}(\boldsymbol{q}_b^n) \in \mathbb{R}^{3\times3}\}$ are the same as in Section (4.1.2), $\{\boldsymbol{S}(\hat{\boldsymbol{\sigma}}) \in \mathbb{R}^{3\times3}\}$ is the skew symmetric matrix (2.6) in terms of the correction term (4.5). Finally, the specific force estimates from the IMU is denoted as $\{\hat{\boldsymbol{f}}_{imu}^b \in \mathbb{R}^3\}$ and the gravity vector as $\{\boldsymbol{g}^n \in \mathbb{R}^3\}$.

4.2 Stability Analysis

Stability analysis is of great importance in both linear and nonlinear control theory. For nonlinear observers Khalil (2015) analyses a variety of examples including the EKF. The main goal is to be able to guarantee that the region of attraction is as big as possible with one or more stable equilibrium and reducing any unstable regions to a minimum.

In (4.4b), $\text{Proj}(\cdot)$ refers to the projection operator which is a well known and widely used robustification tool in nonlinear control- and observer-theory. It is most often applied to adaptive systems in order to guarantee boundedness of solutions, but can be applied to other observer designs as well (Krstič, 1995). The projection function applied for this observer design is described in Grip et al. (2012, Appendix)

The complete observer of (4.4) and (4.6) is proven to have uniformly semi-global exponentially stable (USGES) equilibrium by Grip et al. (2013). Later, its region of attraction is also proven to be almost globally uniformly attractive (Bryne et al., 2014). To compare the stability of this observer, one of the best known observer designs for nonlinear systems, the EKF, is also proven USGES. This, because it is a linearized observer preventing it from being uniformly globally exponentially stable (UGES). The region of attraction in the kinematic observer is however bigger as the EKF dynamics are not accurate further away from the value which the filter was linearized around.

4.3 Simulations of the Kinematic Observer

In order to test the observer design, the position vector in addition to angular velocity and acceleration in yaw is fed from the vessel model to the observer. Based on these values it is supposed to estimate the velocities and attitude of the vessel. A simple test scenario will be designed and simulated in order to verify that it works. Further, this test will be used to investigate what happens when noise is added to the velocity and acceleration estimates. Simulations will be done according to the procedure in Chapter 3. Due to the complexity of the observer and to make the plots big enough to show the results only the ones relevant for the discussion of the observers performance will be presented.

As the observer depends only on position and gyro measurements there is no need for scaling it to be suited for the larger R/V Gunnerus model. If the sensors are similar and as reliable as for the model vessel there should be no difference in the accuracy.

4.4 MATLAB/Simulink Simulations

The 3 DOF vessel model of CSEI (with values as described in Section 2.4) is set in motion using a combination of thrust in surge and yaw as described by Figure 4.1 for a period of 500 seconds. It is also assumed that the virtual reference $\hat{p}_z$ is zero for simplified simulations.

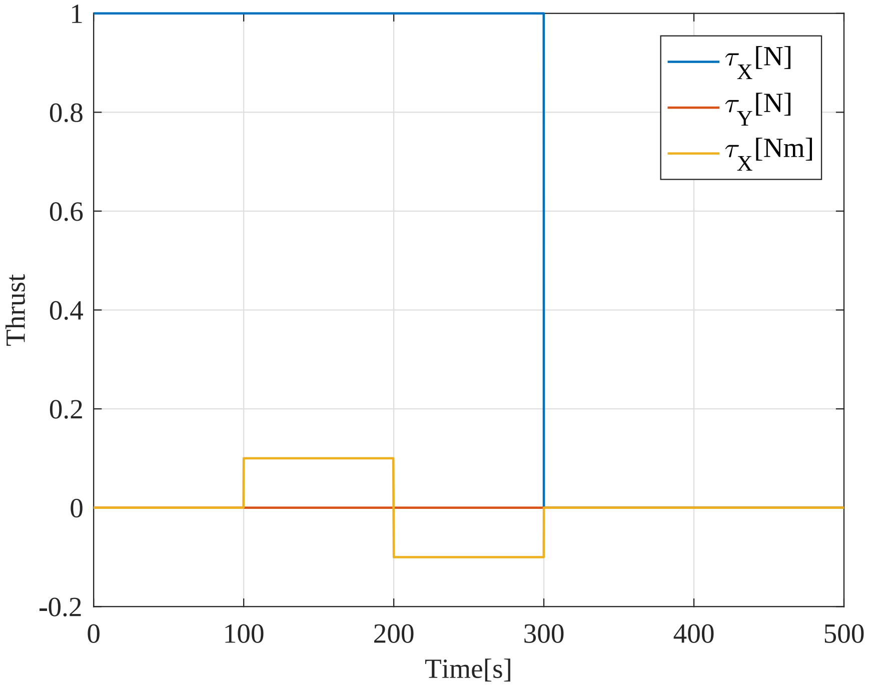

Figure 4.1: Thrust input for the observer study

4.4.1 Estimation using Noiseless Signals

For the translational part of the observer, the position and velocity estimates from (4.6) along with the true values from the vessel model are shown in Figure 4.2. This figure shows that the estimates are close to the real values. It is important to note that the estimated velocities (4.6c) are transformed into BODY frame before plotting the results. This is done for comparing them with the corresponding true velocity components from the model which are in BODY frame. The corresponding errors are shown in Figure 4.3 and shows that the translational observer is successful in estimating the correct values and making the error converge to zero.

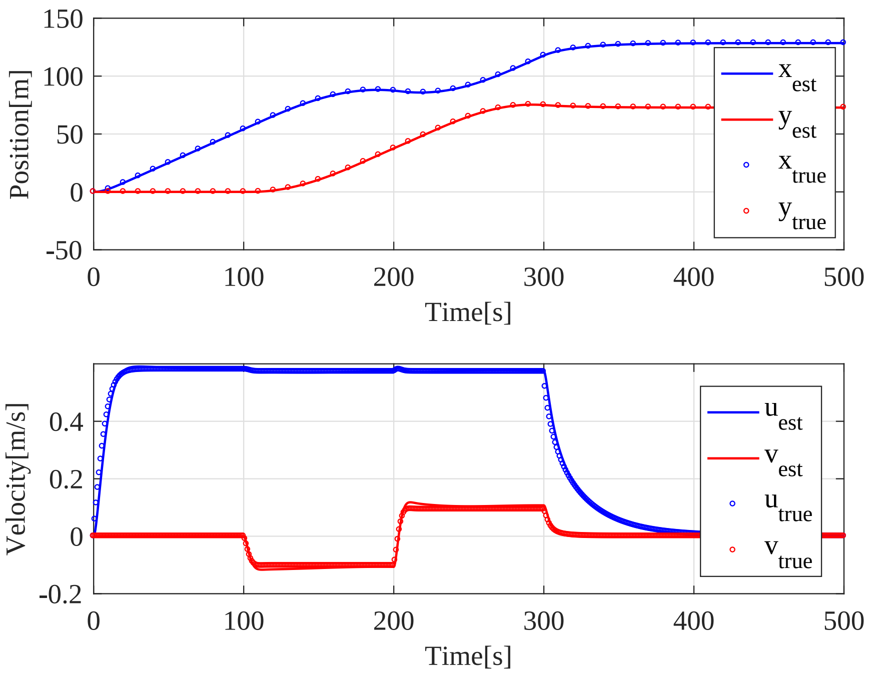

Figure 4.2: Position and velocity estimates without noise

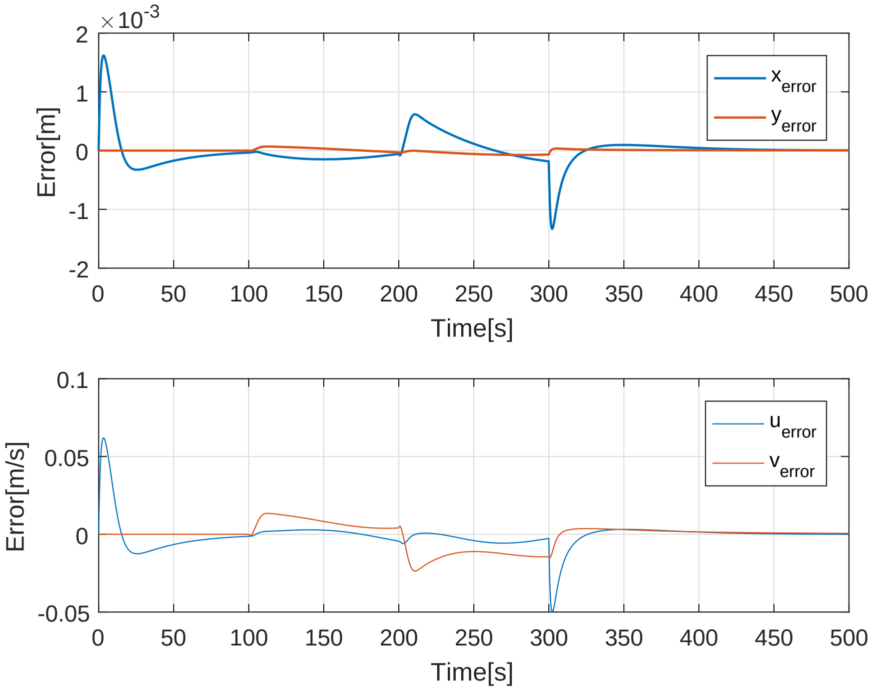

Figure 4.3: Position and velocity errors without noise

The attitude part of the observer is used to calculate the rate of orientation and the attitude of the vessel according to (4.4). Since this is a 6 DOF observer it can also estimate the motion in roll (ϕ, p) and pitch (θ, q), but since input is only fed from a 3 DOF model (angular motion only from yaw (ψ, r) measurements), their accuracy will not be perfect. The estimated velocities can are shown in Figure 4.4. It shows that the yaw rate is by far the most dominant term and that the motion in the other 2 rotational DOF are negligible, as expected. Only at about 200- and 300- seconds they become relevant when the vessel does a sharp turn as can be seen in Figure 4.1. Comparing the results in Figure 4.1 with the actual yaw rate for the 3 DOF vessel model results in the following plot shown in Figure 4.5. From the plot it is obvious that the estimated rate are slower and less peaked than the actual value. Since the estimated values need some time to be calculated, the actual yaw rate stabilizes which means that the estimated states do the same. Therefore, the peaks are at the same points, but with lower values for the estimates. The difference, however, is small and the tendency of the plots are similar.

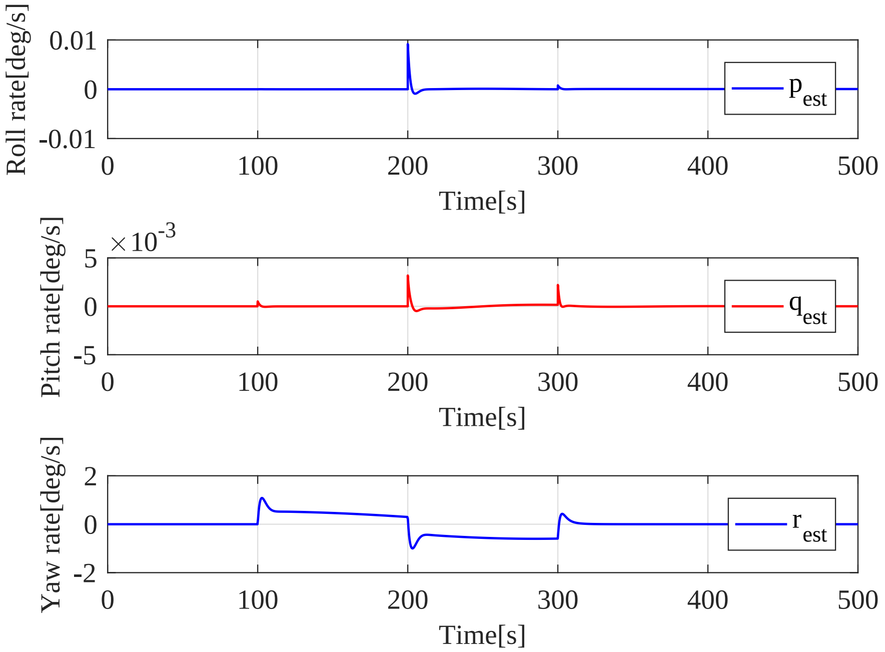

Figure 4.4: Estimated angular rates without noise

For the roll and pitch angles there is no comparable data as the states are assumed to be negligible in the 3 DOF vessel model. Figure 4.4 can at least strengthen this assumptions by showing that the values are way lower than for the yaw. A good sign is that the yaw rates converges to zero over time, meaning that the estimates are stable and together with the error plot in 4.5 concludes that the angular velocity estimates are accurate. In order to find the attitude of the vessel the rates are integrated, resulting in Figure 4.6. Comparing the estimated yaw angle with the true values shows that the error is small confirming that the attitude observer in fact works as expected. The latter is seen from figure 4.7.

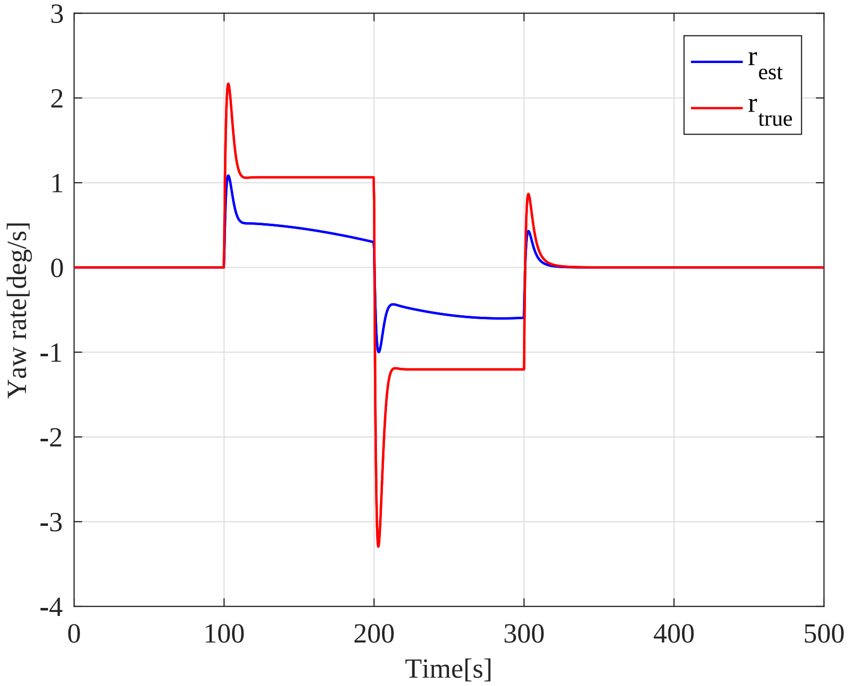

Figure 4.5: Yaw rate error without noise

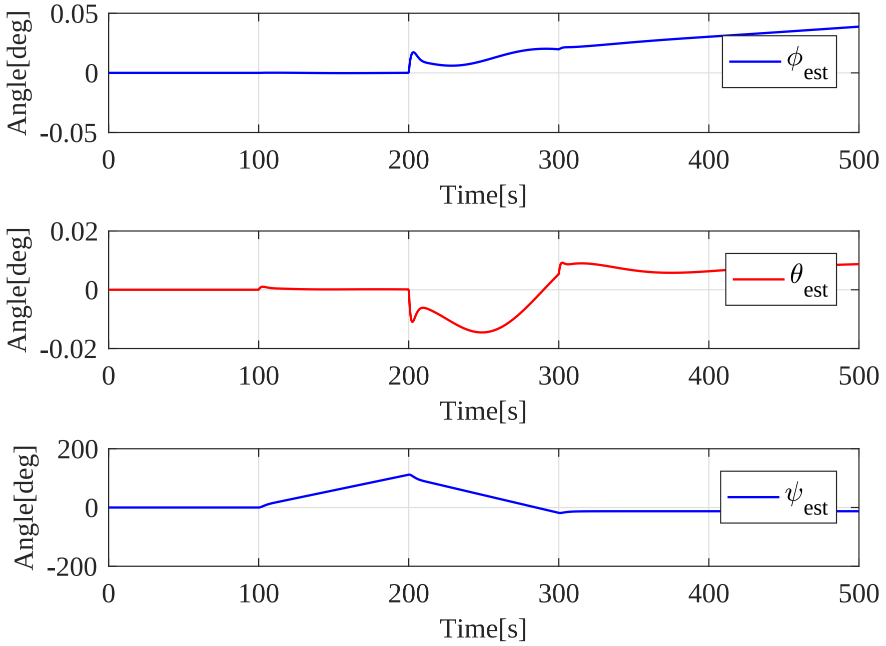

Figure 4.6: Attitude without noise

4.4.2 Estimation using Noisy Signals

In this section noise will be added to the gyro- and to the accelerometer- measurements from the IMU in order to see how the observer performs with disturbances. The noise is assumed to

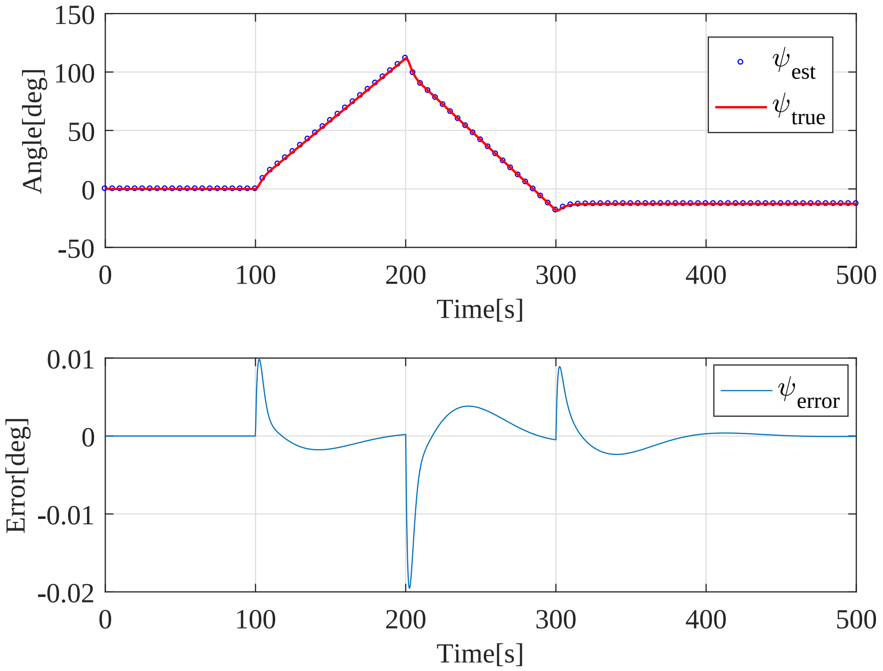

Figure 4.7: True and estimated yaw angle with the error for noiseless test

have zero mean value (white noise) and the noise power used in the simulations were chosen as 10^{-7}. If the observer works as it should the noisy inputs will be filtered through integration and the offset minimized by the estimator. In order to be successful, the observer should perform almost as well as without noise and at least make the errors converge to zero. The same simulation as before were done, with thrust inputs according to Figure 4.1. The results from the simulations are presented in the following figures 4.8, 4.9, 4.10 and 4.11.

Starting with the translational observer and Figure 4.8 the noise does not seem to affect the performance at all, but by looking at the corresponding errors in Figure 4.9 it is obvious that the noise increases the error. The velocity estimates are now noisy, but with much smaller peaks than the noise that was added to the specific force measurements. The same can be seen for the position errors, with only extremely small oscillations resulting from noise. The observer is still stable and the errors converge to zero, with estimates that have reduced noise compared to the measurements.

The results from the attitude part of the observer shows similar results. Figure 4.10 shows how the estimates now relates to the true values showing how the noise on the angular velocity in yaw affects the attitude estimates. Appart from the noise added to the signals the estimated yaw angle seems to be similar to the results achieved without noise (see Figure 4.6). In Figure 4.11, the errors from the estimates are shown. It is worth noticing that the error in heading is greater

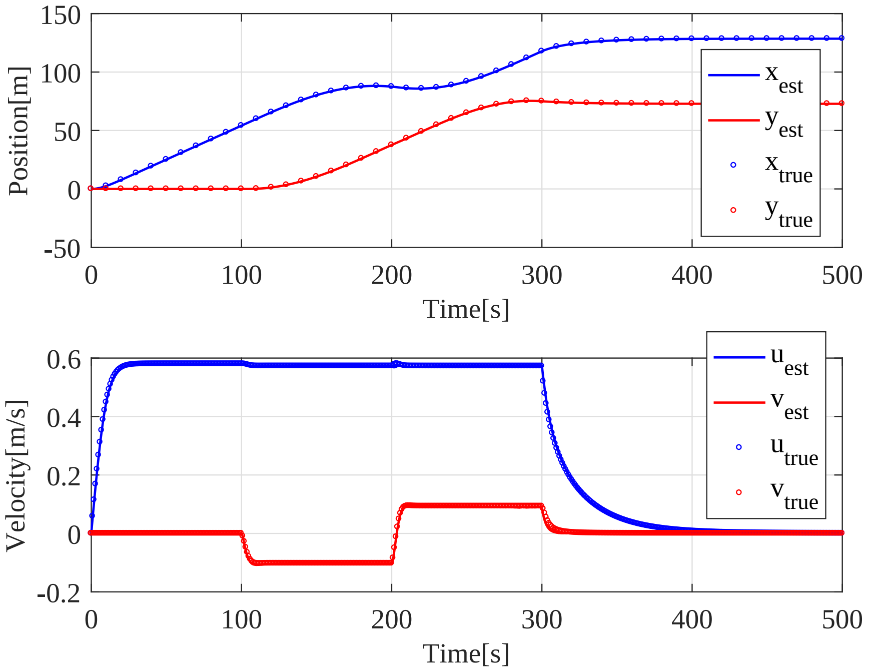

Figure 4.8: Estimated postion and velocity from simulations with noise

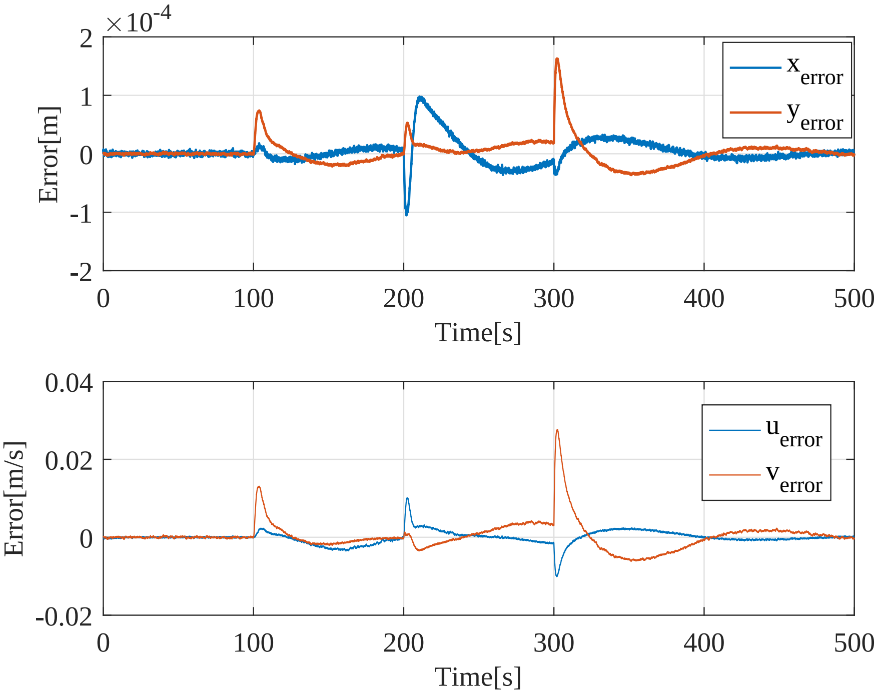

Figure 4.9: Error in postion and velocity estimates from simulations with noise

than without noise, but also that the estimated signals have smaller peaked noise than the yaw rate.

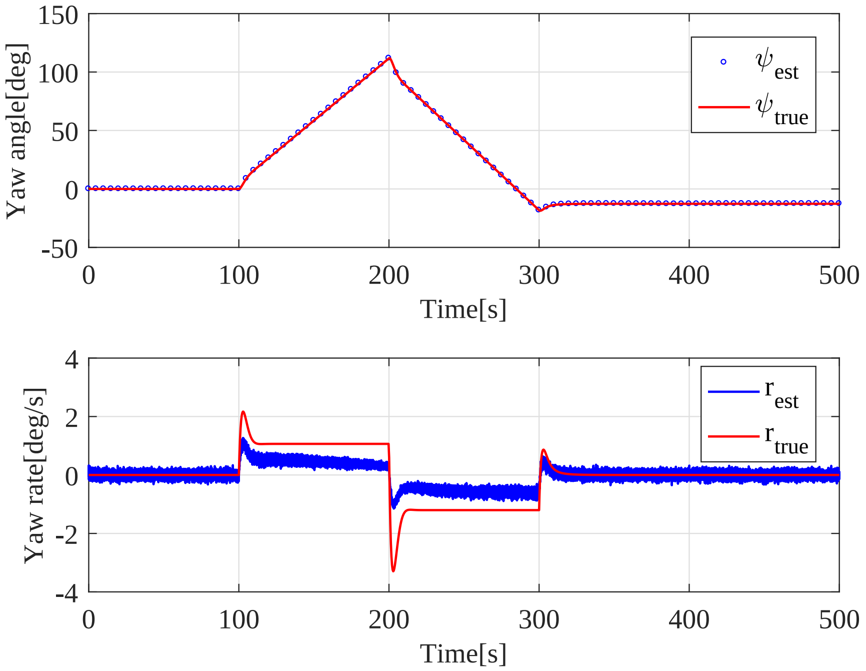

Figure 4.10: Estimated heading and yaw rate from simulations with noise

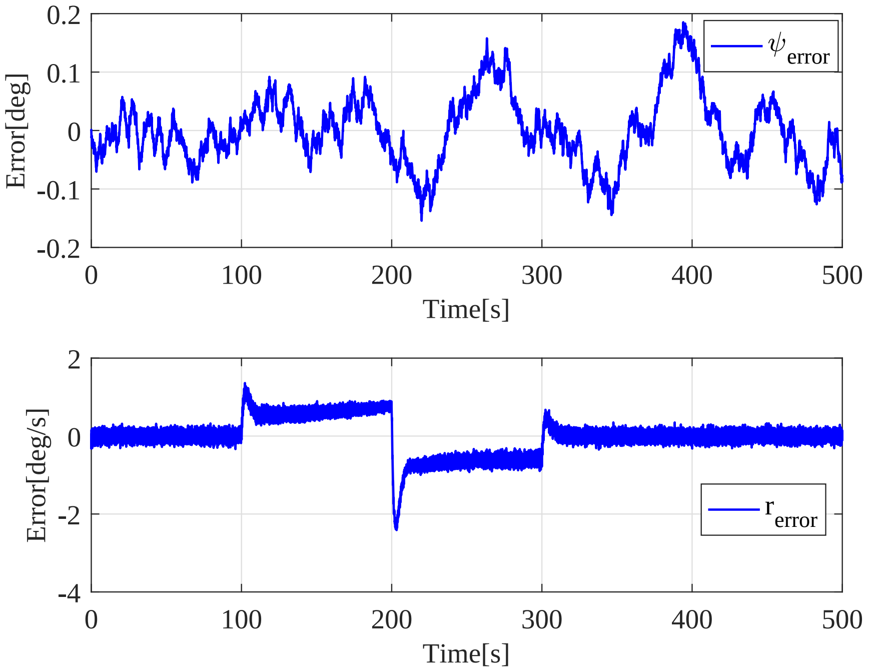

Figure 4.11: Errors in heading and yaw rate from simulations with noise

4.4.3 HIL Simulation of Observer

Figure 4.12 shows how the position and heading of CSEI varies over time in one of the HIL simulations. This simulation is done without any noise on the measured signals. The estimated signals are accurate representations of the true values and the errors cannot be seen from this plot. Here steps in input forces in surge and yaw were added in order to induce vessel motions. Using Figure 4.13 the corresponding errors are shown and confirm that the observers work well, just as in the simulations shown in the previous sections.

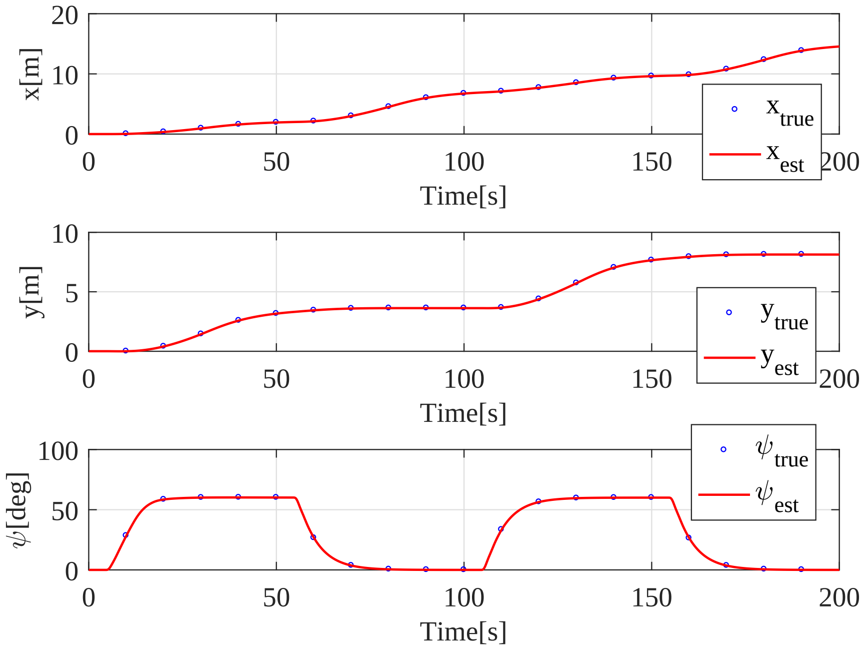

Figure 4.12: Estimated position and heading from HIL simulation

The plots shown in Figures 4.12 and 4.13 shows that the observer worked well in HIL simulations and is ready for application on the physical model vessel of CSEI, when the vessel is fixed.

4.5 Conclusions

In this chapter a kinematic observer has been developed and simulated. The observer is built as an integrator filter which removes oscillating noise by integration. This makes the signal smoother and easier to use in controllers. Simulations were done with and without white noise on the specific force inputs to investigate whether the observer worked as expected. When no noise was added the results proved very accurate with smooth estimates and errors that rapidly converged to zero. Since the observer is a 6 DOF vessel angular motion in roll and pitch could be estimated through the inputs in x, y- and ψ. These were estimated to be at their largest when the vessel changed heading which was as expected.

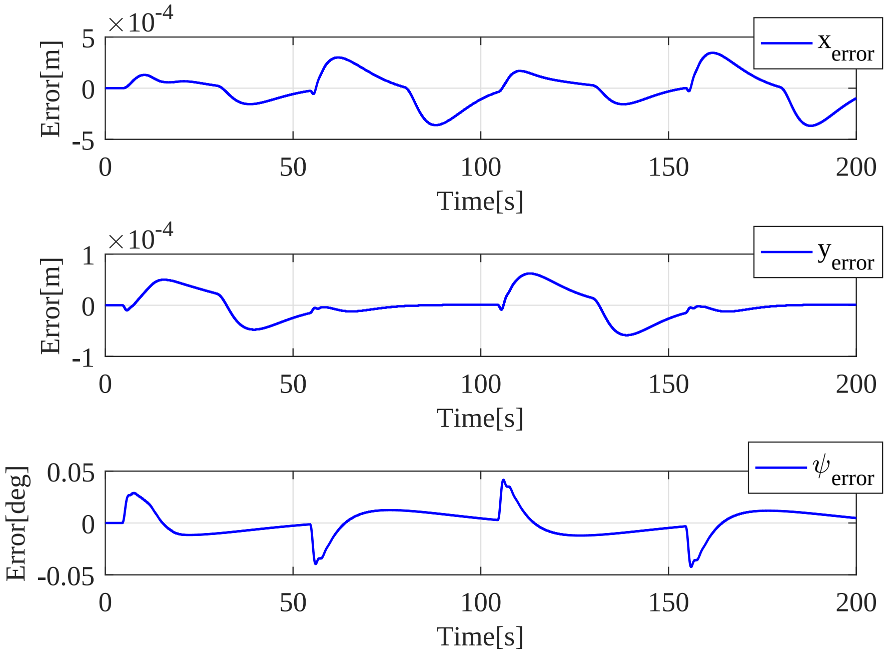

Figure 4.13: Errors in position and heading estimates from HIL simulation

Adding noise to the specific force measurements did not change the results too much. The observer removed the largest amplitudes of the noise out through integration and was able to adjust for the bias caused by integration of the disturbances. The estimates did also look significally smoother than the noisy measurements.

From HIL simulations the same results were obtained as the observer managed to estimate the motion with the same accuracy as the other simulations as the model and all controllers used in HIL were the same. The simulation study proved that this observer work well, that it is ready for use on the MC Lab and for being used on a physical model of R/V Gunnerus.

Chapter 5

Model Reference Adaptive Control

As presented in Section 1.1.4, MRAC is one of the most known approaches in adaptive control (Ioannou and Sun, 2012). As this approach has been widely used in various applications there are several variants of applying the MRAC algorithms. In short, the common goal of all MRAC models is to make the output of the plant track a generated reference signal. The signal is made by a known reference plant model. This is called the model reference control problem (Lavretsky and Wise, 2012). During this process the objective is to keep the error between plant and reference at a minimum, while estimating and adapting to unknown parameters. The closed loop plant consists of an ordinary feedback control law consisting of the plant, a controller and the tuning mechanism for the parameter estimates.

MRAC schemes can be further divided into direct or indirect and as regular control models they can be normalized (Sørensen, 2015). Direct MRAC refers to the adaptive law updating the parameter vector directly. The indirect method updates the same vector only when an algebraic equation which relates the vector to on-line plant parameter estimates is solved (Ioannou and Sun, 2012). In this thesis two direct- and one indirect MRAC- model will be investigated. The first direct adaptive controller is based on vectorial MRAC with integral action. The second will be designed with a baseline control law and for the indirect adaptive controller a scalar system will be implemented. One requirement for both methods of MRAC is extensive knowledge of the plant and the requirements needed for good performance. In Figure 5.1 the different MRAC designs are shown. These figures are based on Ioannou and Sun (2012)

The controllers, or more precisely, the reference plants will be based on the normalized maneuvering models developed in Section 2.5. These normalized control laws are used to facilitate scaling. For the heading controllers, Skjetne (2016) and Lavretsky and Wise (2012) are used as the main references. For the surge controller Ioannou and Sun (2012) and Fossen (2011) are studied in order to develop a similar normalized control design.

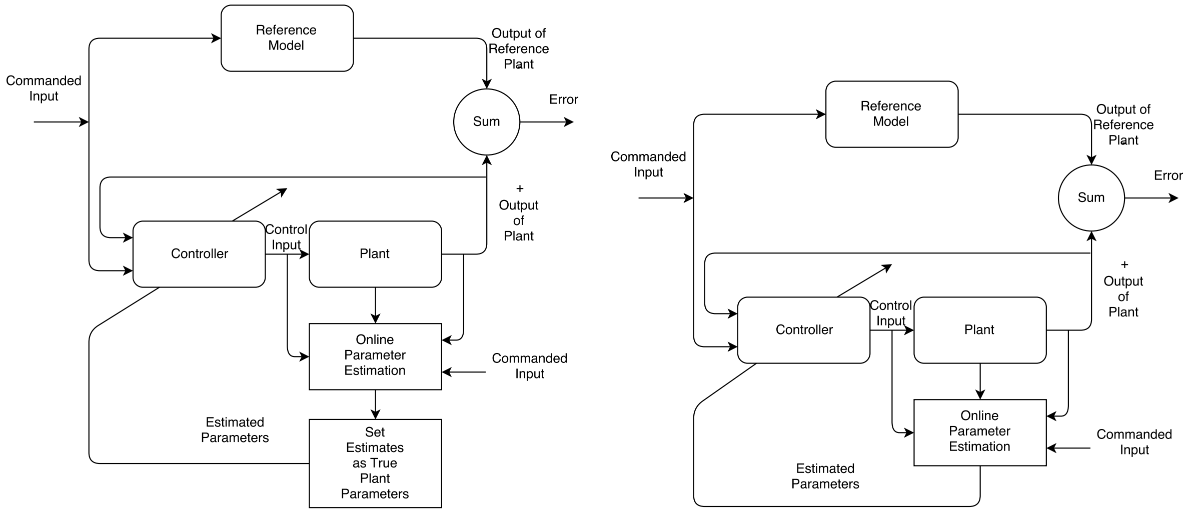
Reference Model
Output of Reference Plant
Commanded Input
Sum
Error
+
Output of Plant
Controller
Control Input
Plant
Online Parameter Estimation
Commanded Input
Estimated Parameters
Set Estimates as True Plant Parameters
Reference Model
Output of Reference Plant
Commanded Input
Sum
Error
+
Output of Plant
Controller
Control Input
Plant
Online Parameter Estimation
Commanded Input
Estimated Parameters

(a) Indirect MRAC scheme **(b)** Direct MRAC scheme

Figure 5.1: Two different designs of MRAC

In order to achieve robustness of the adaptive controllers, two modifications are included in the control design (Ioannou and Sun, 2012). These are the dead-zone modification and the projection operator. Dead-zone modification prevents the controller from over-estimating parameters when the error between plant and reference is low. On the other hand, the projection guarantees an upper bound (same as for the observer in Section 4.2) for the estimates, reducing parameter drifting. Robustification techniques are also used as basis for developing certification of adaptive controllers as done for the projection function in Campbell et al. (2010).

In the following sections the MRAC methods will be further explained using the normalized controllers as examples. The derivations of each controller will be explained methodically and a simulation study will be done in order to test the different controllers and robustification techniques. Simulations will be done separately for each controller and for the two combinations of surge and yaw controllers together. In addition, relevant issues from the ADPRC'16 cruise (Section 1.1.8) will be discussed in light of the simulation results.

5.1 Heading Controllers

5.1.1 Direct MRAC Design with Integral Action

The heading controllers are built using the normalized first order Nomoto model, developed in Section 2.3. According to Lavretsky and Wise (2012) the standard state space representation for a general MRAC design including integral action is:

$$\dot{\boldsymbol{x}}_{ia} = \boldsymbol{A}_{ia}\boldsymbol{x}_{ia} + \boldsymbol{B}_{ia}\boldsymbol{\Lambda}(\delta + \boldsymbol{\Theta}^\top \boldsymbol{\Phi}(\boldsymbol{x}_0, t)) + \boldsymbol{B}_{ref}\boldsymbol{y}_{cmd} \tag{5.1a}$$

$$\boldsymbol{y}_{ia} = \boldsymbol{C}_{ia}\boldsymbol{x}_{ia}. \tag{5.1b}$$

$\boldsymbol{x}_{ia} = [\xi, \boldsymbol{x_0}]^\top$ is the extended state vector, $\boldsymbol{x_0}$ the original state and ξ is the integral state calculated as

$$\dot{\xi} = y - y_{cmd}. \tag{5.2}$$

$\boldsymbol{A}_{ia}$, $\boldsymbol{B}_{ia}$ are the system- and input matrices, respectively. Λ is a unknown diagonal matrix with strictly positive elements, making the pair $(\boldsymbol{A}_{ia}, \boldsymbol{B}_{ia}\boldsymbol{\Lambda})$ controllable. δ is the controller input, $\boldsymbol{\Theta}$ is a vector of unknown parameters, $\boldsymbol{\Phi}(\boldsymbol{x}_0, t)$ is a known regressor vector, $\boldsymbol{B}_{ref}$ is the reference input matrix and $\boldsymbol{y}_{cmd}$ is the input from the reference model. In (5.1b) $\boldsymbol{y}_{ia}$ is the regulated output, $\boldsymbol{C}_{ia}$ the output matrix.

Plant Model

The maneuvering model used for heading control will be the normalized first order Nomoto model (2.52) using nonlinear extensions from Bech (1969). This is the same model developed through sections 2.2 and 2.3 as well as tested in simulations in Section 2.5. Skjetne (2016) shows that it can be expressed in scalar form and with integral action as

$$\begin{aligned}
\dot{\xi} &= \psi - \psi_{cmd} \\
\dot{\psi} &= r \\
\dot{r} &= -\sqrt{\frac{g}{L}}\frac{1}{T_0''}r + \frac{gK_0''}{LT_0''}\frac{T_0''K''}{K_0''T''}\left[\delta + b_0 + \sqrt{\frac{L}{g}}\frac{1}{K''}\left(\frac{T''}{T_0''} - b_1\right)r - \sqrt{\frac{L}{g}}\frac{b_3}{K''}r^3\right].
\end{aligned} \tag{5.3}$$

In this form it is possible to write (5.3) in matrix form as (5.1a) using

$$\boldsymbol{A}_{ia} = \begin{bmatrix} 0 & 1 & 0 \\ 0 & 0 & 1 \\ 0 & 0 & -\sqrt{\frac{g}{L}}\frac{1}{T_0''} \end{bmatrix}, \boldsymbol{b}_{ia} = \begin{bmatrix} 0 \\ 0 \\ \frac{gK_0''}{LT_0''} \end{bmatrix}, \boldsymbol{c} = [0, 1, 0], \quad \Lambda = \frac{T_0''K''}{K_0''T''}, \tag{5.4a}$$

$$\boldsymbol{\theta} = \begin{bmatrix} \theta_1 \\ \theta_2 \\ \theta_3 \end{bmatrix} = \begin{bmatrix} n_o \\ \frac{1}{K''}\left(\frac{T''}{T_0''} - n_1\right) \\ \frac{n_3}{K''} \end{bmatrix} \quad \text{and} \quad \boldsymbol{\Phi} = \begin{bmatrix} 1 \\ \sqrt{\frac{L}{g}}r \\ \sqrt{\frac{L}{g}}r^3 \end{bmatrix}, \tag{5.4b}$$

resulting in

$$\dot{\boldsymbol{x}}_{ia} = \boldsymbol{A}_{ia}\boldsymbol{x}_{ia} + \boldsymbol{b}_{ia}\boldsymbol{\Lambda}(\delta + \boldsymbol{\Theta}^{\top}\boldsymbol{\Phi}(\boldsymbol{x}_0, t)) + \boldsymbol{b}_{ref}y_{cmd} \tag{5.5a}$$

$$\boldsymbol{y}_{ia} = \boldsymbol{c}_{ia}\boldsymbol{x}_{ia}. \tag{5.5b}$$

Note that some uppercase letters from the general state space representation are changed into lower case. This is done in order to show that these are vectors and not matrices in this specific case.

Reference Model

The reference model can be written a similar way as (5.3)

$$\begin{aligned}
\dot{\xi}_{ref} &= \psi_{ref} - \psi_{cmd}(t) \\
\dot{\psi}_{ref} &= r_{ref} \\
\dot{r}_{ref} &= -\sqrt{\frac{g}{L}}\frac{1}{T_0''}r_{ref} + \frac{gK_0''}{LT_0''}\left[\sqrt{\frac{g}{L}}K_i''\xi_{ref} + K_p''\psi_{ref} + \frac{L}{g}K_d''r_{ref}\right].
\end{aligned} \tag{5.6}$$

By writing the reference system matrix according to

$$\boldsymbol{A}_{ref} = \sqrt{\frac{g}{L}}\boldsymbol{H}^{-1}\boldsymbol{A}_{ref}''\boldsymbol{H} \tag{5.7}$$

and the normalization matrix as

$$\boldsymbol{H} = \begin{bmatrix} \sqrt{\frac{g}{L}} & 0 & 0 \\ 0 & 1 & 0 \\ 0 & 0 & \sqrt{\frac{L}{g}} \end{bmatrix}, \tag{5.8}$$

state space representation of the reference system can be written as

$$\dot{\boldsymbol{x}}_{ref} = \boldsymbol{A}_{ref}''\boldsymbol{H}^{-1}\boldsymbol{x}_{ref} + \boldsymbol{b}_{ref}y_{cmd} \tag{5.9a}$$

$$\boldsymbol{y}_{ref} = \boldsymbol{c}\boldsymbol{x}_{ref}. \tag{5.9b}$$

In (5.6), $y_{cmd} = \psi_{cmd}$ is the commanded input and the expression in brackets can be written in matrix form as

$$\left[\sqrt{\frac{g}{L}}K_i''\xi_{ref} + K_p''\psi_{ref} + \sqrt{\frac{L}{g}}K_d''r_{ref}\right] = \boldsymbol{H}\boldsymbol{K}_{pid}^{T''} = \boldsymbol{K}_{PID}^{\top}, \tag{5.10}$$

where $K_{PID}^{\top} = [K_i, K_p, K_d]$ is a vector of proportional-intergral-derivative (PID) controller gains that are tuned in order to make the reference behave as desired. It is assumed that the unknown gain $\boldsymbol{K}_x^\top$ is assumed to be $\in \mathbb{R}^3$ with $\boldsymbol{K}_{PID}^\top$ as initial value. The reference system matrix is then assumed to be written in terms of the plant system as

$$\boldsymbol{A}_{ref} = (\boldsymbol{A}_{ia} - \boldsymbol{b}_{ia}\boldsymbol{\Lambda}\boldsymbol{K}_x^\top), \tag{5.11}$$

$$\tag{5.12}$$

which means that the nondimensional Lyapunov equation of (5.13)

$$\boldsymbol{P}^{"}_{ref}\boldsymbol{A}^{"}_{ref} + \boldsymbol{A}^{"}_{ref}\boldsymbol{P}^{"}_{ref} = -\boldsymbol{Q}^{"}_{ref}, \tag{5.13}$$

$$\tag{5.14}$$

can be solved for $\boldsymbol{P}^{"}_{ref} = \boldsymbol{P}^{"T}_{ref} > 0$ given $\boldsymbol{Q}^{"}_{ref} = \boldsymbol{Q}^{"T}_{ref} > 0$.

Control- and Update- Laws

In order to simplify the derivation of the control laws the nondimensional matrices are scaled back according to

$$\boldsymbol{A}_{ref} = \sqrt{\frac{g}{L}}\boldsymbol{H}^{-1}\boldsymbol{A}^{"}_{ref}\boldsymbol{H} \tag{5.15a}$$

$$\boldsymbol{P}_{ref} = \boldsymbol{H}\boldsymbol{P}^{"}_{ref}\boldsymbol{H}. \tag{5.15b}$$

Using (5.5) where $\boldsymbol{A}_{ia}$ is Hurwitz, (5.11) and that the DC gain from $y_{cmd} \rightarrow y_{ref}$ the following control law is proposed (Skjetne, 2016)

$$\delta = -\hat{\boldsymbol{K}}_x^\top \boldsymbol{x} - \hat{\boldsymbol{\Theta}}^\top \boldsymbol{\Phi}(\boldsymbol{x}_0, t). \tag{5.16}$$

where $\hat{\boldsymbol{K}}_x^\top$ and $\hat{\boldsymbol{\Theta}}^\top$ are the unknown gains to be estimated in the controller. By applying (5.16) into (5.5) and defining the parameter errors as

$$\tilde{\boldsymbol{K}}_x = \hat{\boldsymbol{K}}_x - \boldsymbol{K}_x \tag{5.17a}$$

$$\tilde{\boldsymbol{\Theta}} = \hat{\boldsymbol{\Theta}} - \boldsymbol{\Theta}, \tag{5.17b}$$

the (5.5a) can be written as

$$\dot{\boldsymbol{x}}_{ia} = \boldsymbol{A}_{ref}\boldsymbol{x}_{ia} + \boldsymbol{b}_{ref}y_{cmd} + \boldsymbol{b}_{ia}\boldsymbol{\Lambda}\tilde{\boldsymbol{K}}_x^\top \boldsymbol{x}_{ia} + \boldsymbol{b}_{ia}\boldsymbol{\Lambda}\tilde{\boldsymbol{\Theta}}^\top \boldsymbol{\Phi}(\boldsymbol{x}_0, t). \tag{5.18}$$

To derive the control laws, the error dynamics ($\boldsymbol{e}_{ia} = \boldsymbol{x}_{ia} - \boldsymbol{x}_{ref}$) must be investigated further

$$\dot{\boldsymbol{e}}_{ia} = \boldsymbol{A}_{ref}\boldsymbol{e}_{ia} + \boldsymbol{b}_{ia}\boldsymbol{\Lambda}\tilde{\boldsymbol{K}}_x^\top \boldsymbol{x}_{ia} + \boldsymbol{b}_{ia}\boldsymbol{\Lambda}\tilde{\boldsymbol{\Theta}}^\top \boldsymbol{\Phi}(\boldsymbol{x}_0, t). \tag{5.19}$$

We let (5.15b) be the solution to the Lyapunov equation, given $\boldsymbol{Q}_{ref} = \boldsymbol{Q}_{ref}^T > 0$ following

$$\boldsymbol{P}_{ref}\boldsymbol{A}_{ref} + \boldsymbol{A}_{ref}\boldsymbol{P}_{ref} = -\boldsymbol{Q}_{ref} \tag{5.20}$$

and define a Lyapunov function candidate (LFC)

$$\boldsymbol{V} = \boldsymbol{e}^\top \boldsymbol{P}_{ref}\boldsymbol{e} + \boldsymbol{Tr}\big(\tilde{\boldsymbol{K}}_x^\top \boldsymbol{\Gamma}_x^{-1}\tilde{\boldsymbol{K}}_x\Lambda\big) + \boldsymbol{Tr}\big(\tilde{\boldsymbol{\Theta}}^\top \boldsymbol{\Gamma}_\theta^{-1}\tilde{\boldsymbol{\Theta}}\boldsymbol{\Lambda}\big) \tag{5.21}$$

Differentiating (5.21) yields

$$\begin{aligned}
\dot{\boldsymbol{V}} =& 2\boldsymbol{e}_{ia}^\top \boldsymbol{P}_{ref}\big[\boldsymbol{A}_{ref}\boldsymbol{e}_{ia} + \boldsymbol{b}_{ia}\boldsymbol{\Lambda}\tilde{\boldsymbol{K}}_x^\top \boldsymbol{x}_{ia} + \boldsymbol{b}_{ia}\boldsymbol{\Lambda}\tilde{\boldsymbol{\Theta}}^\top \boldsymbol{\Phi}(\boldsymbol{x}_0, t)\big] \\
&+ 2\boldsymbol{Tr}\big(\tilde{\boldsymbol{K}}_x^\top \boldsymbol{\Gamma}_x^{-1}\dot{\tilde{\boldsymbol{K}}}_x\boldsymbol{\Lambda}\big) + 2\boldsymbol{Tr}\big(\tilde{\boldsymbol{\Theta}}^\top \boldsymbol{\Gamma}_\theta^{-1}\dot{\tilde{\boldsymbol{\Theta}}}\boldsymbol{\Lambda}\big) && \text{(5.22a)} \\
=& 2\boldsymbol{e}_{ia}^\top \boldsymbol{P}_{ref}\boldsymbol{A}_{ref}\boldsymbol{e}_{ia} + 2\boldsymbol{e}_{ia}^\top \boldsymbol{P}_{ref}\boldsymbol{b}_{ia}\boldsymbol{\Lambda}\tilde{\boldsymbol{K}}_x^\top \boldsymbol{x}_{ia} \\
&+ 2\boldsymbol{Tr}\big(\tilde{\boldsymbol{K}}_x^\top \boldsymbol{\Gamma}_x^{-1}\dot{\tilde{\boldsymbol{K}}}_x\boldsymbol{\Lambda}\big) + 2\boldsymbol{Tr}\big(\tilde{\boldsymbol{\Theta}}^\top \boldsymbol{\Gamma}_\theta^{-1}\dot{\tilde{\boldsymbol{\Theta}}}\boldsymbol{\Lambda}\big) && \text{(5.22b)} \\
=& -\boldsymbol{e}_{ia}^\top \boldsymbol{Q}_{ref}\boldsymbol{e}_{ia} + 2\boldsymbol{Tr}\big(\tilde{\boldsymbol{K}}_x^\top \boldsymbol{x}_{ia}\boldsymbol{e}_{ia}^\top \boldsymbol{P}_{ref}\boldsymbol{b}_{ia}\boldsymbol{\Lambda}\big) - 2\boldsymbol{Tr}\big(\tilde{\boldsymbol{K}}_x^\top \boldsymbol{\Gamma}_x^{-1}\dot{\tilde{\boldsymbol{K}}}_x\boldsymbol{\Lambda}\big) \\
&+ 2\boldsymbol{Tr}\big(\tilde{\boldsymbol{\Theta}}^\top \boldsymbol{\Phi}(\boldsymbol{x}_0, t)\boldsymbol{P}_{ref}\big) + 2\boldsymbol{Tr}\big(\tilde{\boldsymbol{\Theta}}^\top \boldsymbol{\Gamma}_\theta^{-1}\dot{\tilde{\boldsymbol{\Theta}}}\boldsymbol{\Lambda}\big) && \text{(5.22c)} \\
=& -\boldsymbol{e}_{ia}^\top \boldsymbol{Q}_{ref}\boldsymbol{e}_{ia} + 2\boldsymbol{Tr}\big(\tilde{\boldsymbol{K}}_x^\top \boldsymbol{x}_{ia}\boldsymbol{e}_{ia}^\top \boldsymbol{P}_{ref}\boldsymbol{b}_{ia}\boldsymbol{\Lambda}\big) - 2\boldsymbol{Tr}\big(\tilde{\boldsymbol{K}}_x^\top \boldsymbol{\Gamma}_x^{-1}\dot{\tilde{\boldsymbol{K}}}_x\boldsymbol{\Lambda}\big) \\
&+ 2\boldsymbol{Tr}\big(\tilde{\boldsymbol{\Theta}}^\top \boldsymbol{\Phi}(\boldsymbol{x}_0)\boldsymbol{e}_{ia}^\top \boldsymbol{P}_{ref}\boldsymbol{b}_{ia}\boldsymbol{\Lambda}\big) - 2\boldsymbol{Tr}\big(\tilde{\boldsymbol{\Theta}}^\top \boldsymbol{\Gamma}_\theta^{-1}\dot{\tilde{\boldsymbol{\Theta}}}\boldsymbol{\Lambda}\big) && \text{(5.22d)} \\
=& -\boldsymbol{e}_{ia}^\top \boldsymbol{Q}_{ref}\boldsymbol{e}_{ia} + 2\boldsymbol{Tr}\big(\tilde{\boldsymbol{K}}_x^\top \big[\boldsymbol{x}_{ia}\boldsymbol{e}_{ia}^\top \boldsymbol{P}_{ref}\boldsymbol{b}_{ia} - \dot{\tilde{\boldsymbol{K}}}_x\boldsymbol{\Gamma}_x^{-1}\big]\boldsymbol{\Lambda}\big) \\
&+ 2\boldsymbol{Tr}\big(\tilde{\boldsymbol{\Theta}}\big[\boldsymbol{\Phi}(\boldsymbol{x}_0, t)\boldsymbol{e}_{ia}^\top \boldsymbol{P}_{ref}\boldsymbol{b}_{ia} - \dot{\tilde{\boldsymbol{\Theta}}}\boldsymbol{\Gamma}_\theta^{-1}\big]\boldsymbol{\Lambda}\big), && \text{(5.22e)}
\end{aligned}$$

resulting in the update laws

$$\begin{aligned}
\dot{\tilde{\boldsymbol{K}}}_x^\top &= \boldsymbol{\Gamma}_x\boldsymbol{x}\boldsymbol{e}^\top \boldsymbol{P}_{ref}\boldsymbol{b}_{ia} && \text{(5.23a)} \\
\dot{\tilde{\boldsymbol{\Theta}}} &= \boldsymbol{\Gamma}_\theta\boldsymbol{\Phi}(\boldsymbol{x}_0, t)\boldsymbol{e}^\top \boldsymbol{P}_{ref}\boldsymbol{b}_{ia}. && \text{(5.23b)}
\end{aligned}$$

This results in the negative semi-definite function

$$\boldsymbol{V} = -\boldsymbol{e}^\top \boldsymbol{Q}_{ref}\boldsymbol{e} \leq 0 \tag{5.24}$$

which can prove that the equilibrium of the closed loop system $(\boldsymbol{e}, \boldsymbol{K}_x^\top, \tilde{\boldsymbol{\Theta}}) = (0, 0, 0)$ is uniformly globally stable (UGS). This is done by applying LaSalle-Yoshisawa which shows that $\boldsymbol{e}(t) \to 0$ as $t \to \infty$ (explained in Fossen (2011), Skjetne (2016) and Khalil (2015)). It is possible to extend (5.16) including a direct stabilizing term resulting in

$$\delta = -\hat{\boldsymbol{K}}_x^\top \boldsymbol{x} - \hat{\boldsymbol{\Theta}}^\top \boldsymbol{\Phi}(\boldsymbol{x}_0, t) - k_p \boldsymbol{b}_{ia}^\top \boldsymbol{P}_{ref}(\boldsymbol{x}_{ia} - \boldsymbol{x}_{ref}) \tag{5.25}$$

5.1.2 Direct MRAC Design by Augmenting a Baseline Control Law

For a baseline augmented MRAC design the starting point is similar to (5.1) with an extra term Lavretsky and Wise (2012)

$$\dot{\boldsymbol{x}}_{bl} = \boldsymbol{A}_{bl}\boldsymbol{x}_{bl} + \boldsymbol{B}_{bl}\boldsymbol{\Lambda}(\delta + \boldsymbol{\Theta}^\top \boldsymbol{\Phi}(\boldsymbol{x}_0, t)) + \boldsymbol{B}_{ref}\boldsymbol{y}_{cmd} \tag{5.26a}$$

$$\boldsymbol{y}_{bl} = \boldsymbol{C}_{bl}\boldsymbol{x}_{bl} + \boldsymbol{D}_{bl}\boldsymbol{\Lambda}(\delta + \boldsymbol{\Theta}^\top \boldsymbol{\Phi}(\boldsymbol{x}_0, t)), \tag{5.26b}$$

where $\boldsymbol{A}_{bl}, \boldsymbol{B}_{bl}, \boldsymbol{C}_{bl}$ and $\boldsymbol{D}_{bl}$ are known matrices. δ, $\boldsymbol{\Theta}$, $\boldsymbol{\Phi}(\boldsymbol{x}_0, t)$ and Λ are defined as in (5.1).

Now, $\boldsymbol{\Lambda} = \boldsymbol{I}$ and $\boldsymbol{\Theta} = 0$ is applied to (5.26) simplifying it to

$$\dot{z} = \boldsymbol{A}z + \boldsymbol{B}v \tag{5.27a}$$

$$y = \boldsymbol{C}z + \boldsymbol{D}v. \tag{5.27b}$$

For this system, a baseline control law is designed as a linear quadratic regulator (LQR) cost function

$$\boldsymbol{J} = \int_0^\infty \left(\boldsymbol{z}^\top \boldsymbol{Q}\boldsymbol{z} + v^\top \boldsymbol{R}v\right), \tag{5.28}$$

for which the optimized PID-control law for the baseline controller is given as

$$v = -R^{-1}\boldsymbol{B}^\top \boldsymbol{P}\boldsymbol{z} = -\boldsymbol{K}_{lqr}^\top \boldsymbol{z} = -K_i^\top \xi - K_p^\top x_0, \tag{5.29}$$

where $\boldsymbol{Q} = \boldsymbol{Q}^\top, \boldsymbol{R} = \boldsymbol{R}^\top$ are chosen such that $\boldsymbol{P} = \boldsymbol{P}^\top$ is the solution of the algebraic Riccatti equation (ARE)

$$\boldsymbol{P}\boldsymbol{A} + \boldsymbol{A}^\top \boldsymbol{P} - \boldsymbol{P}\boldsymbol{B}\boldsymbol{R}^{-1}\boldsymbol{B}^\top \boldsymbol{P} = 0. \tag{5.30}$$

This results in the baseline control law

$$\delta_{bl} = -\boldsymbol{K}_{lqr}^\top \boldsymbol{x}. \tag{5.31}$$

Plant Model

The plant model is still based on the nonlinear extension of the Nomoto model shown in (5.3). As $D = 0$ the plant dynamics are expressed in the same way as (5.5), with the same matrices as described in (5.4). Since the system has three states the LQR controller from (5.31) will include a derivative term making it similar to (5.10).

Reference Model

The reference model is very similar to the one presented in (5.9), but is extended with an additional term. This model is referred to as an observer-like model (Lavretsky and Wise, 2012) (Skjetne, 2016) and is as follows

$$
\begin{aligned}
\dot{\boldsymbol{x}}_{ref} &= \sqrt{\frac{g}{L}}\boldsymbol{H}^{-1}\boldsymbol{A}^{''}_{ref}\boldsymbol{H}\boldsymbol{x}_{ref} + \sqrt{\frac{g}{L}}\boldsymbol{H}^{-1}\boldsymbol{L}^{''}_{v}\boldsymbol{H}(\boldsymbol{x}_{bl} - \boldsymbol{x}_{ref}) + \boldsymbol{b}_{ref}y_{cmd} \\
\boldsymbol{y}_{ref} &= \boldsymbol{c}\boldsymbol{x}_{ref},
\end{aligned}
\tag{5.32}
$$

where

$$
\boldsymbol{L}^{''}_{v} = \sigma\boldsymbol{P}^{''}_{v}(\boldsymbol{R}^{''}_{v})^{-1} \tag{5.33}
$$

$$
\boldsymbol{R}^{''}_{v} = \frac{v}{v+1}\boldsymbol{I}. \tag{5.34}
$$

Chosing,

$$
\boldsymbol{Q}^{''}_{v} = \boldsymbol{Q} + \frac{v+1}{v}\boldsymbol{I} \tag{5.35}
$$

$\boldsymbol{P}^{''}_{v} = \boldsymbol{P}^{''T}_{v}$ is the solution to

$$
\boldsymbol{P}^{''}_{v}(\boldsymbol{A}^{''T}_{ref}) + \boldsymbol{A}^{''}_{ref}(\boldsymbol{P}^{''}_{v}) - \sigma\boldsymbol{P}^{''}_{v}(\boldsymbol{R}^{''}_{v}) + \boldsymbol{Q}^{''}_{v} = 0 \tag{5.36}
$$

and σ enables state feedback in reference filters if $\sigma = 1$ (if feedback is disabled, $\sigma = 0$).

Control- and Update- Laws

The control law chosen for (5.5) is the sum

$$
\delta = -\delta_{bl} + \delta_{ad}, \tag{5.37}
$$

where δ_{bl} is the baseline control input and δ_{ad} is the adaptive correction term.
Inserted into (5.5) results in

$$
\begin{aligned}
\dot{\boldsymbol{x}} &= \boldsymbol{A}_{bl}\boldsymbol{x}_{bl} + \boldsymbol{b}_{bl}\boldsymbol{\Lambda}\big(\delta_{ad} + \delta_{bl} + \boldsymbol{\Theta}^{\top}\boldsymbol{\Phi}(\boldsymbol{x}_0, t)\big) \\
&\quad + \boldsymbol{b}_{ref}y_{cmd} + \boldsymbol{b}_{bl}u_{bl} - \boldsymbol{b}_{bl}u_{bl} && \text{(5.38a)} \\
&= \boldsymbol{A}_{ref}\boldsymbol{x}_{bl} + \boldsymbol{b}_{bl}\boldsymbol{\Lambda}\big[\delta_{ad} + \boldsymbol{K}_{\delta}^{\top}\delta_{bl} + \boldsymbol{\Theta}^{\top}\boldsymbol{\Phi}(\boldsymbol{x}_0, t)\big] + \boldsymbol{b}_{ref}y_{cmd} && \text{(5.38b)} \\
&= \boldsymbol{A}_{ref}\boldsymbol{x}_{bl}\big[\delta_{ad} + \boldsymbol{\Omega}^{\top}\boldsymbol{\Upsilon}(\boldsymbol{x}, t)\big] + \boldsymbol{b}_{ref}y_{cmd}, && \text{(5.38c)}
\end{aligned}
$$

where $\boldsymbol{K}_\delta = \boldsymbol{\Lambda}^{-1} - 1$ is a unknown gain,

$$\boldsymbol{\Omega} = \begin{bmatrix} K_\delta \\ \boldsymbol{\Theta} \end{bmatrix}, \quad \boldsymbol{\Upsilon}(x) = \begin{bmatrix} \delta_{bl} \\ \boldsymbol{\Phi}(\boldsymbol{x}_0, t) \end{bmatrix} \tag{5.39}$$

In order to choose the update law for Ω we use the solution of (5.36), $\boldsymbol{e} = \boldsymbol{x}_{bl} - \boldsymbol{x}_{ref}$ and the LFC

$$V = \boldsymbol{e}_{bl}^\top \boldsymbol{P}_v^{-1} \boldsymbol{e}_{bl} + \boldsymbol{Tr}\big(\tilde{\boldsymbol{\Omega}} \boldsymbol{\Gamma}_\Omega^{-1} \tilde{\boldsymbol{\Omega}} \boldsymbol{\Lambda}\big). \tag{5.40}$$

Differentiating it yields

$$\begin{aligned} \dot{V} &= 2\boldsymbol{e}_{bl}^\top \boldsymbol{P}_v^{-1} \boldsymbol{A}_v \boldsymbol{e}_{bl} + 2\boldsymbol{e}_{bl}^\top \boldsymbol{P}_v^{-1} \boldsymbol{b}_v \boldsymbol{\Lambda} \tilde{\boldsymbol{\Omega}} \boldsymbol{\Upsilon}(\boldsymbol{x}, t) + 2\boldsymbol{Tr}\big(\tilde{\boldsymbol{\Omega}} \boldsymbol{\Gamma}_\Omega^{-1} \dot{\tilde{\boldsymbol{\Omega}}} \boldsymbol{\Lambda}\big) \\ &= -\boldsymbol{e}_{bl}^\top \big(\boldsymbol{P}_v^{-1} \boldsymbol{Q}_v \boldsymbol{P}_v^{-1} - \sigma \boldsymbol{R}_v^{-1}\big) \boldsymbol{e} + 2\boldsymbol{Tr}\big(\tilde{\boldsymbol{\Omega}}^\top \big[\boldsymbol{\Upsilon}(\boldsymbol{x}, t) \boldsymbol{e}_{bl}^\top \boldsymbol{P}_v^{-1} \boldsymbol{b}_{bl} - \boldsymbol{\Gamma}_\Omega^{-1} \dot{\tilde{\boldsymbol{\Omega}}}\big] \boldsymbol{\Lambda}\big). \end{aligned} \tag{5.41}$$

Looking at the last term of (5.41) the update law is chosen as

$$\dot{\boldsymbol{\Omega}} = \boldsymbol{\Gamma}_\Omega \boldsymbol{\Upsilon}(\boldsymbol{x}, t) \boldsymbol{e}^\top \boldsymbol{P}_v^{-1} \boldsymbol{b}_{bl} \tag{5.42}$$

which cancels out the last term resulting in

$$\dot{V} = -\boldsymbol{e}_{bl}^\top \big(\boldsymbol{P}_v^{-1} \boldsymbol{Q}_v \boldsymbol{P}_v^{-1} - \sigma \boldsymbol{R}_v^{-1}\big) \boldsymbol{e}_{bl} \leq 0. \tag{5.43}$$

Applying LaSalle-Yoshizawa proves UGS for the closed-loop equilibrium $(\boldsymbol{e}, \tilde{\boldsymbol{\Omega}}) = (0, 0)$ (Fossen, 2011) (Khalil, 2015).

5.2 Surge Controller

The MRAC for the surge controller was chosen for a scalar plant using the linearized surge-speed model (2.30) with unknown parameters. The system is similar to the scalar examples in Skjetne (2016) and Ioannou and Sun (2012), and is written as

$$\begin{aligned} \dot{u}_{ind} &= (a_0 + a_1 u_{ind} + a_2 |u_{ind}| u_{ind}) + b\delta \\ &= \boldsymbol{\phi}(u_{ind})^\top \boldsymbol{\theta} + b\delta, \end{aligned} \tag{5.44}$$

where $\boldsymbol{\theta} = [a_0, a_1, a_2]^\top$ consists of the unknown parameters and $\boldsymbol{\phi}(u_{ind}) = [1, u_{ind}, u_{ind}|u_{ind}|]^\top$ is a known regressor vector and the sign of b is assumed to be known.

Using normalized parameters (5.44) can be written as

$$\begin{aligned}\dot{u}^{"}_{ind} &= (a^{"}_0 + a^{"}_1 u^{"}_{ind} + a^{"}_2 |u^{"}_{ind}| u^{"}_{ind}) + b^{"} \delta \\ &= \boldsymbol{\phi}(u^{"}_{ind})^\top \boldsymbol{\theta}^{"} + b^{"} \delta, \end{aligned} \tag{5.45}$$

which can be transformed to a expression using dimensional surge speed and input (here: bias, as δ is nondimensional) as in (2.47) resulting in

$$\begin{aligned}\dot{u}_{ind} &= \sqrt{\frac{g}{L}}(a^{"}_0 + \frac{a^{"}_1}{\sqrt{Lg}} u_{ind} + \frac{a^{"}_2}{Lg} |u_{ind}| u_{ind}) + b\delta \\ &= \boldsymbol{\phi}(u_{ind})^\top \boldsymbol{\theta} + b\delta, \end{aligned} \tag{5.46}$$

where $\boldsymbol{\theta} = [a^{"}_0, \frac{a^{"}_1}{\sqrt{gL}}, \frac{a^{"}_2}{gL}]^\top$ consists of the unknown scaled parameters and the regressor vector becomes $\boldsymbol{\phi}(u_{ind}) = [1, u_{ind}, |u_{ind}|u_{ind}]^\top$. The sign of b is still assumed to be known.

In state space form the plant dynamics of a scalar system is written as

$$u_{ind} = -a_p u_{ind} + b_p \delta, \tag{5.47}$$

where a_p and b_p represents $\boldsymbol{\phi}(u_{ind})^\top \boldsymbol{\theta}$ and b from (5.46).

A surge-speed reference model from Fossen (2011) is described as

$$\dot{u}_{ref} = -k_p u_{ref} - k_p u_d + \dot{u}_d. \tag{5.48}$$

In (5.48) k_p is a proportional gain, u_{ref} is the reference surge speed $u_d = y_{cmd}$ and $\dot{u}_d = \dot{y}_{cmd}$ is the desired acceleration. This reference model can also be written as a function of normalized parameters. For dimensional velocity and input forces (5.48) can be written as

$$\dot{u}_{ref} = -\sqrt{\frac{g}{L}} k^{"}_p u_{ref} - \sqrt{\frac{g}{L}} k^{"}_p u_d + \dot{u}_d. \tag{5.49}$$

From equation (5.49) the following system scalars and vectors can be obtained by (5.50)

$$a_{ref} = \sqrt{\frac{g}{L}} k^{"}_p, \quad \boldsymbol{b}_{ref} = [-\sqrt{\frac{g}{L}} k^{"}_p, 1], \quad \boldsymbol{y}_{cmd} = [u_d, \dot{u}_d]^\top. \tag{5.50}$$

(5.49) can then be written as

$$\dot{u}_{ref} = -a_{ref} u_{ref} + \boldsymbol{b}_{ref} \boldsymbol{y}_{cmd} \tag{5.51}$$

and the following control law is proposed

$$\delta = -k(t)u_{ind} + \boldsymbol{l}(t)\boldsymbol{y}_{ref}, \tag{5.52}$$

$$= \rho\alpha(u_{ind}, t) \tag{5.53}$$

where

$$k(t) = \frac{a_{ref} + \hat{a}_p}{\hat{b}_p}, \quad \boldsymbol{l}(t) = \frac{\boldsymbol{b}_{ref}}{\hat{b}_p}. \tag{5.54}$$

a_{ref} and $\boldsymbol{b}_{ref}$ are as in (5.50). $\hat{a}_p$ and $\hat{b}_p$ are estimates of the unknown plant from (5.47). $\rho = \frac{1}{b}$ such that $\tilde{\rho} = \hat{\rho} - \rho$ can be expressed by

$$b\tilde{\rho} = 1 - b\hat{\rho}, \tag{5.55}$$

which can simplify the expression and avoid using the estimates in the denominator.

The unknown plant can be written as (5.56)

$$u_{ind} = \hat{a}_p u_{ind} + \hat{b}_p \delta, \tag{5.56}$$

Now the $a_{ref}u_{ind}$ is addedboth sides of (5.46) as shown in (5.57)

$$\dot{u}_{ind} = -a_{ref}u_{ind} + (a_{ref} + a_p)u_{ind} + b\delta. \tag{5.57}$$

The same is done for the estimated plant dynamics accordingly by adding $a_{ref}\hat{u}_{ind}$ to both sides

$$\dot{\hat{u}}_{ind} = -a_{ref}\hat{u}_{ind} + (a_{ref} + \hat{a}_p)\hat{u}_{ind} + \hat{b}_p\delta. \tag{5.58}$$

By application of the *Laplace transformation* u_{ind} and $\hat{u}_{ind}$ can be expresed as

$$u_{ind} = \frac{1}{s + a_{ref}}[(a_{ref} + a_p)u_{ind} + b\delta] \tag{5.59}$$

$$\hat{u}_{ind} = \frac{1}{s + a_{ref}}[(a_{ref} + \hat{a}_p)u_{ind} + \hat{b}\delta] \tag{5.60}$$

Now, the error dynamics of the actual and estimated plants is written as

$$e = u_{ind} - \hat{u}_{ind} \tag{5.61}$$

$$= \frac{1}{s + a_{ref}}[(a_p - \hat{a}_p)u_{ind} - (b_p - \hat{b}_p)\delta] \tag{5.62}$$

$$\tag{5.63}$$

using $e_{ind} = u_{ind} - u_{ref}$, $\tilde{a}_p = a_p - \hat{a}_p$ and $\tilde{b}_p = b - \hat{b}_p$ the derivative of the error becomes

$$\dot{e} = a_{ref}e - \tilde{a}u_{ind} - \tilde{b}\delta. \tag{5.64}$$

Now a_p and $\tilde{a}_p$ are replaced by $\boldsymbol{\Phi}^\top(u_{ind})\boldsymbol{\Theta}$ and $\boldsymbol{\Phi}^\top(u_{ind})\hat{\boldsymbol{\Theta}}$ as in the original equation (5.44).

By replacing $\tilde{b}_p$ with (5.55) and choosing the LFC as

$$V = \frac{1}{2}\big(e^2 + \tilde{\boldsymbol{\theta}}^\top \boldsymbol{\Gamma}^{-1}\tilde{\boldsymbol{\theta}} + \frac{|b|}{\gamma_b}\tilde{\rho}^2\big) \tag{5.65}$$

and differentiating (5.65) results in

$$\begin{aligned} \dot{V} &= -k_p e_{ind}^2 + \tilde{\boldsymbol{\theta}}^\top \boldsymbol{\Phi}(u_{ind})u_{ind} - b\tilde{\rho}\alpha(u_{ind}, \hat{\boldsymbol{\theta}})u - \tilde{\boldsymbol{\theta}}^\top \boldsymbol{\Gamma}^{-1}\dot{\hat{\boldsymbol{\theta}}} - \frac{|b|}{\gamma_b}\tilde{\rho}\dot{\hat{\rho}} && (5.66a) \\ &= -k_p e_{ind}^2 + \tilde{\boldsymbol{\theta}}^\top \big[\boldsymbol{\phi}(u_{ind})e_{ind} - \boldsymbol{\gamma}^{-1}\dot{\hat{\boldsymbol{\theta}}}\big] - \tilde{\rho}|b|\big[\text{sgn}(b)\alpha(u_{ind}, \hat{\boldsymbol{\theta}})e_{ind} + \frac{1}{\gamma_b}\dot{\hat{\rho}}\big]. && (5.66b) \end{aligned}$$

The update laws for (5.66a) are chosen as

$$\dot{\hat{\boldsymbol{\theta}}} = \boldsymbol{\Gamma}\boldsymbol{\phi}(u)e_{ind} \tag{5.67}$$

$$\dot{\hat{\rho}} = -\gamma_b sgn(b)\alpha(u_{ind}, \hat{\boldsymbol{\theta}})e_{ind} \tag{5.68}$$

and renders the equilibrium $(e_{ind}, \boldsymbol{\theta}, \rho) = (0, 0, 0)$ UGS proven using LaSalle-Yoshizawa as

$$\dot{V} = -k_p e^2 \leq 0 \tag{5.69}$$

5.3 Robustification Methods

For parameter estimation it is important to include robustification. The first method that will be presented is the dead-zone modification.

5.3.1 Dead-zone Modificator

This modification reduces chattering from noise and sudden drifting of estimates when the tracking error between plant and reference is small. It simply shuts down the estimation of parameters, until the error becomes significant. Lavretsky and Wise (2012), presents the following scalar function for the dead-zone modification

$$\mu(|e|) = \max\bigg(0, \min\bigg(1, \frac{|e| - \delta e_0}{(1-\delta)e_0}\bigg)\bigg), \tag{5.70}$$

where $0 < \delta < 1, 0 < e_0 \ll 1$ are positive scalars. The robustification term $\mu(|e|)$ is multiplied to the update laws of the estimates and ensures Uniformly Ultimate Boundedness (UUB) for the tracking error e.

5.3.2 Projection Operator

In Section 4.2, the projection operator was introduced in order to guarantee boundedness of parameters in a kinematic observer design. This is also the case for robustification of adaptive update laws in control design. Lavretsky and Wise (2012, Chapter 11.4) and Krstiĉ (1995) shows the procedure of implementing a projection function.

For a bounded parameter $\boldsymbol{\theta} \in \mathbb{R}^p$, where $|\boldsymbol{\theta}| \leq \boldsymbol{\theta}_{max}$ a convex function is presented as

$$f(\theta) = \frac{(1+\epsilon)\theta^\top\theta - \theta_{max}^2}{\epsilon\theta_{max}^2} \tag{5.71}$$

and the gradient of (5.71) is

$$\nabla f = \frac{2(1+\epsilon)}{\epsilon\theta_{max}^2}\theta. \tag{5.72}$$

Using (5.71) and (5.72), the projection function can then be written as

$$Pr(\theta, \Gamma y) = \begin{cases} \Gamma y - \frac{\Gamma\nabla f^\top(\nabla f)}{(\nabla f)\Gamma(\nabla f)}\Gamma y f & \text{if } f > 0 \text{ and } y^\top\Gamma(\nabla f) \\ \Gamma y & \text{elsewhere,} \end{cases} \tag{5.73}$$

where $Pr(\theta, \Gamma y)$ is the modified update law for the parameter $\dot{\theta} = \Gamma y$.
Defining the two sets Ω_0 and Ω_1, where

$$\Omega_0 := \{\theta \in \mathbb{R}^p : f(\theta) \leq 0\} = \left\{\theta \in \mathbb{R}^p : |\theta| \leq \frac{\theta_{max}}{\sqrt{1+\epsilon}}\right\} \tag{5.74}$$

$$\Omega_1 := \{\theta \in \mathbb{R}^p : f(\theta) \leq 1\} = \left\{\theta \in \mathbb{R}^p : |\theta| \leq \theta_{max}\right\}, \tag{5.75}$$

$$\tag{5.76}$$

ensure that if $\theta(0) \in \Omega_0$, then $\theta(t) \in \Omega_1 \forall t \geq 0$ (Lavretsky and Wise, 2012).

5.4 Simulation Study of the Controllers

In this section the three types of MRAC algorithms will be simulated in order to show that they can be used to steer the two vessels CSEI and R/V Gunnerus. The controllers will first be implemented for the CSEI model vessel. Then some practical examples of how to robustify the controllers will be presented before finally scaling the controllers in order to check whether the R/V Gunnerus vessel can be controlled with the same controllers as the CSEI model.

5.4.1 MRAC for CSEI

The first thing to do is to define the test scenario for which the controllers are simulated. In this initial simulation with CSEI using MATLAB/Simulink the desired surge velocity will be 0.2 m/s while the heading angle will be implemented as a step function varying the desired heading between 0° and 60° as shown in Figure 5.2

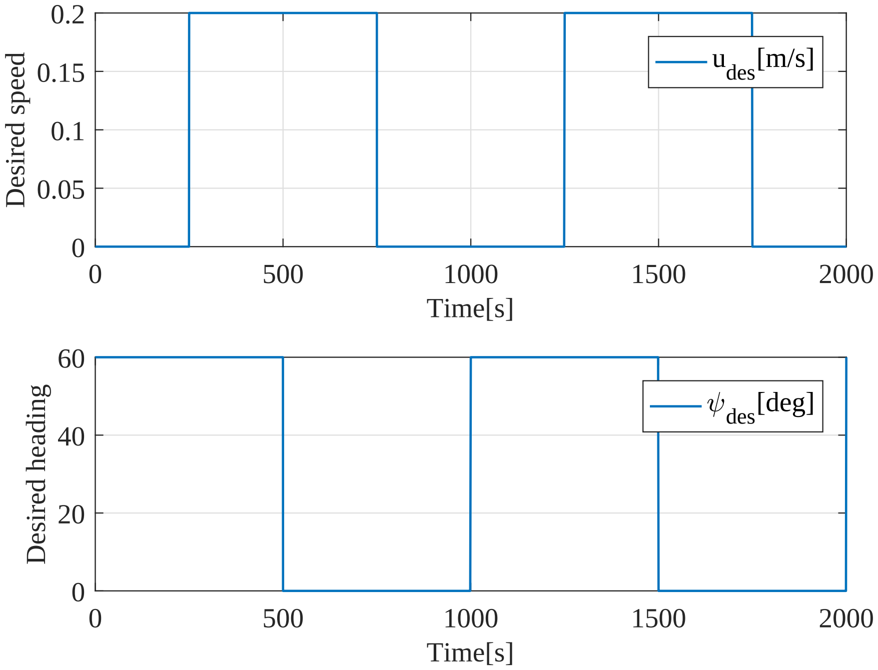

Figure 5.2: Desired surge velocity and heading for CSEI

The heading can be controlled by either the vectorial MRAC with integral action from 5.1.1 or the MRAC augmented with a baseline controller from Section 5.1.2. For the first simulation, the vectorial MRAC with integral action was chosen and by implementing the control law (5.16) together with the update laws (5.23) the following results were obtained, shown in Figure 5.3

Figure 5.3, shows the reference model from (5.6) together with the true values and Figure 5.4 shows the estimated parameters for the same simulation.

As it is possible to see from Figure 5.3, the reference frame is being tracked accurately for the whole simulation time in all states. This proves that the controller is able to control CSEI to the right heading. The estimated parameters from Figure 5.4 shows that the $K_{est} = \hat{K}_x$ estimates stays close to its initial condition throughout the simulation while the $\theta_{est} = \hat{\theta}$ parameters

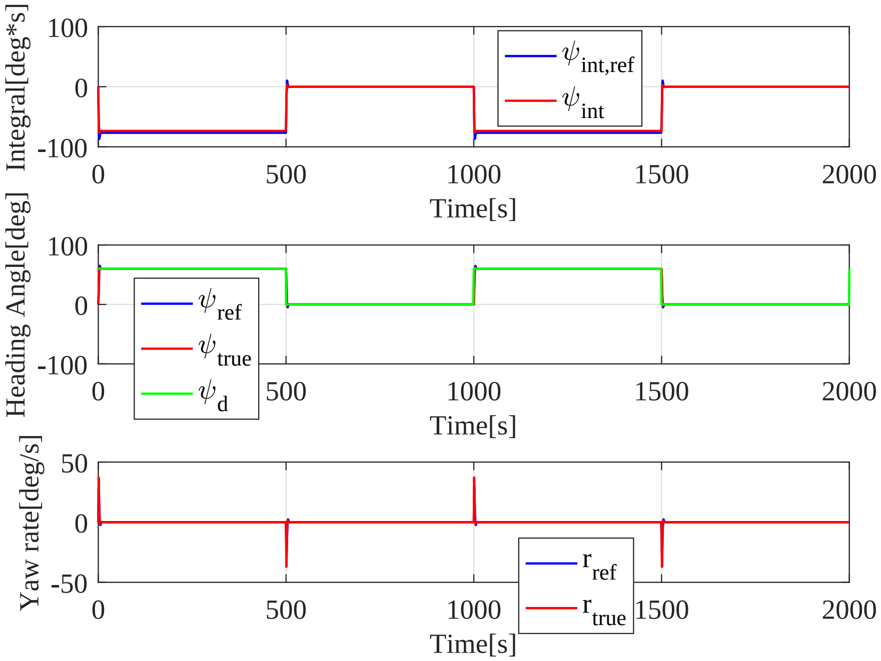

Figure 5.3: Reference states together with the corresponding measured states

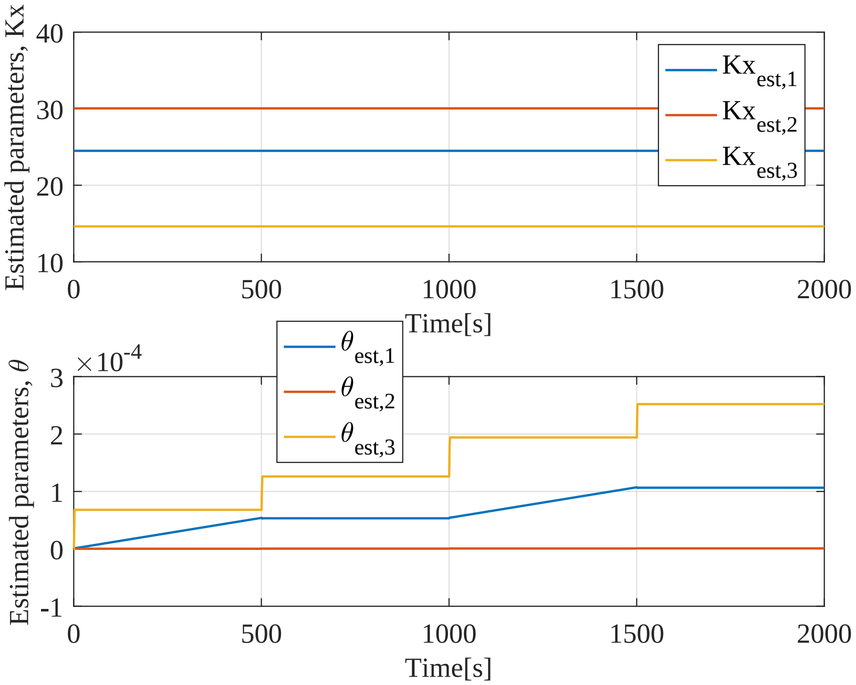

Figure 5.4: Parameter estimates for MRAC with integral action

slowly diverge away from zero. This divergence is so small that it does not affect the performance in any way.

The surge speed is controlled by the indirect adaptive controller presented in Section 5.2. The desired surge speed is set constant to 0.2 m/s for the whole simulation and the result is shown in figures 5.5 and 5.6.

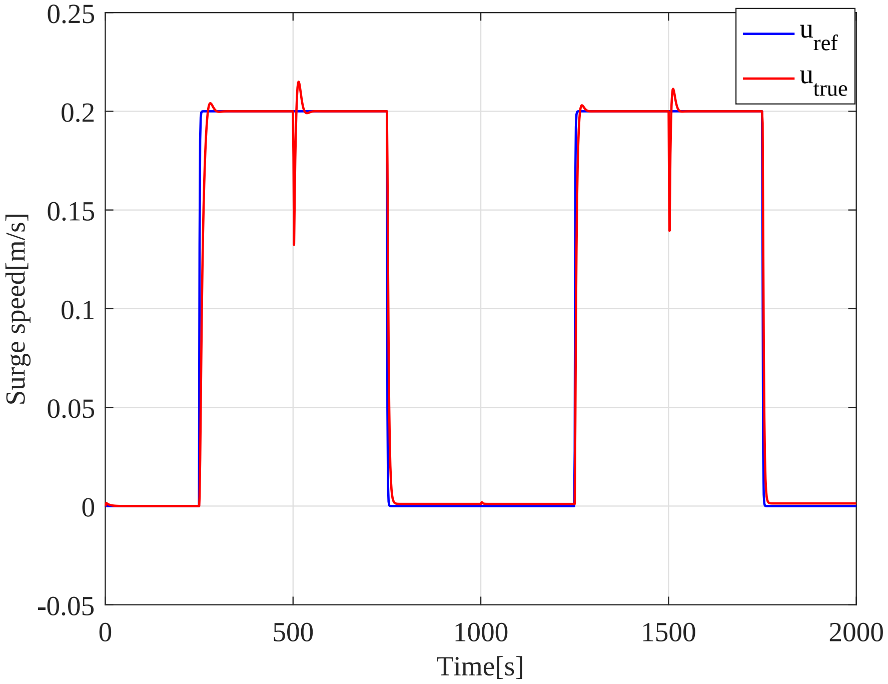

Figure 5.5: Surge reference model compared to actual values

Starting in Figure 5.5 it is possible to see that the reference model is quick to get to the desired value. The controller, however, does not manage to keep up with the reference. This can be fixed by tuning the controller to make it more aggressive. Also, the spikes in the plot is not due to errors in the simulations, but because of the heading changes.

Figure 5.6 shows how the surge parameter estimates evolve during the simulation. They may look rough-edged, but looking at how the heading changes in Figure 5.2 it is clear that this is what makes the estimates making the small jumps in value.

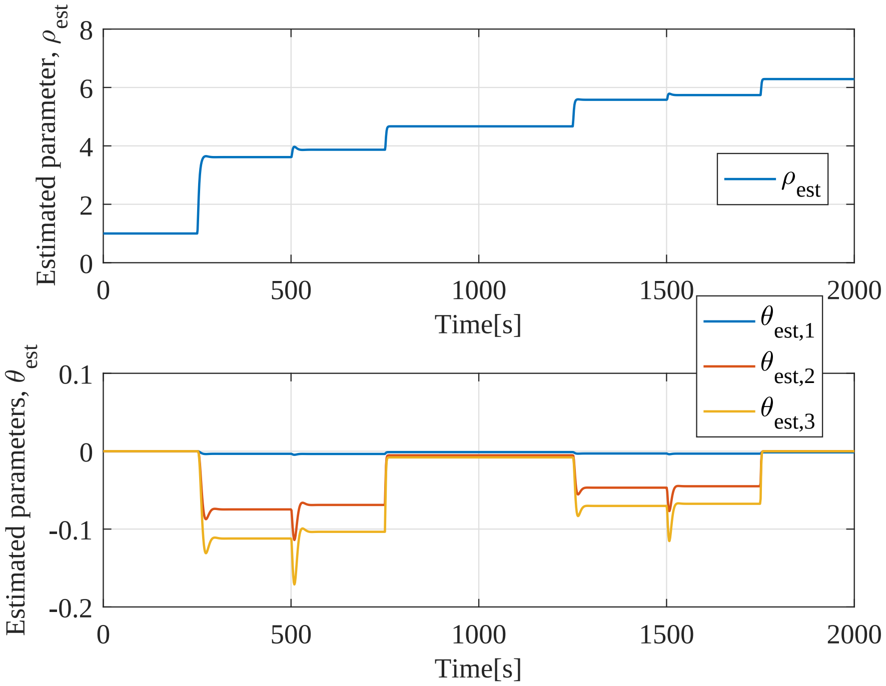

Figure 5.6: Estimated controller gains $\hat{\rho}$ and $\hat{\theta}_i$

Finally, the vectorial MRAC with integral action is replaced with the augmented baseline MRAC. The results are quite similar to the other heading controller as can be seen from figures 5.7 and 5.8, but with larger errors and more drift in the parameter values. With better tuning, this controller will most likely be as good as the vectorial MRAC with integral action.
The controller input from the simulation is summed up in Figure 5.9.

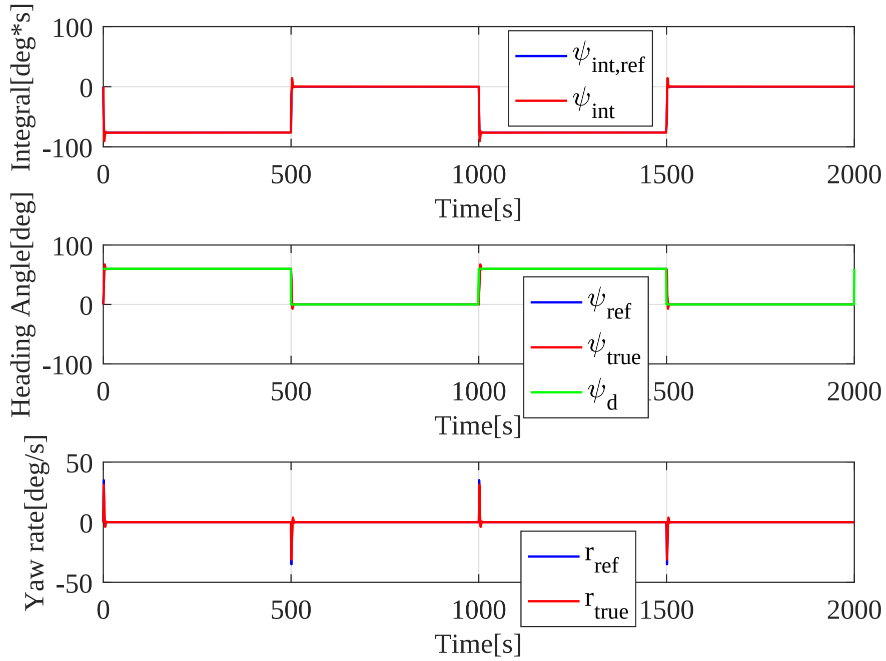

Figure 5.7: Reference states together with the corresponding measured states for baseline MRAC

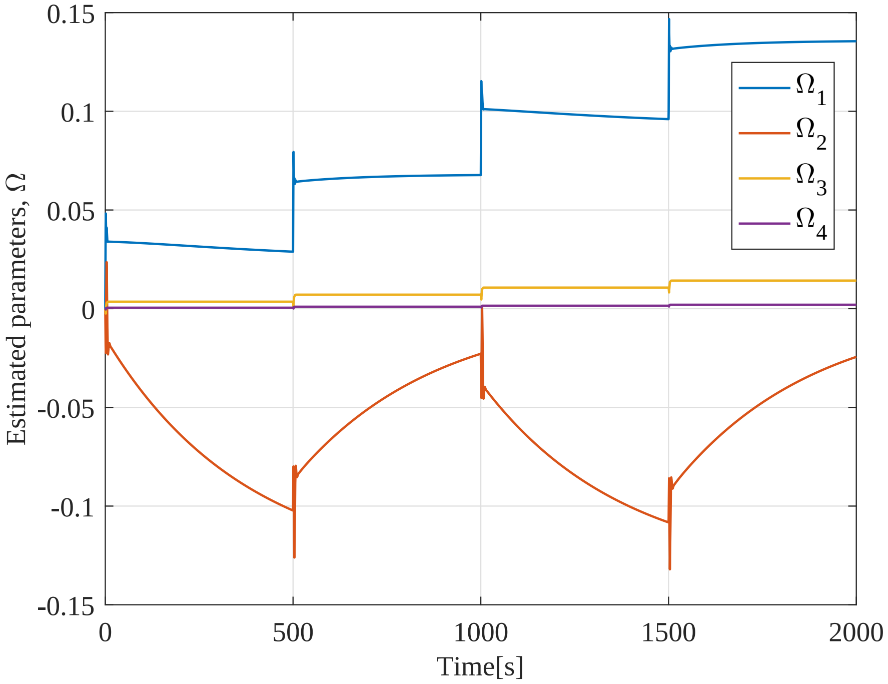

Figure 5.8: Parameter estimates for the baseline MRAC

5.4.2 Robustification of the Controllers

In Figure 5.10 the adaptation gains have been turned as high as possible in order to provoke instabilities. The plots are from a separate simulation, but is used here to prove how the robus-

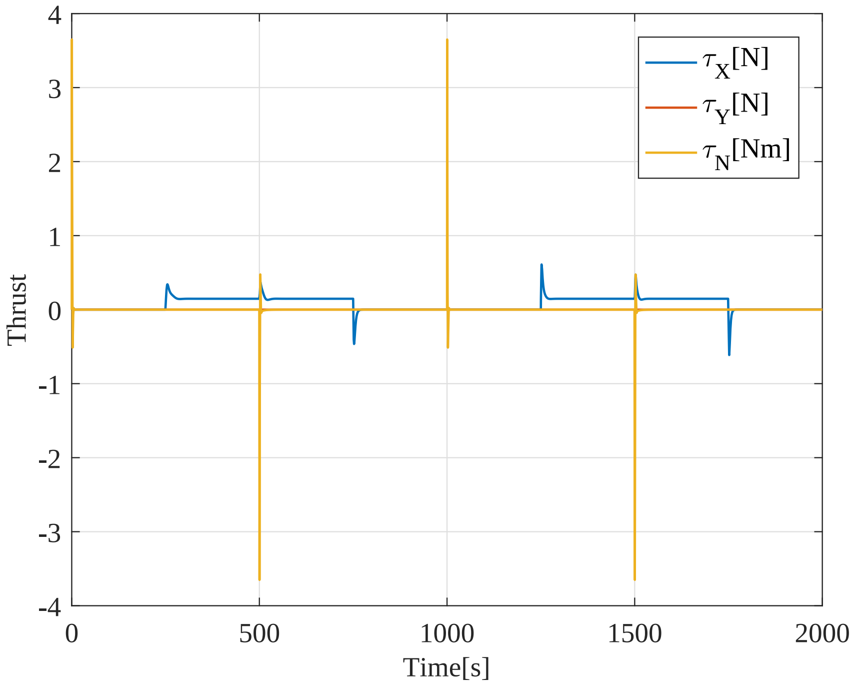

Figure 5.9: Control inputs for the simulation

tification methods affect the stability and ensures boundedness of solutions.

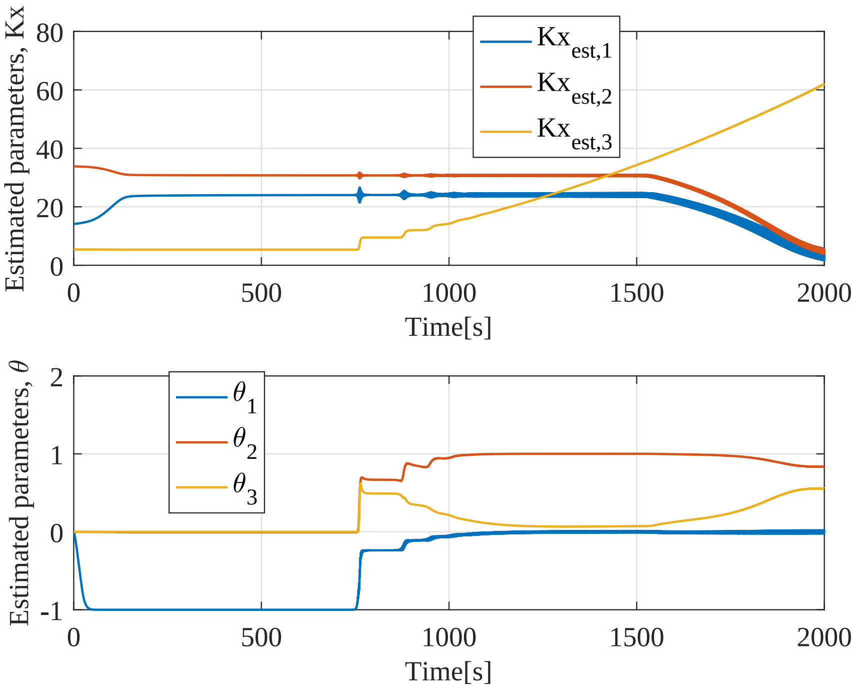

Figure 5.10: Chattering on parameter estimates

From about 750 s in Figure 5.10, small oscillations appear. This is called chattering and seem to have little effect in terms of instability. However, this induces a lot of oscillations to the control inputs which again makes the whole system gradually less stable. After 1500 s the estimated Kx-terms ($\hat{K}_x$) seem to drift off from their previous fixed values. The estimated θ ($\hat{\theta}$) terms are smaller in magnitude, but chattering can also be seen in the same figure from about 800 s.

By applying the dead-zone modification the chattering is removed. It stops adaptation when the error between reference plant and actual plant is small. The projection operator bounds the estimates and prevent drifting. The results of applying robustification can be seen in Figure 5.11.

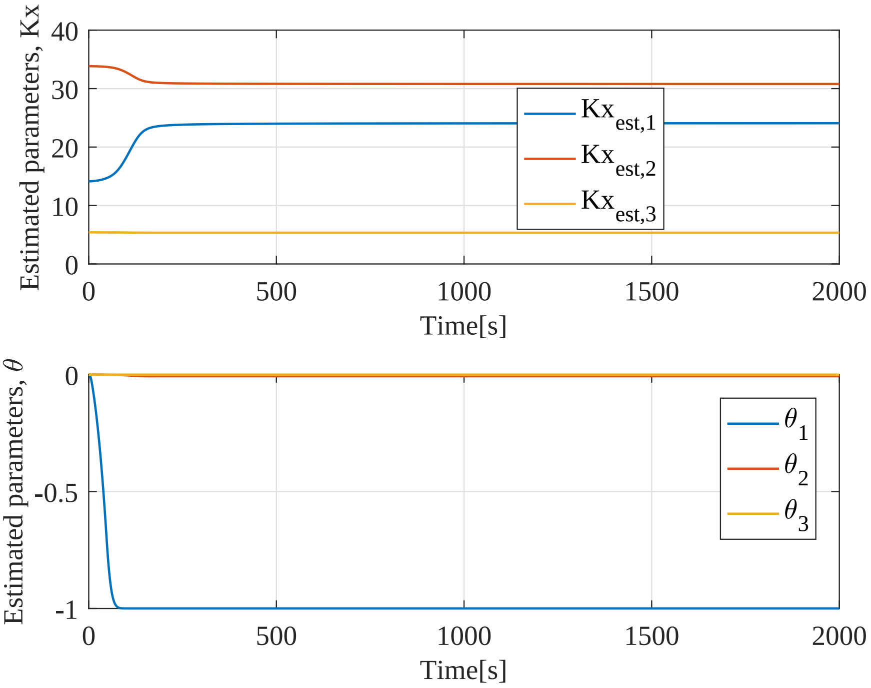

Figure 5.11: Chattering removed by dead-zone modification

5.4.3 HIL Simulations of the MRAC

Figures 5.12 and 5.13 are the results of a HIL simulation in which the desired surge speed is kept constant as the commanded heading is changed in steps. From previous simulations it is clear that the controllers work very well and this is yet again proved in this HIL simulation. The true speed and heading converges to the desired values with no sign of instabilities.

This means that also the controllers are ready for implementation on the physical model. Since they worked in HIL tests, the path towards physical testing will be short. This is because the software used in HIL simulations is the same as in physical experiments.

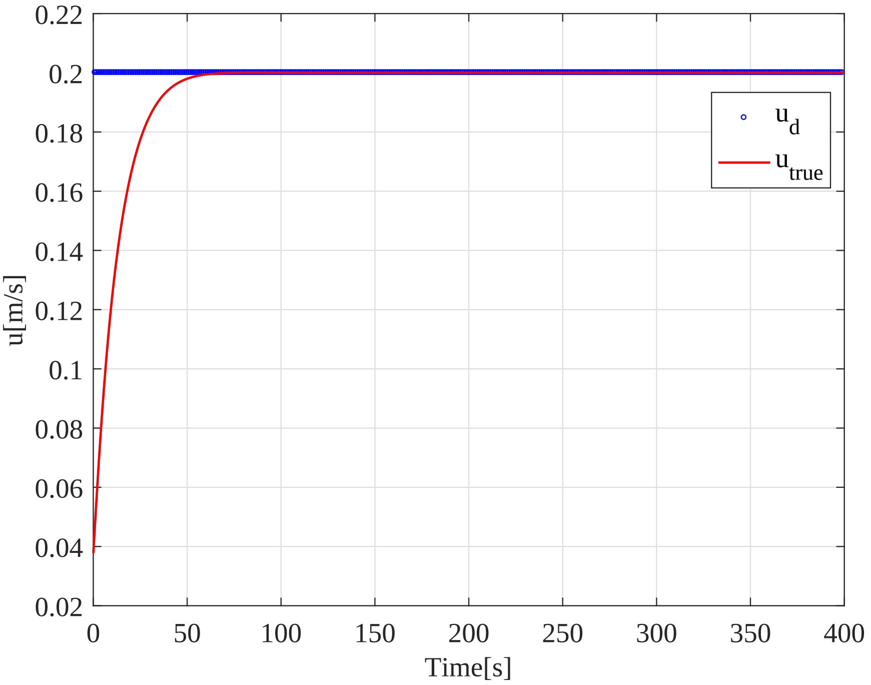

Figure 5.12: Desired and actual surge velocity from HIL simulation

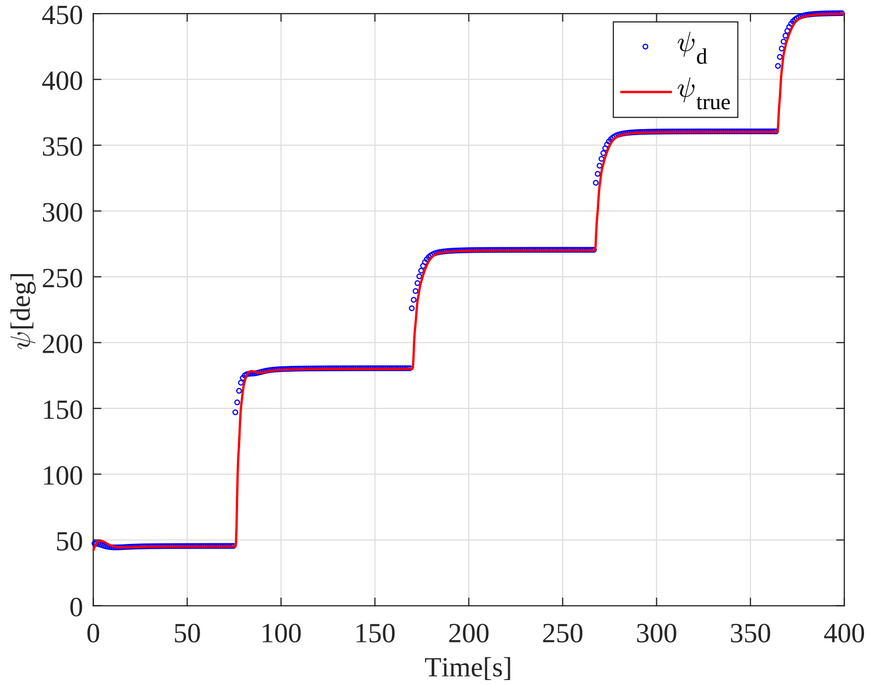

Figure 5.13: Desired and actual heading from HIL simulation

5.4.4 Simulating Scaled Controllers on the R/V Gunnerus Model

In this section the controllers that was successfully tested on CSEI in the sections 5.4.1 and 5.4.2 are going to be scaled with the length of R/V Gunnerus in order to see if the controllers work when scaled. The test scenario is similar to what is done in previous simulations using steps to regulate the desired surge speed and heading angle. The commanded velocity of the vessel is increased to 4 m/s and will also make to steps during the simulation time. The heading angle is still varied between 0° and 60° in steps as before. Figure 5.14 shows how the two set points varies during the simulation. The simulations are done using the robustified control laws from Section 5.4.2.

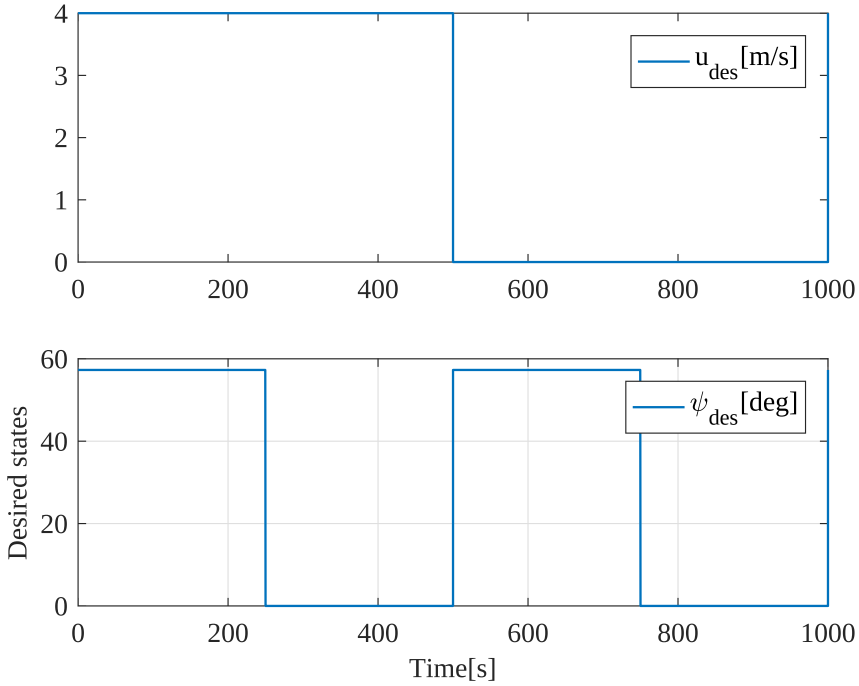

Figure 5.14: Desired surge velocity and heading for CSEI

Beginning with the heading from the vectorial integral action MRAC, Figure 5.15 shows how the controller manages to keep track of the commanded heading. The middle plot shows that the desired heading is reached and that the actual heading, heading rate and the integral term follow the reference plant as it is supposed to.

The estimates from the controller are shown in Figure 5.16. This plot shows that the estimates for $\hat{K}_x$ are constant throughout the simulations, but the $\hat{\theta}$ parameters vary at each step. Their values are too small to be affected by robustification which means that the gains can be tuned much higher if necessary.

The MRAC algorithm with a baseline control law yields similar results as shown in Figures 5.17 and 5.18. Note that this controller is slightly more aggressive in terms of yaw rate at each turn. Still, the results do not vary a lot between the heading controllers.

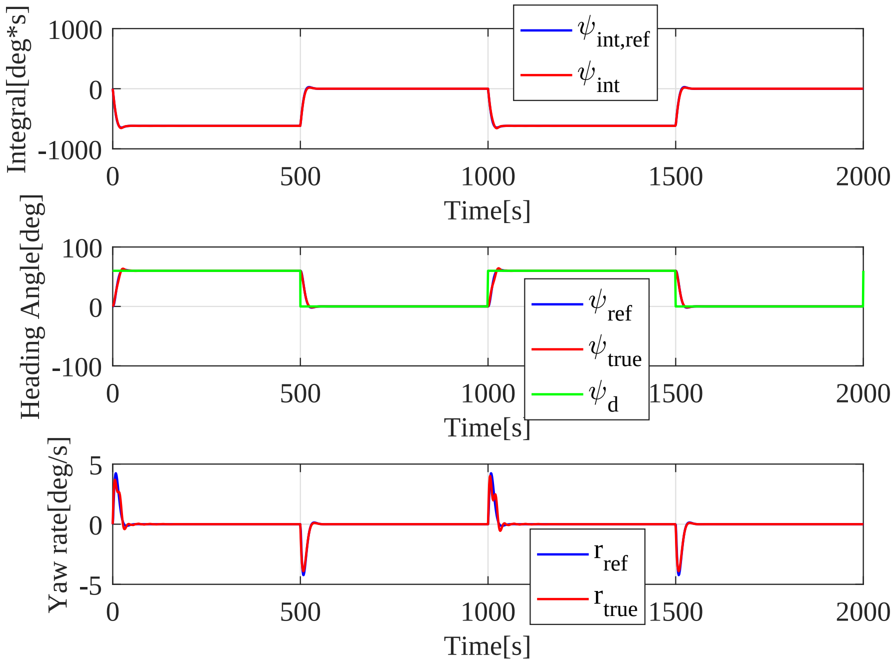

Figure 5.15: Results from scaled vectorial heading controller with integral action

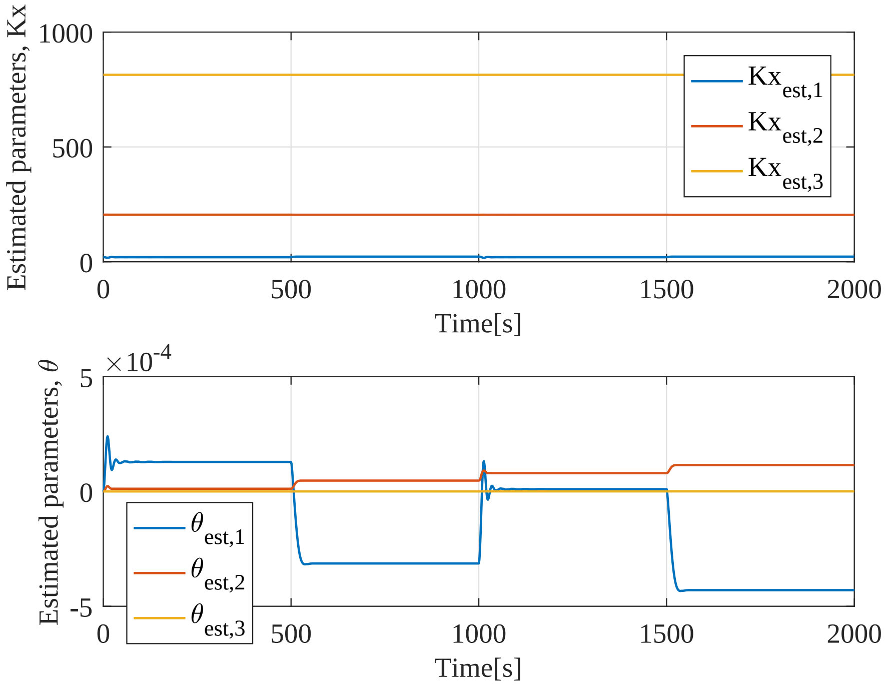

Figure 5.16: Estimated paremeter values for integral action MRAC for R/V Gunnerus

Finally, the surge speed model is scaled for R/V Gunnerus and shows that it too is able to work well with both vessels. This is shown in the Figures 5.19 and 5.20. These figures shows that one almost cannot separate the reference (in blue) and the true value (in red). Compared to (5.5)

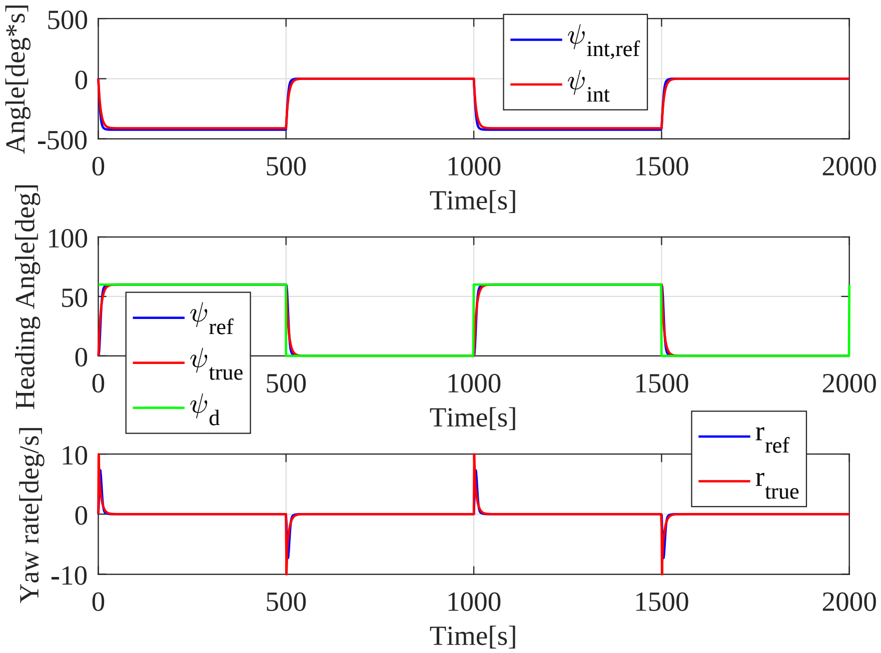

Figure 5.17: Results from scaled MRAC with a baseline control law for R/V Gunnerus

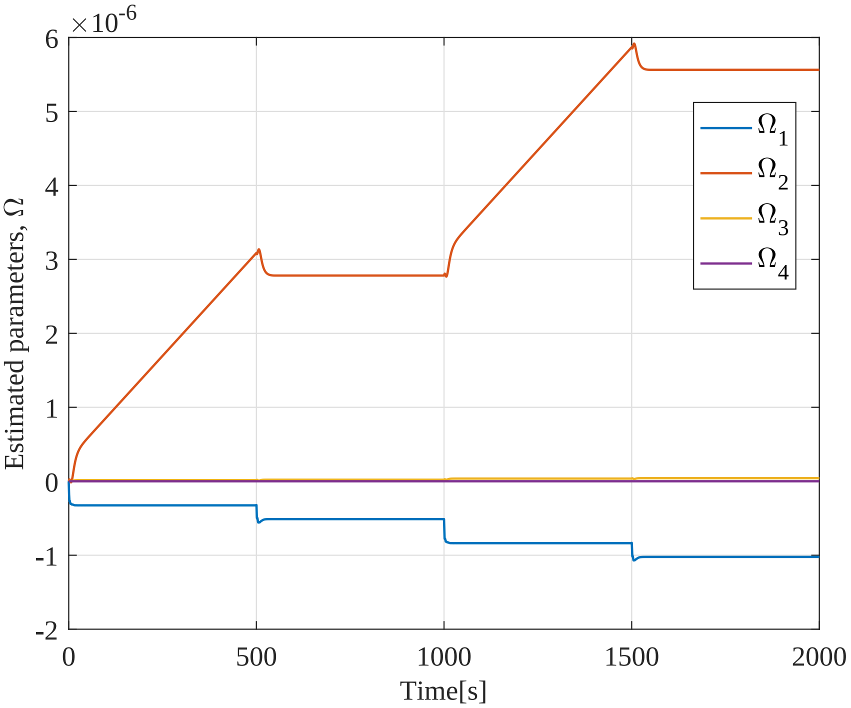

Figure 5.18: Estimated paremeter values for MRAC with a baseline control law for R/V Gunnerus

the difference is much smaller and does not have any spikes in the signal when the vessel turns or accelerates.

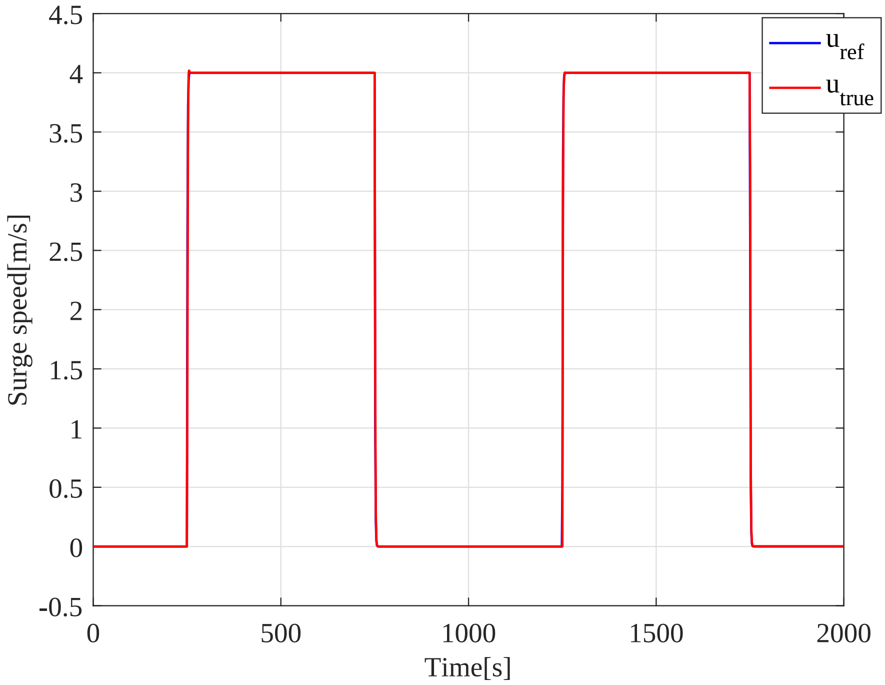

Figure 5.19: Results from scaled indirect MRAC for the surge-speed of R/V Gunnerus

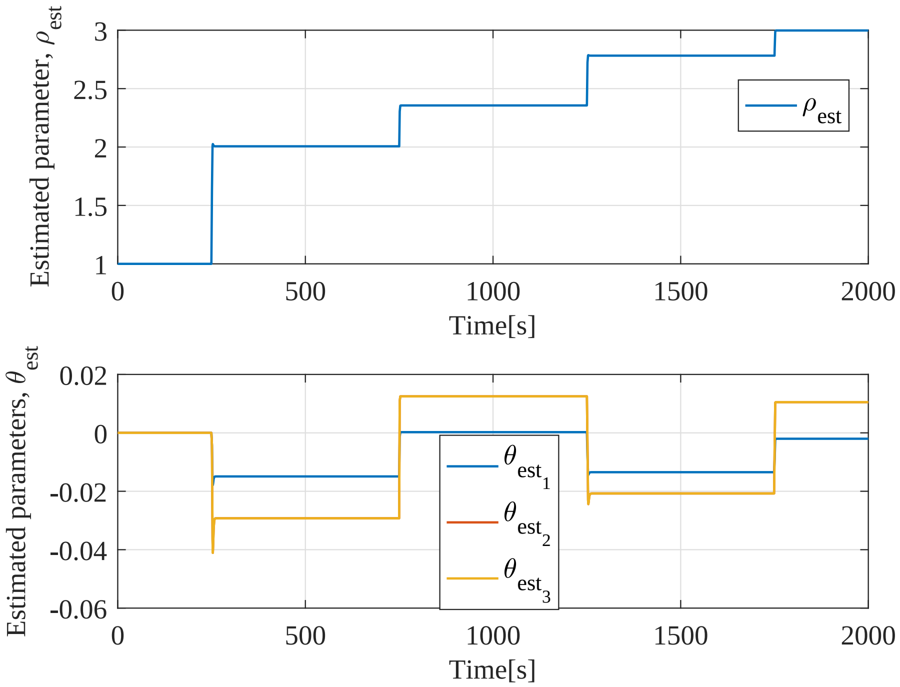

Figure 5.20: Estimated paremeter values for the indirect surge-speed MRAC for R/V Gunnerus

5.5 Implementation Issues on a Full Scale Test with R/V Gunnerus

During the sea trial with Kongsberg the MRAC studied in Section (5.1.1) was implemented on the full scale vessel of R/V Gunnerus. Although the simulations on the software seemed to work fine, problems occurred when testing the controller on the actual vessel. Firstly, the integrator increased in value as the parameters were set making it large before even the controller was put in close loop. The first thing to occur in closed-loop control is that the vessel turned far more than the actual commanded heading. After some time it stabilized and the integral value started dropping, making the heading close in to the commanded value. However, due to very little time for testing more could not be verified from the full scale tests.

This problem was solved by implementing a reset of all the control outputs. This meant that all the parameters could be set while the controller was running in open loop, before resetting the output when the controller was ready to go.

The second problem with the controllers on the cruises were that they had problems crossing $\pm 180^\circ$ heading. *pipi2infinf*-functions were added and although they had worked in simulations, they did not work well with the Kongsberg systems. This resulted in a sudden rotation of the vessel from +180° to -180° and vice versa, depending on which direction 180° was crossed.

In order to fix this problem the range of angles were first changed from $[-\pi, \pi]$ to $[0, 2\pi]$. Now by noticing in which direction the limits (0 or 2π) were crossed another 2π was added or subtracted from the original angles. Making it increase or decrease continually from $[-inf, inf]$. The vessel could now turn freely without risking the controller to make a sudden jump in heading angle.

5.6 Conclusions

Looking at the results from Section 5.4 all controllers performed very well even without robustification, both for the CSEI and the scaled controllers for R/V Gunnerus. This means that either of the heading controllers could be applied for heading control with satisfying performances. The surge-speed controller did also work very well, but could be tuned to be slighly more aggressive in order to reach cruise speed faster.

By adding strong disturbances to the vessels in form of current forces made the parameters drift. To prevent this dead-zone modification and the projection operator were included to the control laws. These robustification successfully reduced the drifting of parameters, making the controllers more reliable even when affected by disturbances.

To conclude, all controllers were successfully simulated and robustified. The scaling of procedure proved to work very well. It took some time to tune the scaled controller in order to perform well, but nontheless not as much as designing a new controller or identifying model parameters on a sea trial.

HIL simulations were done in order to test whether or not the controllers would work in the MC Lab with the physical model. The results were the same as for the rest of the simulations with both the heading controllers and the surge-speed controller providing promising results.

Chapter 6

Guidance

In this chapter guiding of underactuated surface vessels will be discussed. According to Fossen (2011) we divide guidance into three main categories. These are called set-point regulation, trajectory tracking and path following. In set-point regulation the aim is to move from one way-point to another. The attitude and the position of the next way-point are chosen as constants. For trajectory tracking a predefined moving reference is tracked along the desired path. In path-following, the goal is to follow a predefined path independent of time constraints. For this thesis path following and path tracking will be further investigated.

To able to navigate using guidance it is important to know in which direction, for how long and along which path. Therefore, it is necessary to start with making the actual paths that the vessel is going to follow. For straight-lines heading control is enough in order to steer the vessel to the next position (Fossen, 2011). A normal extension to straight line paths between desired points is to make smooth turns along circular arcs when the vessel is in range of the next way-point. These path types are called Dubin paths (Dubins, 1957). For path following and trajectory tracking the normal way of generating paths is through parameterization, genreating the paths at a given rate. The path generation presented in this thesis build mainly on Skjetne (2005), Fossen (2011), Lekkas (2014) and Dubins (1957).

Having generated the paths it is time to make the vessel follow them. In this thesis one guidance laws will be discussed. It is called Line-of-sight guidance calculates a correction term for the heading which gradually converges to zero when the vessel is on the path. This way, the vessel points towards the path while being far away from the path moving fast towards it, before gradually converging to the path. For this guidance law, current compensation can be added to the LOS algorithm either by introducing the sideslip angle (Fossen, 2011) or by Integral LOS (Børhaug, 2008). Here, the compensation term is multiplied with a gain inside the convergence term. This gain can be set to zero when no current is present, reducing the ILOS algorithm to the conventional LOS method. Lekkas (2014) and Skjetne et al. (2011) can be used in order to develop an understanding of LOS guidance. LOS and ILOS are going to be applied for straight-line- and for curved- paths using the procedure presented in Skjetne (2005), Caharija (2014), Caharija et al. (2016), and Lekkas (2014).

6.1 Steering Laws for Regular Paths

In this section the different trajectories and guidance laws for time independent path-following applications will be derived. LOS guidance will be derived for the generated paths in order to minimize the cross-track error.

6.1.1 Straight-lines Between Waypoints and Circular Paths

This thesis focuses on straight line paths in addition to circular paths. First, trajectories are designed by controlling the heading for path following objectives.

Waypoints and Straight Lines

Waypoints are defined as coordinates in on the 2-dimensional surface plane as

$$\boldsymbol{p}_0^n = [x_0, y_0]^\top \tag{6.1}$$

$$\boldsymbol{p}_1^n = [x_1, y_1]^\top, \tag{6.2}$$

where $\boldsymbol{p_0^n}$ is the initial position or previous waypoint of the vessel and $\boldsymbol{p_1^n}$ the next waypoint. The heading of the path can be calculated as

$$\alpha_k = \text{atan2}\left(\frac{y_1 - y_0}{x_1 - x_0}\right). \tag{6.3}$$

(6.1) and (6.3) contains enough information in order to navigate between waypoints. However, by introducing circular arcs at the endpoints (Dubins (1957), Fossen (2011)) a smoother way of moving between desired positions is developed. Within a distance of the desired waypoint the heading is changed with a constant rate in the direction of the next waypoint until the vessel exit the region of turning. The drawback is that the yaw rate will not be continuous at the intersection between straight line and circle.

Circular Paths

For a circular path, Breivik and Fossen (2008) suggest the following. First, the origin of the circular path is denoted $\boldsymbol{p}_c^n = [x_c, y_c]^\top$ and the radius as $r_c > 0$. Using the current position of the vessel $\boldsymbol{p}^n(t) = [x(t), y(t)]^\top$, together with the circular path coordinates the desired path can be written as a function of the heading

$$\chi_p(t) = \chi_c(t) + \lambda\frac{\pi}{2}, \tag{6.4}$$

where λ is either 1 or -1 depending on whether the path is turning clockwise motion or counter-clockwise.

$$\chi_c(t) = \operatorname{atan2}\left(\frac{y(t) - y_c}{x(t) - x_c}\right). \tag{6.5}$$

6.1.2 Line-of-Sight Guidance

Fossen (2011), defines the velocity of a craft with 2-D planar motion as

$$U(t) := ||v(t)|| = \sqrt{\dot{x}(t)^2 + \dot{y}(t)^2} \geq 0 \tag{6.6}$$

and the course- or steering- angle of the vessel as

$$\chi(t) := \operatorname{atan2}(\dot{y}(t), \dot{x}(t)), \in \mathbb{S} := [-\pi, \pi]. \tag{6.7}$$

For straight line paths, the path-fixed coordinates can be derived by

$$\boldsymbol{\epsilon} = \begin{bmatrix} s(t) \\ e(t) \end{bmatrix} = \boldsymbol{R}^\top(\alpha_k)(\boldsymbol{p}^n(t) - \boldsymbol{p}_k^n), \tag{6.8}$$

where $\boldsymbol{p}^n(t)$ is the current position of the vessel and $\boldsymbol{p}_k^n$ is the position of the next waypoint or the spot in the path which the vessel is currently aiming at. α_k is the desired heading for the path. The along-track error is denoted as s(t) and the cross-track error as e(t). The overall control objective for straight line paths is that the vessel is steered along the line-of-sight vector ensuring

$$\lim_{t \to \infty} e(t) = 0. \tag{6.9}$$

The equation above can according to Breivik and Fossen (2008) be satisfied using one of two methods: enclosure-based steering or lookahead-based steering. The LOS vectors and other important parameters are shown in Figure 6.1. It is worth noticing that when no current forces are acting β will be 0 and χ_d will be equal to ψ_d.

Enclosure-Based Steering

Enclosure-based steering is made by initially choosing a large circle $(R > 0)$ around the vessel position $\boldsymbol{p}^n = [x, y]^\top$ which also intersect the desired path at two points. The intersection that

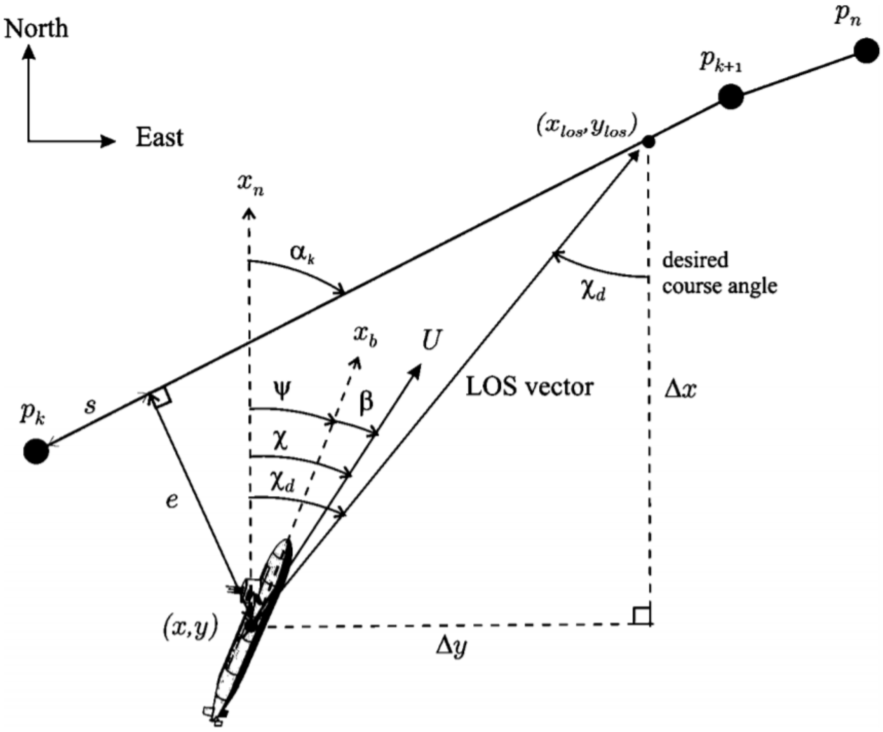
North
East
p_n
p_{k+1}
(x_{los}, y_{los})
x_n
α_k
desired
course angle
χ_d
x_b
U
ψ
β
LOS vector
Δx
p_k
s
χ
χ_d
e
(x,y)
Δy

Figure 6.1: LOS setup. [Courtesy: Fossen (2011)].

lies in the desired direction of the vessel is called $\boldsymbol{p}_{LOS} = [x_{LOS}, y_{LOS}]^\top$ and the vector from $\boldsymbol{p}$ to $\boldsymbol{p}_{LOS}$ is accordingly denoted the LOS-vector. Steering the ship along this vector fulfills (6.9).

The desired course angle is then calculated using Figure 6.1 according to

$$\chi_d(t) = \text{atan2}(y_{LOS} - y(t), x_{LOS} - x(t)). \tag{6.10}$$

To calculate the target intersection, the *Pythagorean theorem* is applied in addition to the heading of the path as shown in

$$[x_{LOS} - x(t)]^2 + [y_{LOS} - y(t)]^2 = R^2, \tag{6.11}$$

$$\tan(\alpha_k) = \frac{y_{k+1} - y_k}{x_{k+1} - x_k} = c, \tag{6.12}$$

where c is a constant parameter. Above, (6.12) corresponds to (6.3).

Lookahead-Based Steering

Lookahead-based steering is slighly less complicated than the enclosure-based method. The course angle is expressed as

$$\chi_d(t) = \chi_p + \chi_r(e), \tag{6.13}$$

where $\chi_p = \alpha_k$ is the path tangential angle described by (6.3) and

$$\chi_r = \arctan\left(\frac{-e}{\Delta}\right) \tag{6.14}$$

is the velocity-path relative angle. In Figure 6.1, it is the difference between α_k and χ_d. Δ is called the lookahead distance and refers to the distance between the direct projection of the vessel position on the path and the intersection between the LOS vector and the path. The relationship between the lookahead distance and the cross-track error can be derived using *Pythagorean theorem*

$$e(t)^2 + \Delta(t)^2 = R^2, \tag{6.15}$$

which relates the two different methods, because the lookahead-based guidance with

$$\Delta(t) = \sqrt{R^2 - e(t)^2}, \tag{6.16}$$

corresponds to the enclosure-based steering law, varying between 0 and R, when $|e(t)| = R$ and $|e(t)| = 0$, respectively (Fossen, 2011).

Steering Laws for Circles

For circles a lookahead-based approach is described in Breivik and Fossen (2008). Figure 6.2, shows how the relevant parameters relate. From (6.4) and (6.5) the desired heading of the path is derived. Inserting (6.4) as χ_p in (6.13), knowing that (6.4) satisfies (6.9), the cross-track error for circular paths is defined as

$$\begin{aligned} e(t) &= r_c - |\boldsymbol{p}(t) - \boldsymbol{p}_c| \\ &= r_c - \sqrt{((x(t) - x_c) - (y(t) - y_c))}. \end{aligned} \tag{6.17}$$

It is important to note that the lookahead distance is now expressed differently than for straight-line paths.

6.2 Steering Laws for Parameterized Paths

In this section paths will be generated by parameterization and these will be tracked in order to show that the path-tracking differs from path-following. Using LOS from Section 6.1.2 the goal will be to track the moving path such that both the along-track error and the cross-track error converge to zero. The related variables are shown in Figure 6.3

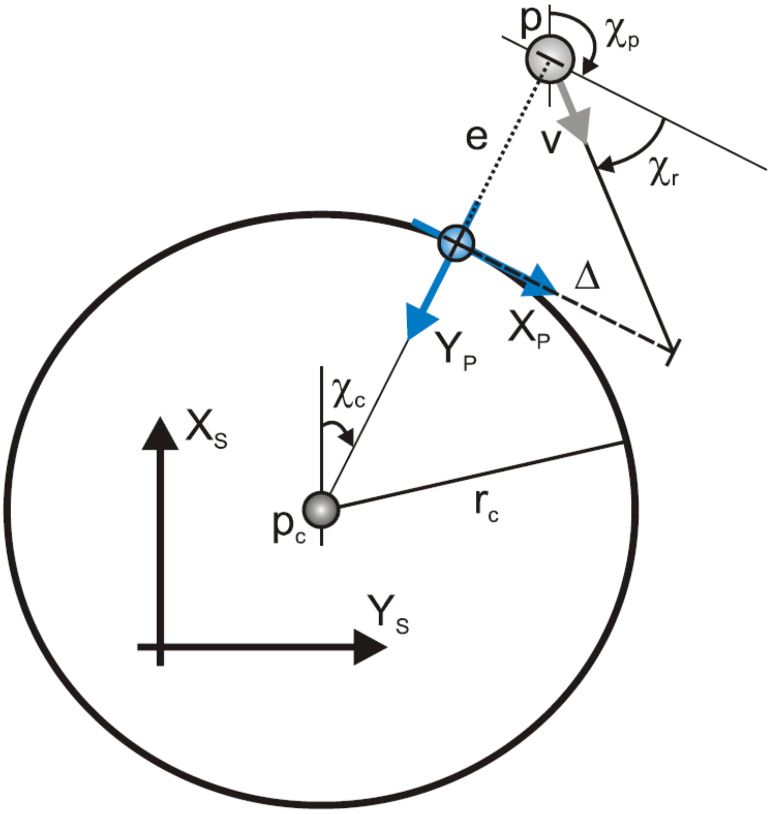
p
χ_p
e
v
χ_r
Δ
Y_P
X_P
χ_c
X_S
p_c
r_c
Y_S

Figure 6.2: LOS setup for circular path. [Courtesy: Breivik and Fossen (2008)].

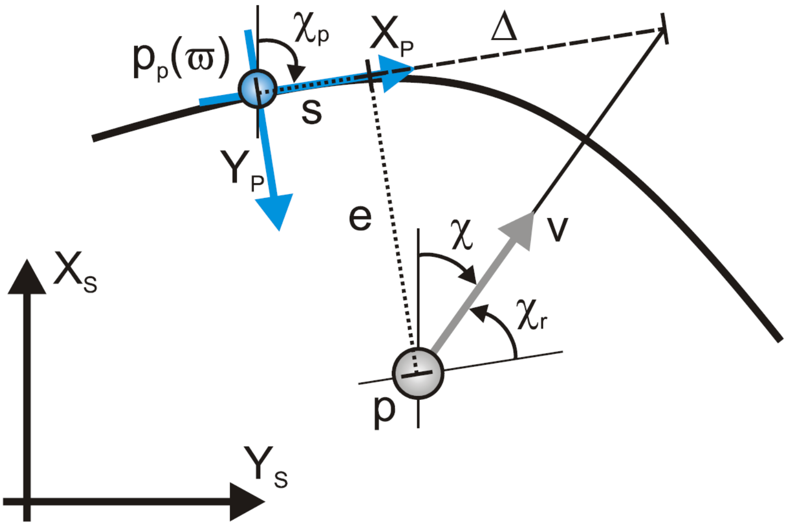
$p_p(\varpi)$
χ_p
X_P
Δ
s
Y_P
e
χ
v
X_S
χ_r
p
Y_S

Figure 6.3: LOS setup for parameterized paths. [Courtesy: Breivik and Fossen (2008)].

6.2.1 Parameterization of Paths

The parameterization of the paths are done by introducing a path variable that is zero at the starting point and increases as the vessel or target moves along it, constantly updating the positions. The paths discussed in this thesis will be straight line paths between waypoints and ellipsoid paths. Unlike shown in Figure 6.3, the parameterization variable will in this thesis be s and not $\bar{\omega}$. This follows the notation of Skjetne (2005) and Skjetne (2014). Straight lines between to waypoints as in (6.1) and (6.2) can be parameterized as

$$\boldsymbol{p}_d^n(s) = (\boldsymbol{p}_{d,1}^n - \boldsymbol{p}_{d,0}^n)s + \boldsymbol{p}_{d,0}^n, \tag{6.18}$$

using the same constant desired heading as in (6.3). The parameterization variables goes from 0 to 1 between the waypoints. It follows that

$$\boldsymbol{p}_d^n(0) = \boldsymbol{p}_0^n, \tag{6.19}$$

$$\boldsymbol{p}_d^n(1) = \boldsymbol{p}_1^n \tag{6.20}$$

and the desired path vector can be written as

$$\boldsymbol{\eta}_d = \begin{bmatrix} x_d \\ y_d \\ \chi_p \end{bmatrix} = \begin{bmatrix} (x_1 - x_0)s + x_0 \\ (y_1 - y_0)s + y_0 \\ \mathrm{atan2}(\boldsymbol{\eta}_d^s(2), \boldsymbol{\eta}_d^s(1)). \end{bmatrix}. \tag{6.21}$$

Note that χ_p in (6.21) and Figure 6.3 corresponds to χ_d in figure 6.1. The path derivatives with respect to the path variable are denoted as $\boldsymbol{\eta}_d^s$ and $\boldsymbol{\eta}_d^{s^2}$. For straight line paths they become

$$\boldsymbol{\eta}_d^s = \begin{bmatrix} x_1 - x_0 \\ y_1 - y_0 \\ 0 \end{bmatrix} \text{ and } \boldsymbol{\eta}_d^{s^2} = \begin{bmatrix} 0 \\ 0 \\ 0 \end{bmatrix}. \tag{6.22}$$

For an ellipsoid path a similar parameterization can be done by

$$x_d = r_1 \cos(2\pi s) + c_1, \tag{6.23}$$

$$y_d = r_2 \sin(2\pi s) + c_2, \tag{6.24}$$

where r_1 and r_2 are the radii of the ellipsoid in x- and y- direction and c_1 and c_2 is the coordinates of the origin. The desired heading angle is now a function of the path variable written as

$$\chi_p = \arctan(\boldsymbol{\eta}_d^s(2), \boldsymbol{\eta}_d^s(1)). \tag{6.25}$$

The complete path vector for an ellipsoid together with its derivatives are given as

$$\boldsymbol{\eta}_d = \begin{bmatrix} r_1\cos(2\pi s) + c_1 \\ r_2\sin(2\pi s) + c_2 \\ \mathrm{atan2}(\boldsymbol{\eta}^s(2), \boldsymbol{\eta}^s(2)) \end{bmatrix}, \quad \boldsymbol{\eta}_d^s = \begin{bmatrix} -2\pi r_1\sin(2\pi s) \\ 2\pi r_2\cos(2\pi s) \\ \frac{2\pi r_1 r_2}{r_1^2\sin(2\pi s)^2 + r_2^2\cos(2\pi s)^2} \end{bmatrix},$$

$$\boldsymbol{\eta}_d^{s^2} = \begin{bmatrix} -4\pi r_1\cos(2\pi s) \\ 4\pi r_2\sin(2\pi s) \\ \frac{4\pi^2(r_1 r_2(r_1^2 - r_2^2)\sin(4\pi s))}{(r_1^2\sin(2\pi s)^2 + r_2^2\cos(2\pi s)^2)^2} \end{bmatrix}. \tag{6.26}$$

6.2.2 Update Laws

The cross-track error for parameterized paths are calculated in the same way as in (6.8). For a point on the parameterized path $\boldsymbol{p}_p(s)$ Breivik and Fossen (2008) calculates the cross track error as

$$\boldsymbol{\epsilon}(t) = \begin{bmatrix} s(t) \\ e(t) \end{bmatrix} = \boldsymbol{R}(\psi_d)^\top(\boldsymbol{p}(t) - \boldsymbol{p}_p(s)). \tag{6.27}$$

The path-following objective is now extended from (6.9) to include along-track error, yielding

$$\lim_{t\to\infty} \boldsymbol{\epsilon}(t) = 0. \tag{6.28}$$

In order to achieve this the control system must solve two tasks as explained by Skjetne (2005), both the geometric- and dynamic assignments must be satisfied.

The paths presented in the previous sections are designed such that the path variable s is zero at the initial position and 1 at the final position. Two update laws are used in this thesis: tracking update law and gradient update law, both presented in Skjetne (2005). Note that the virtual point replacing $\boldsymbol{p}$ in Skjetne (2014) is replaced in order to be applicable for current forces on the vessel. For the tracking update the derivative of s, or the speed assignment is defined as

$$\dot{s} = v(s) = \frac{u_d}{|\boldsymbol{p}_d^s(s)|} = \frac{u_d}{\sqrt{(\boldsymbol{\eta}_x^s)^2 + (\boldsymbol{\eta}_y^s)^2}}, \tag{6.29}$$

where u_d is the desired velocity. (6.29) can be modified with a feedforward term (Skjetne, 2014) that stops s when the cross track error is large as shown in (6.30)

$$\dot{s} = \frac{\Delta}{\Delta^2 + e(\boldsymbol{p}, s)^2} v(s), \tag{6.30}$$

where Δ is the look-ahead distance and $e(\boldsymbol{p}, s)$ is the cross-track error between a point on the moving vessel ($\boldsymbol{p}$) and the path.

The gradient update law includes a third term called the gradient update witch renders (6.30) as

$$\dot{s} = \frac{\Delta}{\Delta^2 + e(\boldsymbol{p}, s)^2} v(s) - \omega_s(\boldsymbol{p}, s), \tag{6.31}$$

where

$$\omega_s(\boldsymbol{p}, s) = -\mu \frac{\boldsymbol{p}_d^s(s)}{|\boldsymbol{p}_d^s(s)|} (\boldsymbol{p} - \boldsymbol{p}_d) \tag{6.32}$$

and μ is a constant gain. The gradient term in (6.32) makes the vessel converge faster to a point on the path.

6.3 Current Compensation

In this section it is assumed that a constant irrotational current acts on the vessel. This results in that the vessel will drift if nothing is done to compensate for it. Two such methods are ILOS and Sideslip compensation and both can be applied directly in the existing LOS algorithms.

6.3.1 Sideslip Angle

In this thesis current forces will be compensated for by adding compensation terms to the Lookahead-based LOS method. The first method is described in Fossen (2011) and consists of adding an extra term β to (6.13), as shown in Figure 6.1.

$$\chi_p = \psi_d + \beta, \tag{6.33}$$

where ψ_d is the commanded heading of the vessel and

$$\beta = \arcsin\left(\frac{v}{U}\right) \tag{6.34}$$

is called the sideslip angle. v is the velocity in sway and U is the vessels cruising speed as defined in (6.6). By compensating for the additional sideslip in (6.13) the aim is to satisfy (6.9), even when current forces are present.

6.3.2 Integral Line-of-Sight

The second method was first presented by Børhaug (2008) and consist of adding an integral term to the path-tangential velocity term (6.14) of the lookahead equation (6.13). In addition, the expression for the integral term must be derived. The two equations are shown in below

$$\chi_r = -\arctan\left(\frac{e + \sigma e_{int}}{\Delta}\right), \Delta > 0, \tag{6.35}$$

$$\dot{e}_{int} = \frac{\Delta e}{\sqrt{\Delta^2 + (e^2 + \sigma e_{int})}}, \tag{6.36}$$

where e is the cross-track error, Δ is the lookahead distance, $\sigma > 0$ is a tunable gain and e_{int} is the integral state of the cross-track error. The introduction of the integral term builds up when the ocean currents drive the vessel away from the desired path, even if the desired heading angle is achieved. The $(e + \sigma e_{int})$ term will then be nonzero generating the necessary sideslip angle in order to compensate for the current forces. This can be compared to a sideslip term inside the velocity-relative angle term. Note that without ocean current, (6.35) reduces to (6.14).

6.4 Simulations of the Path-Following Algorithms

In this section simulations will be made to test various path-following and path-tracking methods discussed above. First, simulations will be done without current and current compensation to confirm that the algorithms works as expected. By adding current, the current compensator terms will be included in the simulations.

All following tests will be done using the observer from Chapter 4 and controllers derived through Chapter 5. Both vessel models will be simulated to show that everything works for both. As the previous chapters have shown that the control system works in simulations the following results will focus on showing the generated paths and how accurate the vessel is able to follow them. The current compensation is done using ILOS guidance.

The simulations will begin with the vessel at the origin $(x, y) = (0, 0)$. For straight-line paths the vessel will read the location of the next waypoint from a sorted matrix. When all the waypoints are passed the vessel will move with the last set heading until the simulation ends.

For circular path the vessel also starts at the $(x, y) = (0, 0)$, but the origin of the circle is set elsewhere. The vessels must be able to generate and track the paths from far away before finally converging to the paths.

6.4.1 Simulations of Path-Following and Path-Tracking for CSEI

First, the path generation and path-following will be tested for CSEI. Simulations will begin without adding current forces to the vessel model. Then, after ensuring everything works well current will be added and the results will be shown.

Path-Following

Using heading control only and with constant thrust in surge the CSEI will try to follow given paths as derived for straight lines and circles in Section 6.1.1.

Starting with a path consisting of straight lines between four waypoints, Figure 6.4 shows that the vessel has no problems in generating the path nor navigating along it. The waypoints lies at the corner of the square, but in order to show the desired path between them lines have been added. This makes it easier to analyze the cross-track error from this figure. The cross-track error can be seen converge to zero shortly after each turn. In Figure 6.5, it is proved that this is the case. The vessel starts at the origin and continues in the last set heading after all waypoints are passed.

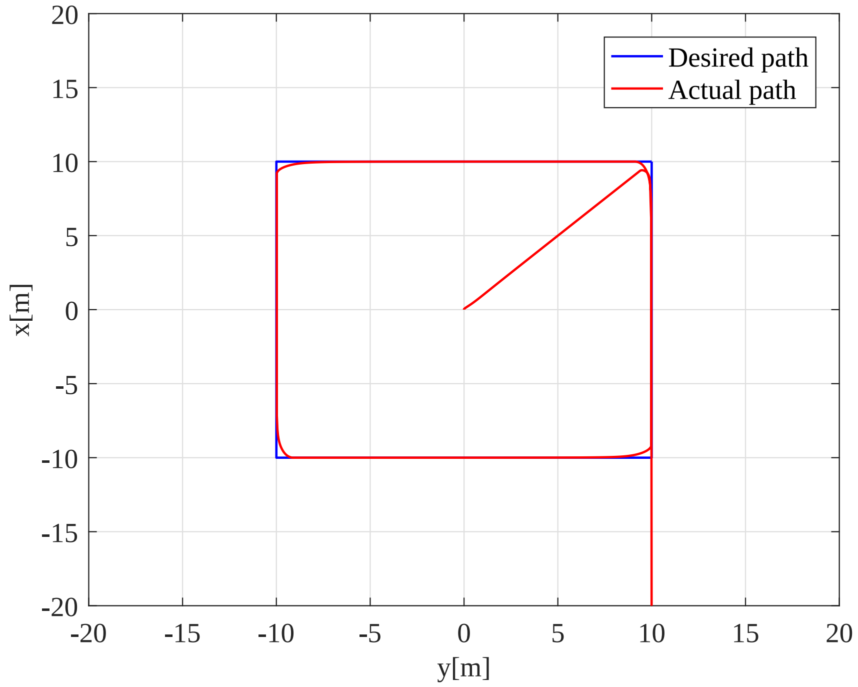

Figure 6.4: Straight-line path in between waypoints

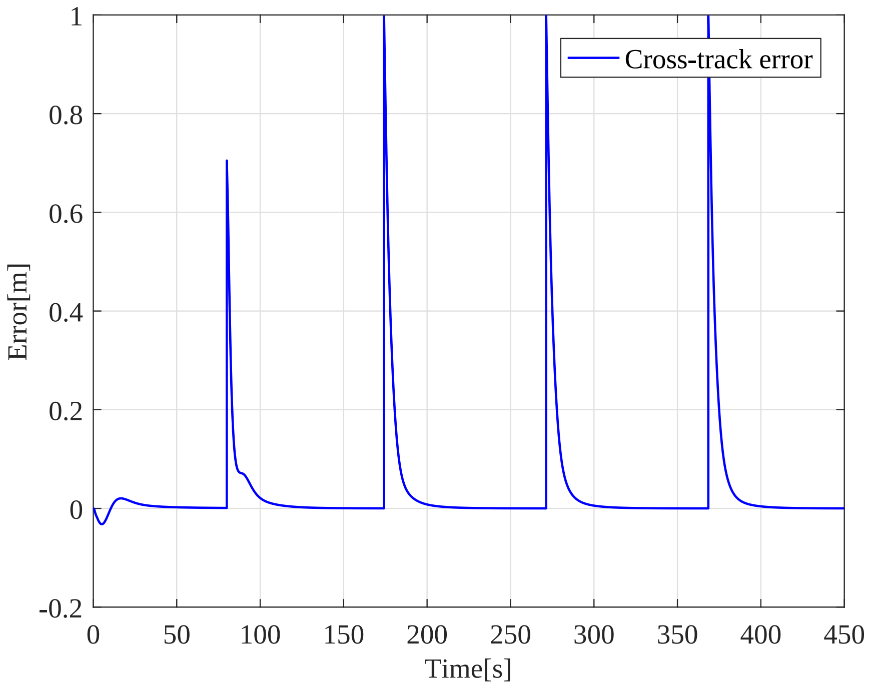

Figure 6.5: Cross-track error for straight-line path in between waypoints

For the circular paths the results were as promising as for the straight line paths. Both the path generated for clockwise- and counter-clockwise- motion were simulated and are shown in Figures 6.6 and 6.7.

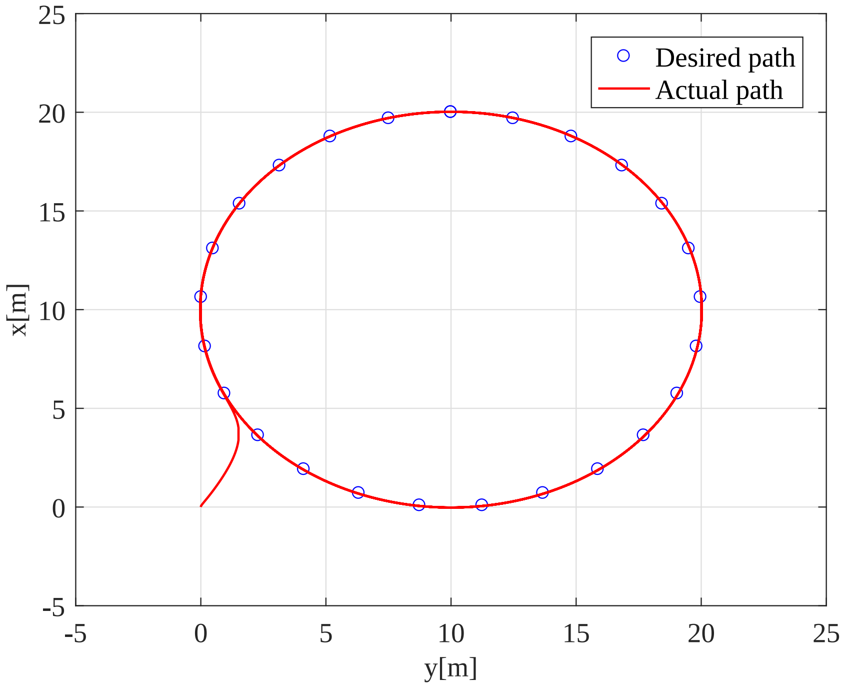

Figure 6.6: Circular path generated in clockwise direction

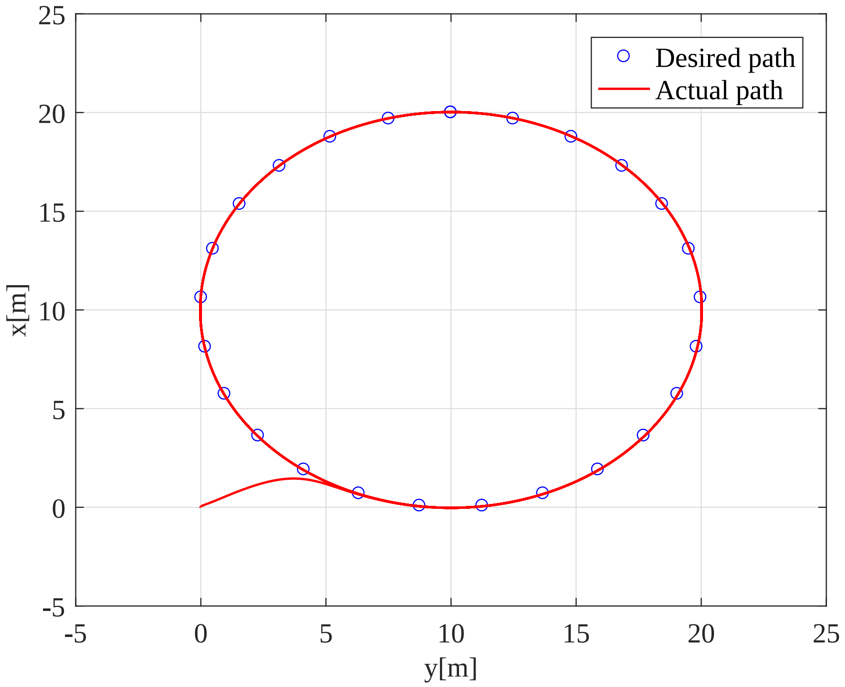

Figure 6.7: Circular path generated in counter-clockwise direction

The corresponding cross track errors are shown in Figures 6.6 and 6.7 respectively. In both of these plots it is obvious that the cross-track error converges rapidly to zero.

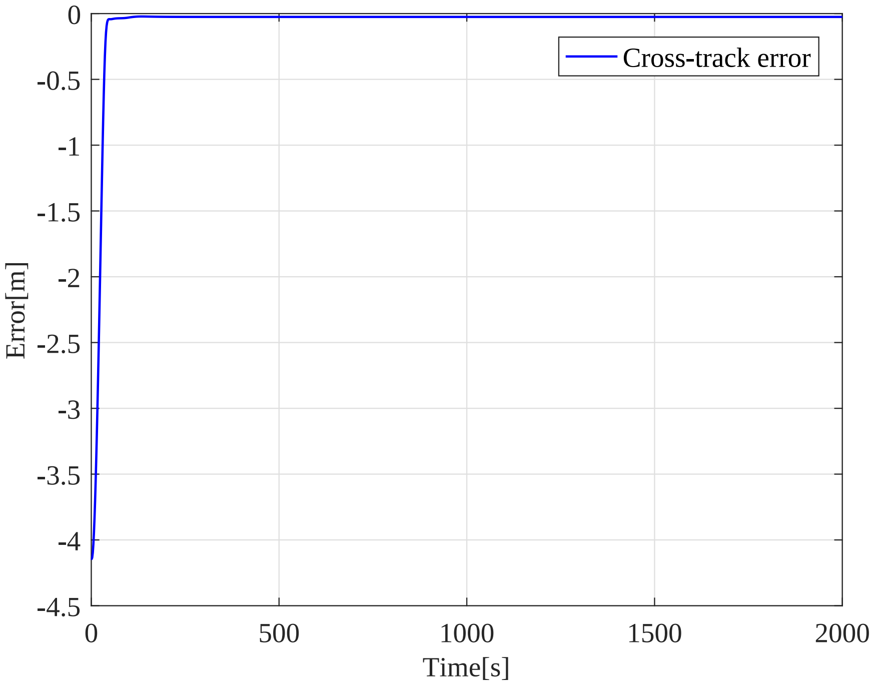

Figure 6.8: Cross-track error for circular path generated in clockwise direction

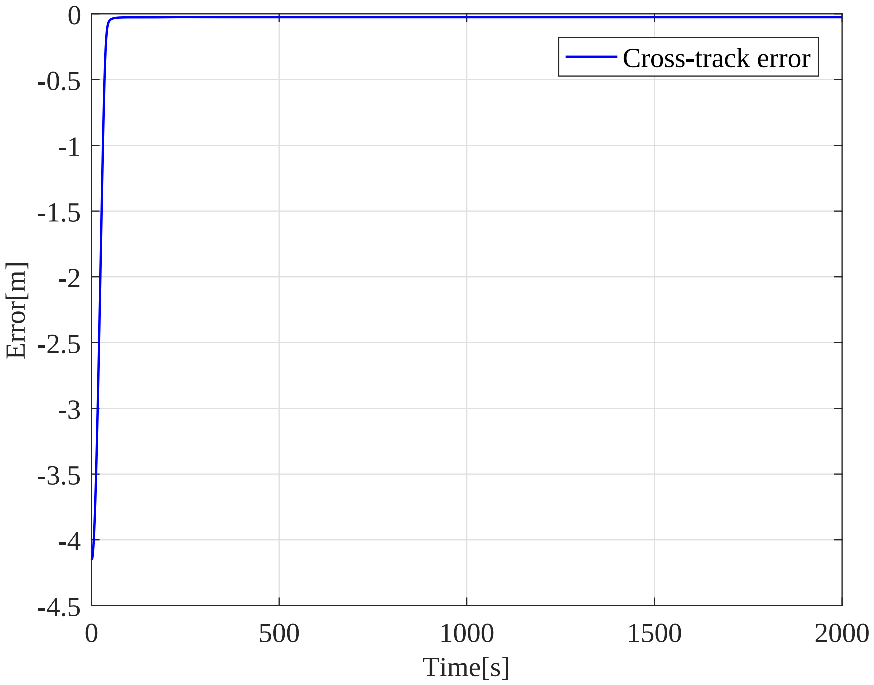

Figure 6.9: Cross-track error for circular path generated in counter-clockwise direction

Path-Tracking

In this section the paths will be generated with respect of a path-parameterized variable which makes the path develop as explained in Section 6.2. To begin with, a square path consisting of straight lines between waypoint will be generated and tracked by CSEI. This is shwn in Figure 6.10. The along-track- and cross-track- errors can be seen in Figure 6.11.

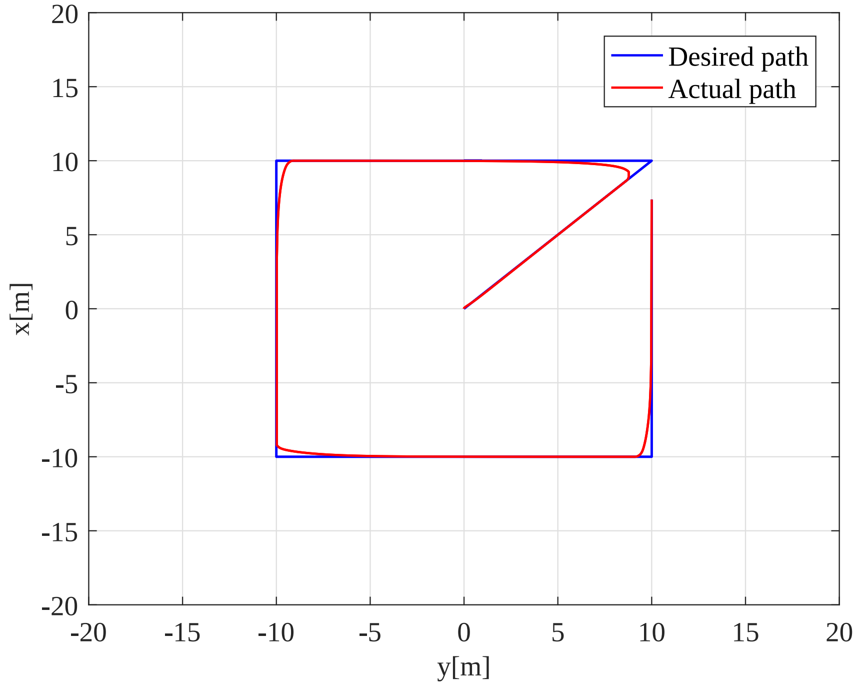

Figure 6.10: Parameterized straight-line paths

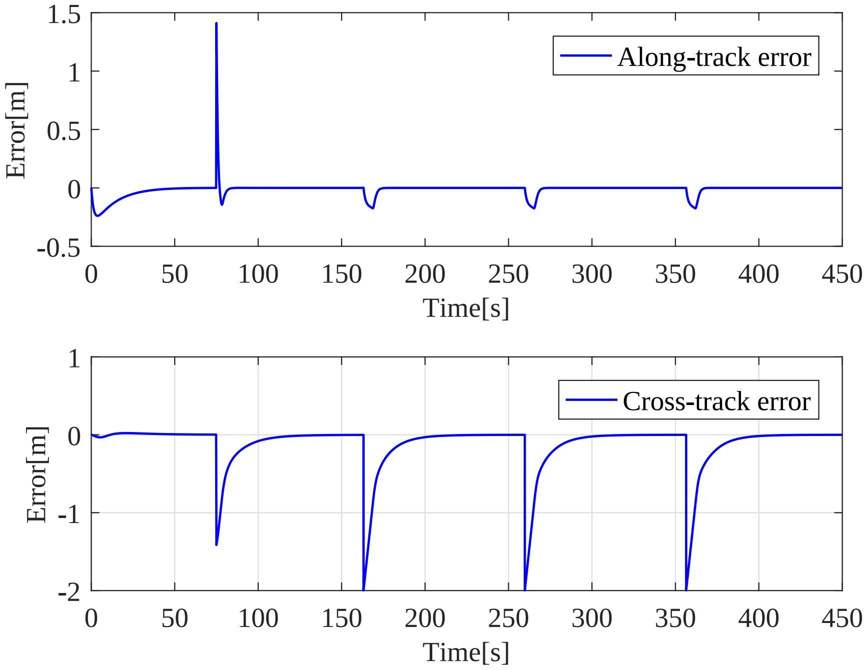

Figure 6.11: Epsilon for parameterized straight-line paths

From Figures 6.10 and 6.11 it can be seen that both errors converge towards zero. The jumps in the plots are made when the waypoints are within switching range and a new trajectory towards the next waypoint is generated. This can also be seen in the plot of the path variable in Figure 6.12, where s does not reach its final value of 1.

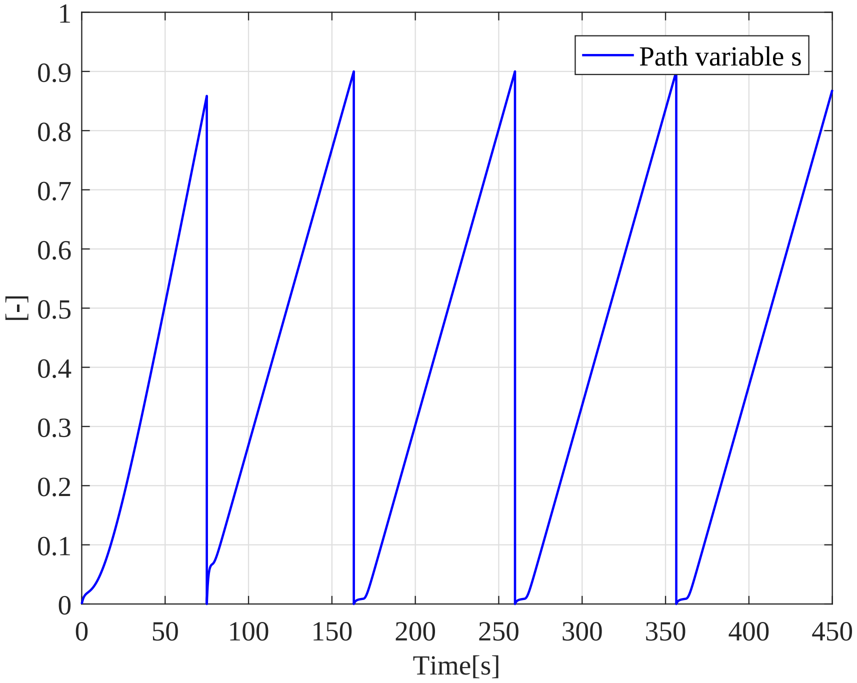

Figure 6.12: Parameterized path variable

The effect of the feedforward term of (6.30) makes the path regulate its evolving speed as shown in Figure 6.12. When the vessel is ahead of the path variable speeds up to catch the vessel, but is also able to wait when the vessel is far from the path as shown with the less steep part of the curves.

This can also be seen from generation and tracking of circular path. In Figure 6.13, the parameterized path starts at the top of the circle. The dots in the plot are plotted with a fixed rate and shows how the path waits for the vessel before speeding up to the desired velocity. The vessel starts at the origin and is set to move to a circular path with origin at $(x, y) = (10, 10)$ and a radius of 10 m. The path moves in clockwise direction for the entire simulation time.

Figure 6.14, show the corresponding along-track- and cross-track- error plots. These plot shows that both error terms seem to converge towards zero over time. This means that the vessel is able to track the desired path even when starting far from the circular path.

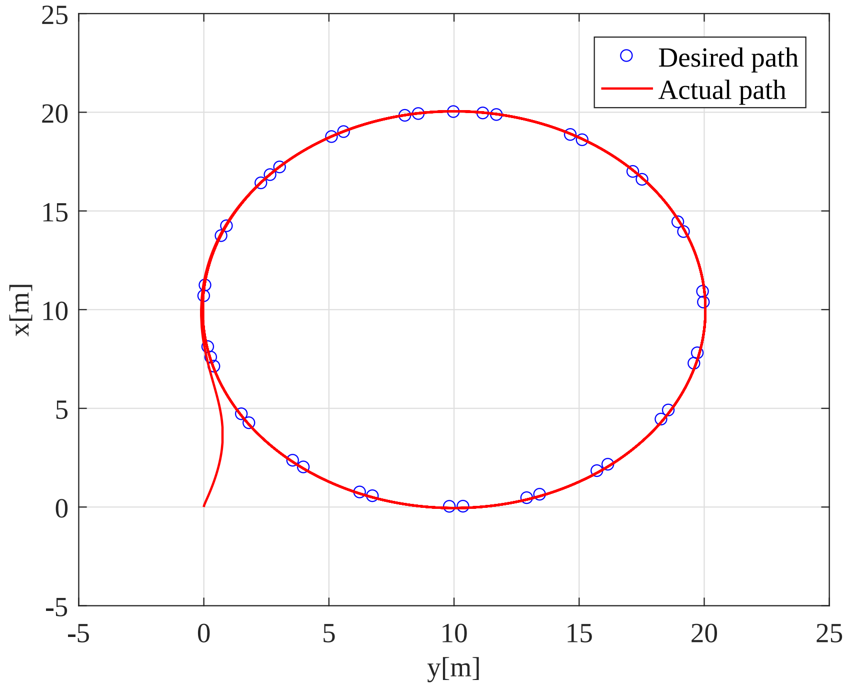

Figure 6.13: Parameterized circular path

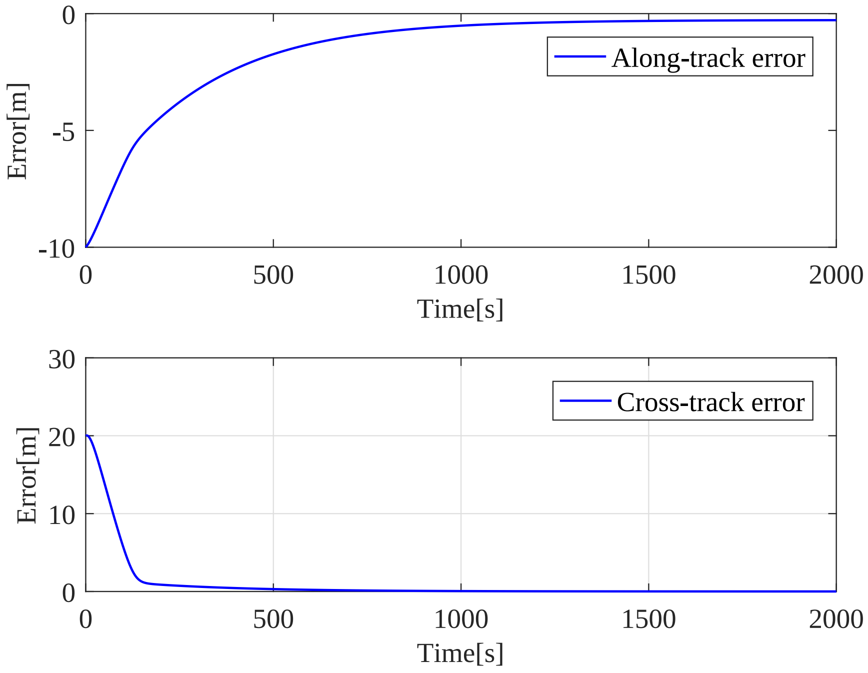

Figure 6.14: Epsilon for circular path

Current Compensation

Finally, current forces were added to the vessel model of CSEI. For these simulation a current velocity of 0.01 m/s was included in both surge and sway. Both parameterized paths were simulated with current and the results are shown in Figures 6.15, 6.16 6.17 and 6.18.

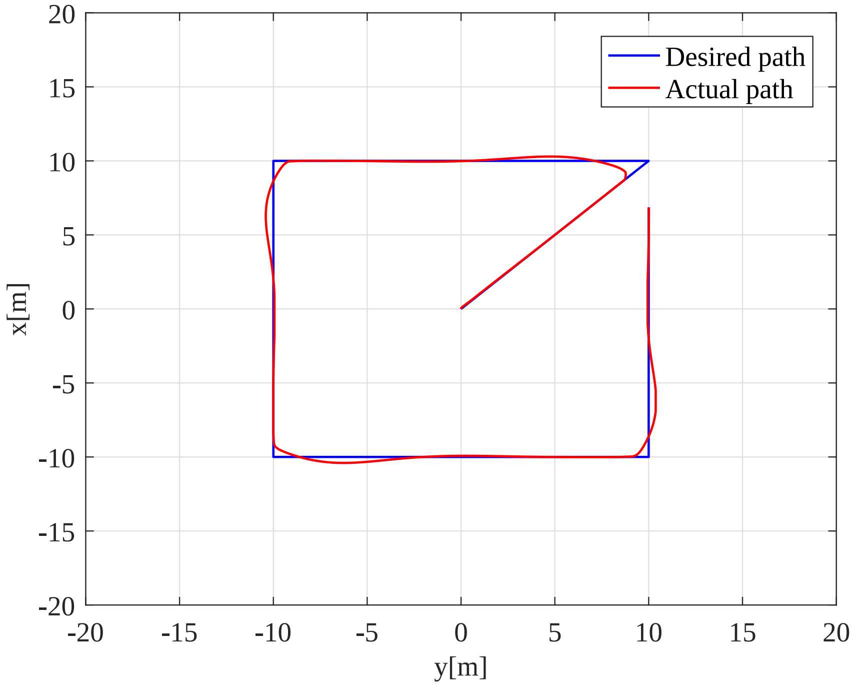

Figure 6.15: Straight-line path with current compensation

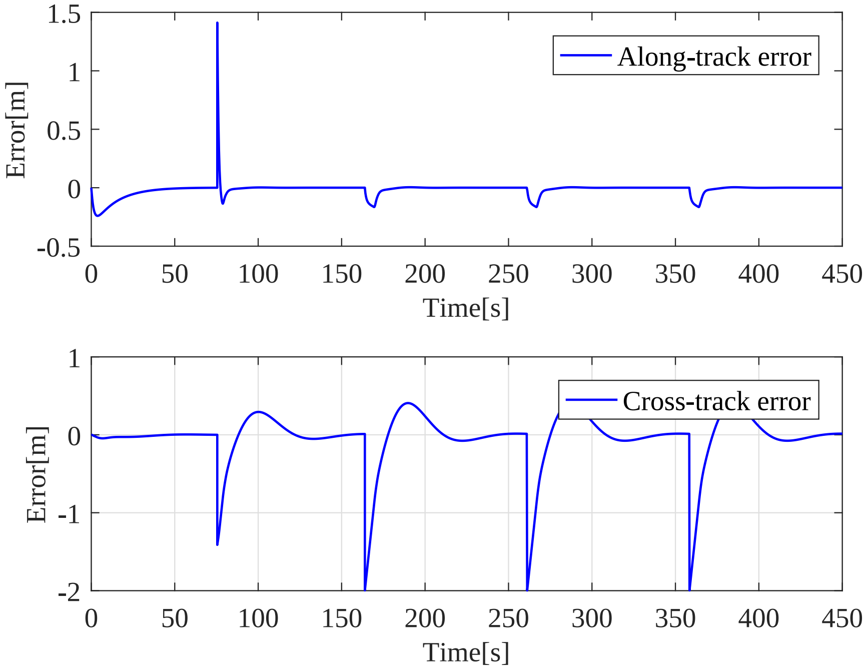

Figure 6.16: Epsilon for straight-line path with current compensation

These figures show that current will affect the behaviour of the vessel. Most noticeable are the plots of straight lines between waypoints in Figures 6.15, 6.16. Due to the sudden changes of

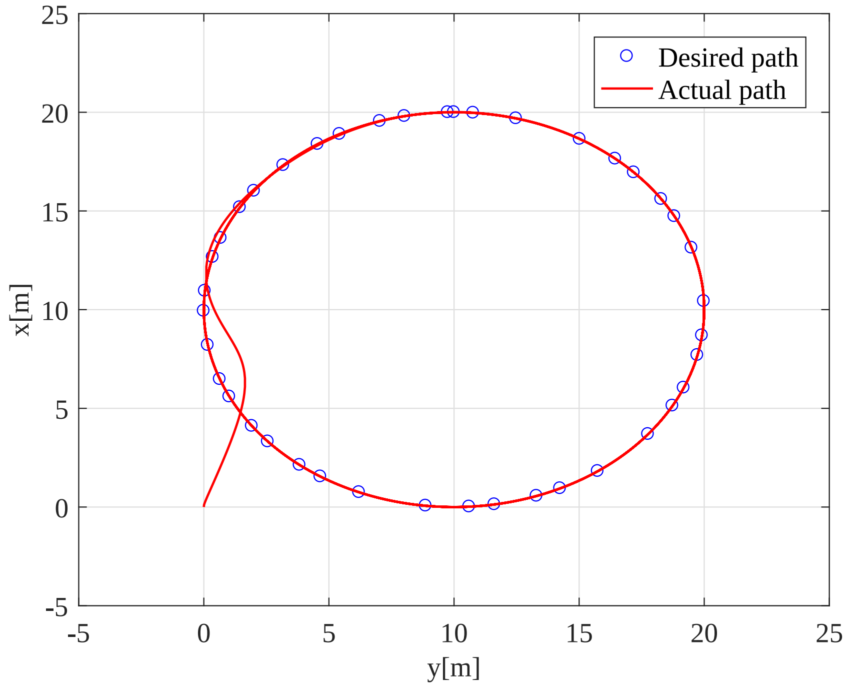

Figure 6.17: Circular path with current compensation

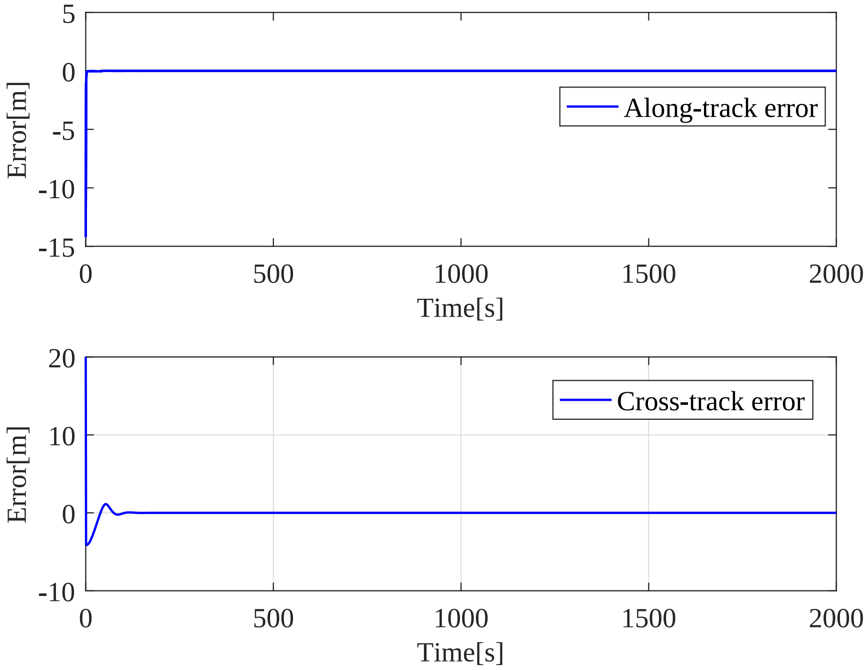

Figure 6.18: Cross-track error for circular path with current compensation

desired waypoints it sends the vessel on a slighly different path.

The circular path does not encounter such sudden changes, but the effect of the current can be seen in the slope towards the circular path. Since the vessel no is pushed with a higher velocity by the current the path does not wait as long for the vessel as without the current.

From the simulations with current it is clear that the ILOS compensation of current forces manages to steer the vessel to towards the desired paths. This applies for both straight lines and circles.

6.4.2 HIL Simulations for Guidance

The previous plots from HIL simulations in Section 5.4.3 are actually for a path-following maneuver shown in Figure 6.19. This plot shows how the vessel moves in between waypoints as simulated in Figure 6.4. This simulation is done without current. The vessel seems to move along the path without issues, turning slightly before it reaches each waypoint at the corner of the square. The cross-track error can be seen converge as the path becomes aligned with the grid in the plot after each turn. Again, this proves how similar the results from HIL and simulations in MATLAB/Simulink are and that the complete path-following autopilot is ready for physical testing in the MC Lab.

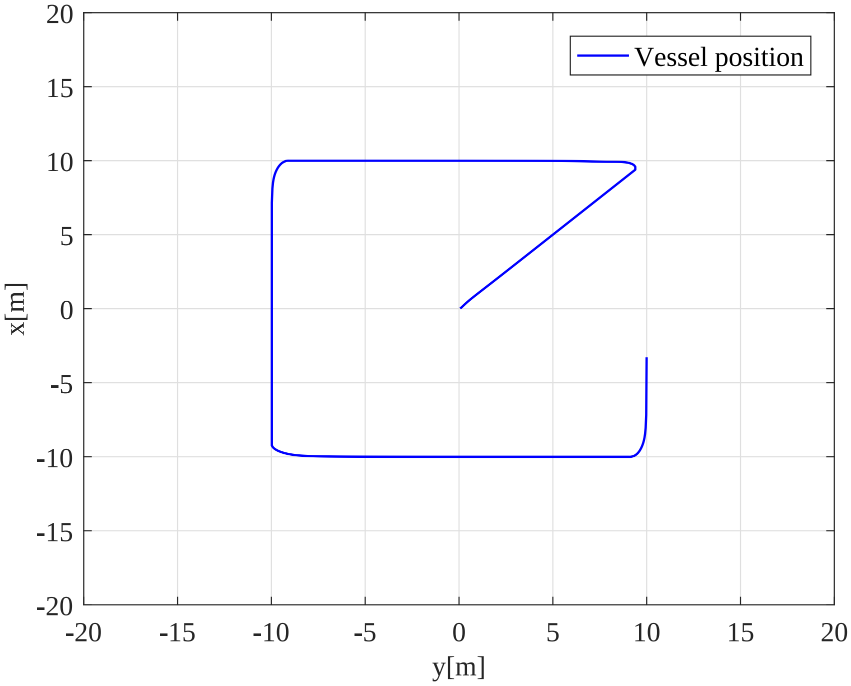

Figure 6.19: Square path consisting of straight lines from HIL

6.4.3 Simulations of Path-Following and Path-Tracking for R/V Gunnerus

This section will contain the same path-following procedures as in the previous section, but for the R/V Gunnerus vessel. As path-generation is not affected by how long the paths are, nor if the desired velocities are higher only some of the scenarios will be presented for the full scale vessel model.

The paths will begin at the origin and be scaled up to fit the full scale vessel of R/V Gunnerus. Therefore, the path will be very similar to the ones in the previous sections, only larger.

Path-Following

Figure 6.20 shows the desired path and how R/V Gunnerus converges to it.

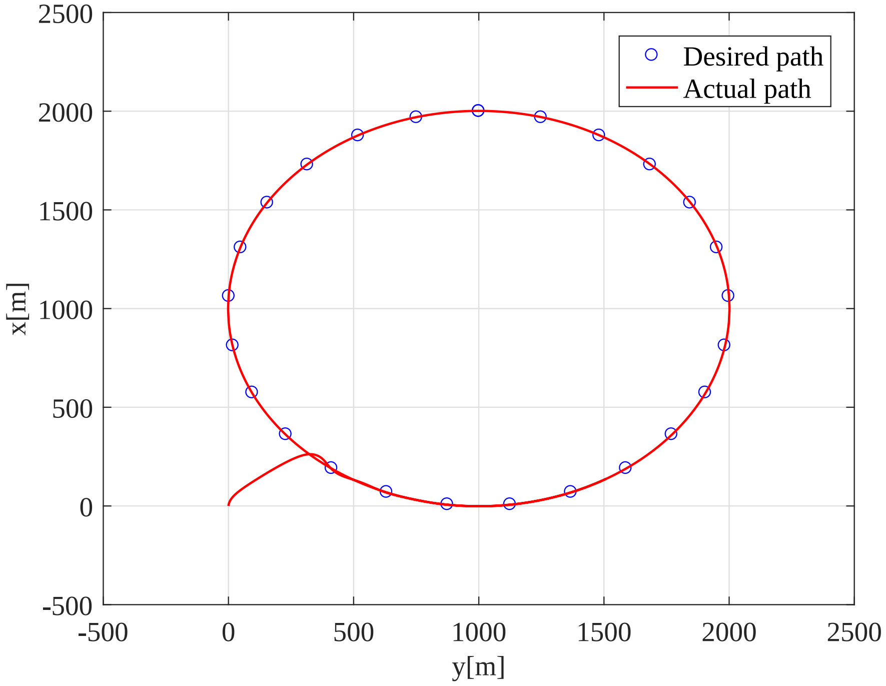

Figure 6.20: Circular path generated in counter-clockwise direction for R/V Gunnerus

Using the cross track error from Figure 6.21 it is possible to see how the corresponding cross-track error evolves throughout the simulation.

Figures 6.20 and 6.21, shows that the paths are successfully generated and that R/V Gunnerus has no problems following them for the entire simulation time.

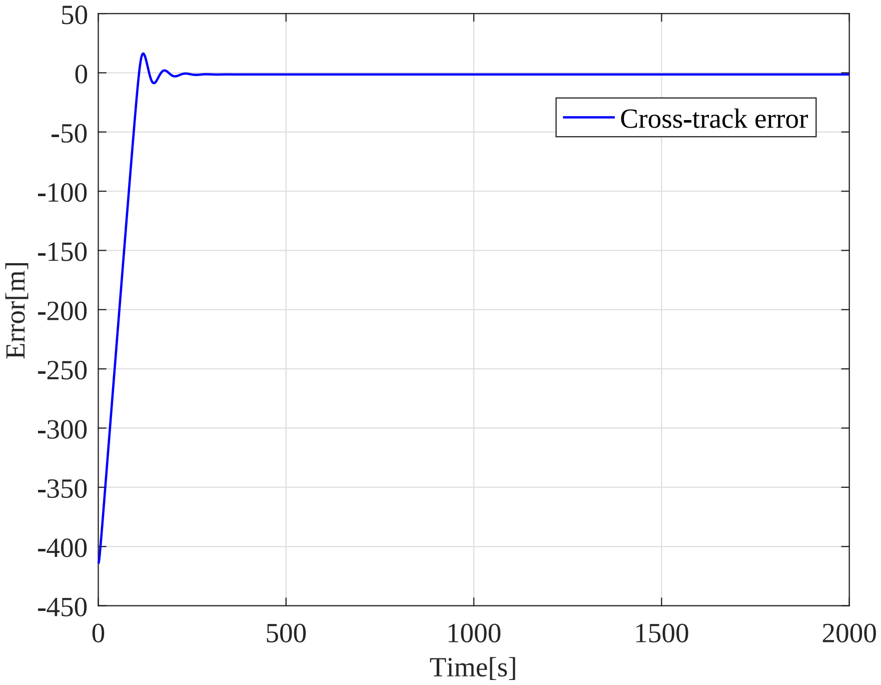

Figure 6.21: Cross-track error for circular path generated in counter-clockwise direction for R/V Gunnerus

Path-Tracking

The simulations of a larger circular parameterized paths for R/V Gunnerus is shown in Figure 6.22. The corresponding along-track and cross-track errors are shown in 6.23. From these two plots it can be seen that the parameterized path is generated successfully and that the vessel manages to track it with almost no errors.

Figure 6.22, also shows how the path slows down until the vessel is close with the dots closer to each other. The increasing space between them shows that the path speeds up to the desired vessel speed.

In Figure 6.24, the developement of how the path-variable for the circular path is shown. The negative values corresponds to that the vessel is behind the desired position, making the path to evolve slower. An increase in s of 1 corresponds to one round in a circular path, moving in clockwise direction.

Current Compensation

Finally, current forces are added to the R/V Gunnerus vessel model and a straight-line path is simulated as shown in Figure 6.25. It shows that the current forces initially push the vessel out of the desired path. This can be seen in the origin and at each corner. Then the current

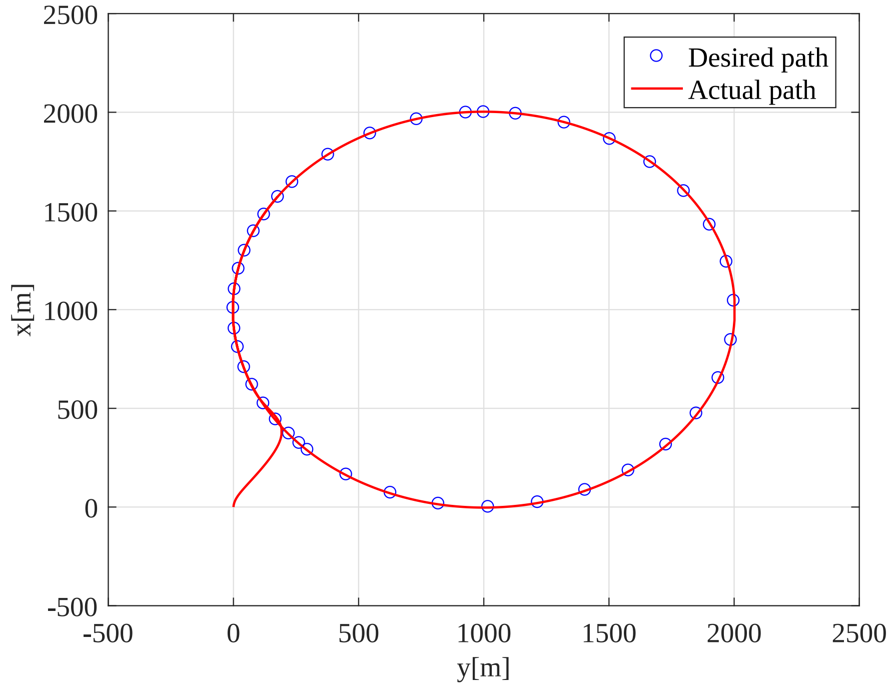

Figure 6.22: Parameterized circular path for R/V Gunnerus

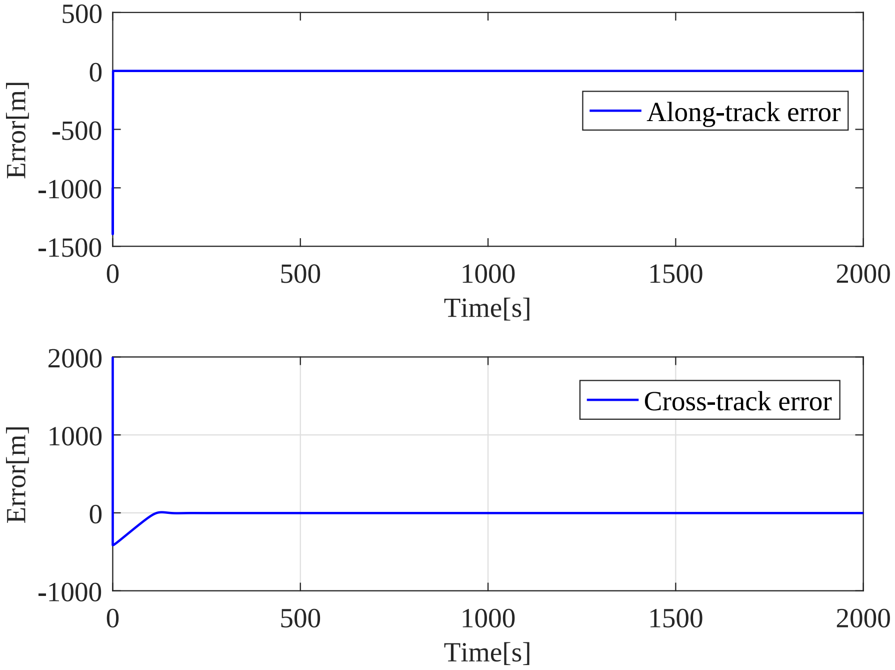

Figure 6.23: Epsilon for circular path for R/V Gunnerus

compensator term from the ILOS guidance law counteract the current and the vessel is able to track the path with small errors.

Figure 6.26 shows how the along-track- and cross-track- errors converge to zero after each

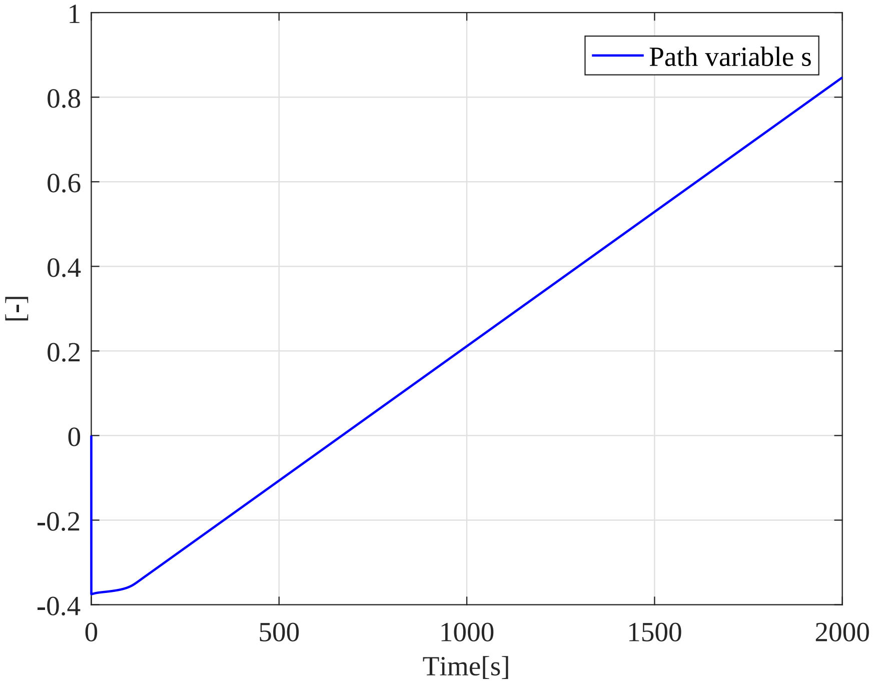

Figure 6.24: Path variable for circular path

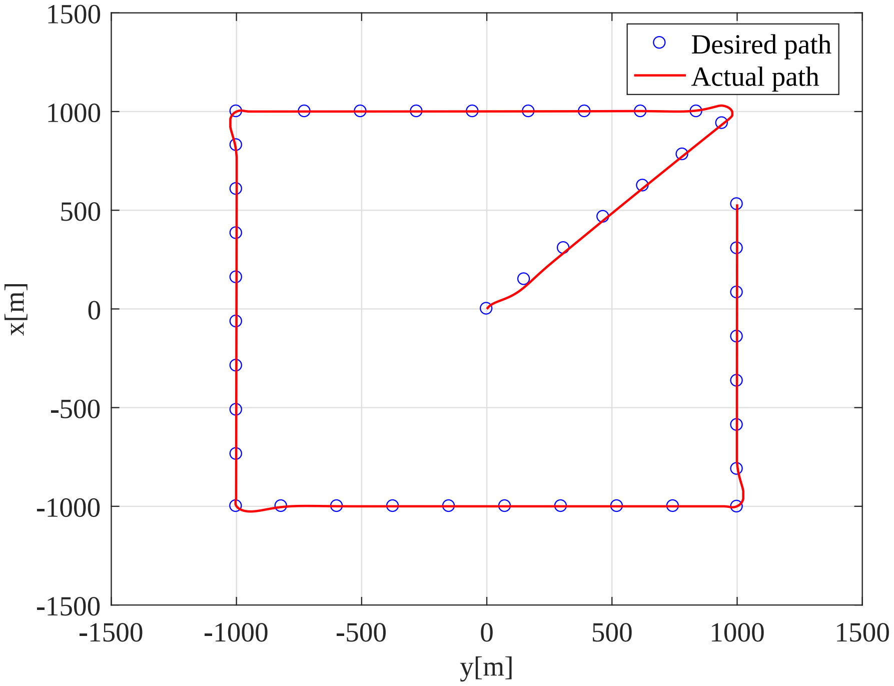

Figure 6.25: Straight-line path with current compensation

turn. Looking at both Figure 6.25 and Figure 6.25 it seems that the current is counteracted successfully and that the full-scale vessel model is able to navigate in current.

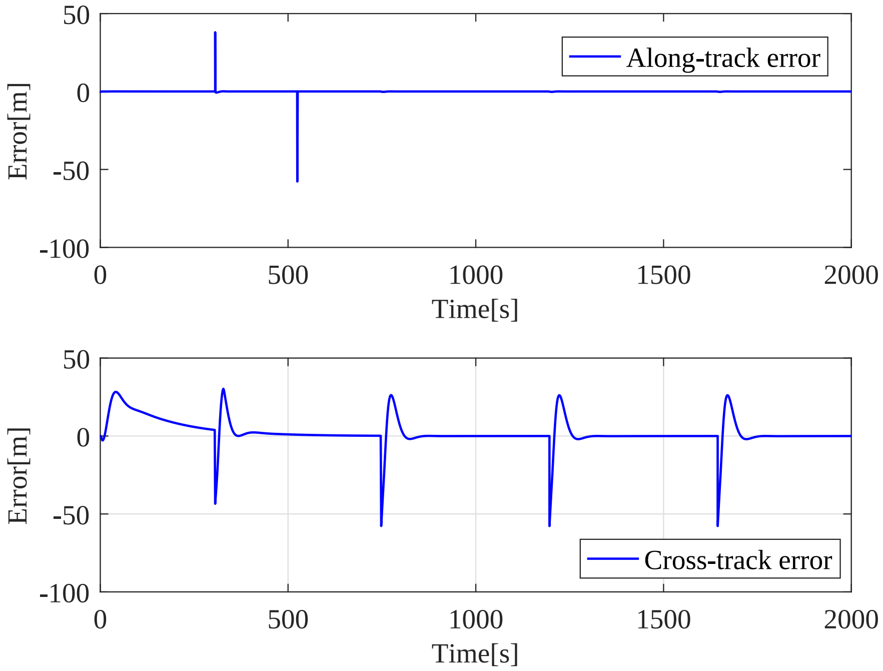

Figure 6.26: Epsilon for straight-line path with current compensation

6.5 Conclusions

From the results in Section 6.4, it is possible to see that the time-unconstrained path-following simulations worked as expected for both straight-line path between waypoints and for the circular path. The cross track error was forced towards zero every time the vessel reached the desired path or changed path towards the next waypoint.

For the parameterized paths, similar results were obtained. The cross-track error as well as the along-track error were both forced to zero, making the vessel follow the desired path with the desired velocity. Adding current forces caused drifting and were successfully treated by the compensator terms added to the guidance laws.

Simulations were done for both CSEI and R/V Gunnerus. The path generation, path-following and tracking were simulated successfully for both vessels. This was expected as path generation is a separate module of the control system and only depends on that the controller for CSEI and R/V Gunnerus are able to follow the desired heading and speed. In addition, the HIL simulations showed that the control system with path generation was successfully implemented resulting in exactly the same results making the control system ready to test on physical model vessels in the laboratory.

Chapter 7

Discussion

In the following chapter, an overall discussion will be done for the derivation, implementation and simulation results for the signal-based observer and the path-following adaptive autopilot design.

7.1 Discussing the Normalized Maneuvering Models

In Chapter 2 the mathematical modeling of the model vessel CSEI was presented. For this model, the maneuvering models, maneuvering characteristics and normalization procedures were derived. The complexity of the scaling procedure increased with the number of DOF. This makes the normalization of the 2DOF sway-yaw subsystem much more complex than the surge-speed and the Nomoto models. In addition, some modifications needed to be made because of a faulty vessel model which included a quadratic damping term to the surge speed equation and did not include coriolis forces. Due to lack of coupled damping terms (the coefficients are wrong in given the vessel model) the destabilizing Munk moment became dominant in the 2DOF sway-yaw subsystem. The linear damping terms were not large enough to cope with this, yielding inaccurate results. This made the choice of desired maneuvering models easier since the only models left were the normalized surge-speed model and the normalized 1st order Nomoto model. By application of these models for control design the most significant errors in the hydrodynamical coefficients are avoided. By applying these simplified models the control designs becomes less advanced. The model parameters will in further control design be treated as unknown and are going to be estimated. This makes the controller designs completely unaffected by the faulty parameter values in the given vessel model. Finally, by assessment of the directional stability it is shown that the CSEI model and R/V Gunnerus are both straight line stable. This vessels can then be said to have similar maneuvering characteristics using Norrbins or Bechs nonlinear Nomoto models.

7.2 Discussion Concerning the Signal-Based Observer

The signal-based observer discussed in Chapter 4 uses measurements from GNSS, compass and IMU to estimate the attitude, translation and velocities for the vessel. For the low-cost perspective it is preferable since it can be implemented in similar way for the CSEI model as for the full scale vessel. In addition, there is no need for model parameters and expensive sea trials. During tests in MATLAB and in HIL simulations, the observer managed to estimate all the states necessary with errors converging to zero. By adding noise on the specific force measurements, the filter effects were shown both for the attitude part and for the translational part of the observer. With noise, the estimates were worse, but nonetheless small with errors that converged to zero. The largest peaks of the noise were also filtered by the observer using integration.

7.3 Discussion of the Adaptive Controllers

Throughout Chapter 5, two types of direct MRAC algorithms were developed for heading control, while one indirect MRAC was implemented for surge-speed control. The results from simulations on CSEI shows that all controllers worked well even without robustification. However, by adding large disturbances (such as current) the parameter estimates drifted. By introduction of the dead-zone modification chattering of the signals were removed when the tracking errors were low. The projection operator, ensured that the parameter estimates where bounded in case of drifting. Scaling the controllers, proved easier than expected. Only a bit of tuning was necessary in order to obtain the desired response for the full scale model of R/V Gunnerus as for the CSEI making the normalized controllers successful in keeping the low-cost perspective for the control design. HIL simualtions proved that the controllers behaved just as for the simulations in MATLAB/Simulink.

7.4 Discussion Based on Guidance

As an extension to the autopilot design, path generation, path-following and path-tracking was implemented for straight lines and circles. Chapter 6, explained how these paths could be generated with and without the use of parameterization. The principle guidance law that were used for simulations was the lookahead-based LOS guidance.This because its simplicity and overall validity of the whole range of cross-track errors. Simulations where done for both circular and straight lines, with and without parameterization as well as for both with and without current forces. The controllers and observers derived in Chapters 4 and 5 were all used to perform these simulations. Looking at the results from the simulations and from HIL tests it is clear that the autopilot did manage to follow and track the paths properly, even with current forces acting on the vessel. This means that the compensation terms in the LOS algorithm worked as expected and is ready for practical tests on CSEI in the MC Lab.

Chapter 8

Conclusions and Further Work

8.1 Overall Conclusion

The goal of this was to design, implement and test a signal-based observer and a path-following normalized autopilot to fulfill the low-cost goals of commercial shipping. Simplified maneuvering models were derived in order to determine their applicability to scaling. In this way the basis for the normalized adaptive controllers were made. A kinematic observer design was made as a separate part of the control system. This uses measurements from GNSS, compass and IMU in order to estimate the vessels attitude, position and velocities. Therefore, model parameters are not needed for estimation and avoids the need for costly sea trials. The choice of controllers were based on the same principle of avoiding using model parameters. For this, the MRAC design was chosen. By using reference models and control designs based on the normalized maneuvering models, the required parameters were now treated as unknowns. The controllers used adaptation in order to estimate these unknown values while controlling the vessel. Robustification techniques were also applied to bound the estimates. Finally, a guidance loop was added to the control system making the vessel able to move along predetermined paths in both constrained-time and unconstrained-time path following applications.

Simulations are done throughout this thesis in order to choose the preferred models and determining the performance of each component in the control system. For the maneuvering models the 1st order Nomoto model was chosen as the preferred heading model. The surge-speed model was chosen for controlling the vessels speed. Using these normalized models, the control system was first implemented and tested using MATLAB and Simulink. Then, HIL simulations were done using the same software as in the MC Lab. Simulations proved that the control system worked as expected. The kinematic observer was able to filter noise while keeping the errors converging towards zero, the MRAC controllers were able to generate and track reference signals controlling the vessel to the correct heading and to the desired speed. Robustification helped for special cases where large disturbances were added to the vessel models in term of current forces. The scaling procedure resulted in controllers working on both CSEI and R/V Gunnerus. Only minor tuning was necessary to obtain satisfying performance for the scaled vessel, even thought the controllers were originally designed for CSEI. Finally, path-following was simulated proving that the overall control system managed to steer the vessel along predefined paths, with and without current forces acting on the vessel models.

In short, a control system that satisfy the low-cost perspective was derived, implemented and tested through simulations with satisfying results. This shows that control systems for full-scale vessels can be designed without lengthy and expensive sea trials. Instead, control systems can be developed on model vessels with similar shape in laboratories.

8.2 Further Work

Continuing this topic the study can be extended into full-scale testing on vessels. It is important to study the applicability of normalized controllers with respect to other hull shapes and different vessels. There is a need for more similar studies in order to have a database of tests for which conclusions can be made on whether this control design will be beneficial or not. Another possibility is to extend the work done in this thesis to underwater vehicles in 6 DOF. By using normalized and adaptive controllers that do not use model parameters, a universal control system that works for more than one vessel can be developed.

The control system can also be extended to include obstacle avoidance to increase the autonomy of the vessel. Studies of this based on for instance LOS guidance have been made proving that it is possible. In addition, one could connect several vessels with similar control systems in order to be able to perform coordinated operations. This could also be useful for ships doing seismic mapping.

Bibliography

Bech, M., 1969. The reversed spiral test as applied to large ships.

Børhaug, E. e. a., 2008. Integral los control for path following of underactuated marine surface vessels in the presence of constant ocean currents. Proc. of the 47th IEEE Conference on Decision and Control, 4984–4991.

Breivik, M., Fossen, T., December 2008. Guidance laws for planar motion control. IEEE, pp. 570–577.

Brodtkorb, A. H., Teel, A. R., Sørensen, A. J., 2016. Hybrid observer combining measurements of different fidelities. IFAC PapersOnLine 49 (23), 506–511.

Bryne, T. H., Fossen, T. I., Johansen, T. A., 2014. Nonlinear observer with time-varying gains for inertial navigation aided by satellite reference systems in dynamic positioning.

Bryne, T. H., Fossen, T. I., Johansen, T. A., 2015. A virtual vertical reference concept for gnss/ins applications at the sea surface. IFAC PapersOnLine 48 (16), 127–133.

Caharija, W., 2014. Integral line-of-sight guidance and control of underactuated marine vehicles.

Caharija, W., Pettersen, K. Y., Bibuli, M., Calado, P., Zereik, E., Braga, J., Gravdahl, J. T., Sorensen, A. J., Milovanovic, M., Bruzzone, G., September 2016. Integral line-of-sight guidance and control of underactuated marine vehicles: Theory, simulations, and experiments. Control Systems Technology, IEEE Transactions on 24 (5), 1623–1642.

Campbell, S. F., Kaneshige, J. T., Larchev, G. V., April 2010. Projection operator: A step towards certification of adaptive controllers. AIAA Infotech at Aerospace 2010.
URL `http://hdl.handle.net/2060/20100027545`

Chou, J. C. K., 1992. Quaternion kinematic and dynamic differential equations. Robotics and Automation, IEEE Transactions on 8 (1), 53–64.

Clarke, D., Horn, J. R., 1997. Estimation of hydrodynamic derivatives. Proceedings of the 1997 11th Ship Control Systems Symposium. Part 2 (of 2) 2, 275–289.
URL `https://www.scopus.com/inward/record.uri?eid=2-s2.0-0030675878&partnerID=40&md5=6af0772f65076b2a68167ec74bfaa4ff`

Dubins, L. E., July 1957. On curves of minimal length with a constraint on average curvature, and with prescribed initial and terminal positions and tangents. American Journal of Mathematics 79 (3), 497–516.

Faltinsen, O. M., Sortland, B., 1987. Slow drift eddy making damping of a ship. Applied Ocean Research 9 (1), 37–46.

Fossen, T. I., 1991. Nonlinear modelling and control of underwater vehicles.

Fossen, T. I., 1994. Guidance and control of ocean vehicles. Wiley, Chichester.

Fossen, T. I., 2011. Handbook of Marine Craft Hydrodynamics and Motion Control. Chichester, UK: John Wiley & Sons, Ltd, Chichester, UK.

Fossen, T. I., Fjellstad, O., 1995. Nonlinear modelling of marine vehicles in 6 degrees of freedom.

Fossen, T. I., Perez, T., 2008. Mss hydro/gnc toolbox, part of marine systems simulator (mss). Available at: http://www.marinecontrol.org. Last used: 28.06.2017.

Grip, H. F., Fossen, T. I., Johansen, T. A., Saberi, A., 2012. Attitude estimation using biased gyro and vector measurements with time-varying reference vectors. Automatic Control, IEEE Transactions on 57 (5), 1332–1338.
URL `http://ieeexplore.ieee.org/ielx5/9/6187742/06060863.pdf?tp=&arnumber=6060863&isnumber=6187742`

Grip, H. F., Fossen, T. I., Johansen, T. A., Saberi, A., 2013. Nonlinear observer for gnss-aided inertial navigation with quaternion-based attitude estimation, 272–279.

Ioannou, P. A., Sun, J., 2012. Robust adaptive control. Dover Publications, Mineola, N.Y.

Kalman, R. E., 1960. A new approach to linear filtering and prediction problems. Journal of Basic Engineering 82 (1), 35.
URL `http://fluidsengineering.asmedigitalcollection.asme.org/data/Journals/JFEGA4/27220/35_1.pdf`

Kalman, R. E., Bucy, R. S., 1961. New result in linear filtering and production theory. Journal of Basic Engineering 83.

Khalil, H. K., 2015. Nonlinear Control: Global Edition, 1st Edition. Pearson Education Limited, Essex, England.

Krstiĉ, M., 1995. Nonlinear and adaptive control design. Adaptive and learning systems for signal processing, communications, and control. Wiley, New York.

Lavretsky, E., Wise, K. A., 2012. Robust and Adaptive Control : with Aerospace Applications. Robust and Adaptive Control. Springer, Dordrecht.

Lekkas, A. M., 2014. Guidance and path-planning systems for autonomous vehicles. Vol. 2014:126 of Doktoravhandlinger ved NTNU (trykt utg.). Norwegian University of Science and Technology, Faculty of Information Technology, Mathematics and Electrical Engineering, Department of Engineering Cybernetics, Trondheim.

Mahony, R., Hamel, T., Pflimlin, J.-M., June 2008. Nonlinear complementary filters on the special orthogonal group. Automatic Control, IEEE Transactions on 53 (5), 1203–1218.

Nomoto, K., February 1972. Problems and requirements of directional stability and control of surface ships. ARCHIVE: Journal of Mechanical Engineering Science 1959-1982 (vols 1-23) 14 (7), 1–5.

Nomoto K., T. Taguchi, K. H., Hirano, S., 1957. On the steering qualities of ships. technical report. International Shipbuilding Progress, Vol. 4.

Norrbin, N. H., 1963. On the Design Analyses of Zig-Zag Test on Base of Quasi Linear Frequency Response. Technical Report 12. Meddelanden (Statens skeppsprovningsanstalt). Göteborg.

Norrbin, N. H., 1971. Theory and observations on the use of a mathematical model for ship manoeuvring in deep and confined waters. Vol. 68 of Meddelanden (Statens skeppsprovningsanstalt). Göteborg.

NTNU, 2016. Handbook of Marine HIL simulation and Marine cybernetics laboratories. Retrieved February 15th, 2017, from `https://github.com/NTNU-MCS/MC_Lab_Handbook`.

Perez, T., Fossen, T. I., 2004. Marine systems simulator (mss). Available at: http://www.marinecontrol.org. Last used: 28.06.2017.

Saout, O., Ananthakrishnan, P., 2011. Hydrodynamic and dynamic analysis to determine the directional stability of an underwater vehicle near a free surface. Applied Ocean Research 33 (2), 158–167.

Schmidt, S. F., McGee, L. A., 1985. Discovery of the kalman filter as a practical tool for aerospace and industry - nasa-tm-86847.

Skjetne, R., 2005. The maneuvering problem. Vol. 2005:1 of Doktoravhandlinger ved NTNU (trykt utg.). Norwegian University of Science and Technology, Faculty of Information Technology, Mathematics, and Electrical Engineering, Department of Engineering Cybernetics, Trondheim.

Skjetne, R., 2014. Report: Maneuvering los control design: The fully actuated case.

Skjetne, R., 2016. Adaptive Autopilot: MRAC Case Study- Revision Draft for Studying.

Skjetne, R., Jørgensen, U., Teel, A. R., 2011. Line-of-sight path-following along regularly parametrized curves solved as a generic maneuvering problem. pp. 2467–2474.

SNAME, 1950. Nomenclature for treating the motion of a submerged body through a fluid : report of the American Towing Tank Conference. Vol. 1-5 of Technical and research bulletin (Society of Naval Architects and Marine Engineers. Technical and Research Committee). SNAME, New York, N.Y.

Sørensen, A. J., 2013. Marine Control Systems: Propulsion and Motion Control of Ships and ocean Structures-Lecture Notes.

Sørensen, M. E. N., 2015. Topics in system and control theory.

Vik, B., 2014. Integrated Satellite and Inertial Navigation Systems. Department of Engineering Cybernetics, NTNU, Trondheim.

World Geodetic System, 1984. Its definition and relationships with local geodetic systems. in:defense mapping agency.